MAGNETIC EXCITATIONS IN SOLIDS

Carl E. PATTON

Department of Physics, Colorado State University, Fort Collins, Colorado 80523, U.S.A.

NORTH-HOLLAND PHYSICS PUBLISHING – AMSTERDAM

PHYSICS REPORTS (Review Section of Physics Letters) 103, No. 5 (1984) 251–315. North-Holland, Amsterdam

MAGNETIC EXCITATIONS IN SOLIDS

Carl E. PATTON

Department of Physics, Colorado State University, Fort Collins, Colorado 80523, U.S.A.

Received September 1983

Contents:

1. Introduction	253	3.2. Dispersion modifications	286
2. Magnetic excitations	254	3.3. Nonlinear excitations	294
2.1. Spin-wave modes – Infinite isotropic medium	254	3.4. Relaxation	300
2.2. Magnetostatic modes – Isotropic thick slab	258	4. Magnon light scattering techniques	304
2.3. Dipole-exchange modes – Isotropic thin slab	265	4.1. Fabry–Perot interferometry	305
2.4. Dipole-exchange modes – Isotropic thick slab	272	4.2. Multipass and stabilization techniques	307
3. Anisotropy, parametric excitations, and relaxation	280	4.3. Mechanically scanned tandem operation	309
3.1. Surface anisotropy and pinning	280	References	312

Abstract:

This article presents a review of low to moderate frequency magnetic excitations, termed magnons or spin waves, in magnetically ordered materials. The emphasis is on intuitive behavior rather than analytical theory. Topics include spin waves, magnetostatic modes, dipole-exchange modes, surface anisotropy, dispersion properties, nonlinear effects, and relaxation. These phenomena are illustrated with experimental examples based on magnon light scattering results as well as conventional microwave techniques.

Single orders for this issue

PHYSICS REPORTS (Review Section of Physics Letters) 103, No. 5 (1984) 251–315.

Copies of this issue may be obtained at the price given below. All orders should be sent directly to the Publisher. Orders must be accompanied by check.

Single issue price Dfl. 37.00, postage included.

0 370-1573/84/$19.50 © Elsevier Science Publishers B.V. (North-Holland Physics Publishing Division)

1. Introduction

This article will review the properties of zero to moderate ($\sim 10^6\,\mathrm{cm}^{-1}$) wave number high frequency (GHz) magnetic excitations in ferro- and ferrimagnetic materials and in selected weak ferromagnets. The study of such excitations in magnetic systems has attracted considerable attention since the prediction of spin-wave resonance by Kittel [1] and the observation of such resonances by Seavey and Tannenwald [2]. In the years which have followed, the increasing availability of the high quality narrow linewidth films, first of permalloy and later of yttrium iron garnet (YIG), has led to a detailed ferromagnetic resonance (FMR) characterization of these effects. The complex FMR spectra demanded complex models. Theoretical work on volume inhomogeneities, pinning, and surface anisotropy have all made important contributions to the understanding of the data. Reviews by Puszkarski [3] and Wigen et al. [4] present representative citations to the literature.

In the last decade, however, theoretical advances have largely outstripped the resolving power of FMR as an experimental tool to study these high frequency magnetic excitations. The theoretical results, by Wolfram and DeWames [5] for example, indicate important new features for magnon dispersion in both thin films and bulk materials. FMR methods have uncovered only a few gross features expected from the theory, as shown by Tittmann and DeWames [6] and Henry et al. [7], for example.

A rather new technique, at least for magnetics work, appears to be capable of picking up where FMR leaves off. This technique is Brillouin light scattering. The advantages are numerous, as summarized by Camley and Mills [8] and Grimsditch et al. [9]. In FMR, one is generally limited to a single frequency or a limited range of frequencies. Detectable excitations are limited to those modes which can couple to an applied microwave field. The one exception is in the use of high power parametric pumping to excite propagating spin waves. Even here, however, other constraints limit the range of observable excitations and, once observed, their interpretation.

In Brillouin scattering, one observes scattered light which results from the interaction of the incident laser beam with all magnetic excitations in the material, at least in the region penetrated by the light. The scattering geometry will determine the wavevector $\boldsymbol{k}$ of the magnons to be observed, and the detection of all such magnons is possible in concept. One has, in effect, an extremely broadband (up to several thousand GHz with recent innovations) wavevector-selective spectrometer. Brillouin scattering has a further advantage in that the probe wavelength (the light) is generally much smaller than the sample, in contrast with FMR where the opposite is usually true. It is therefore possible to probe local regions and surfaces. In cases where the light penetration depth is small (as for metals), the surface region can be selectively examined.

Light scattering on magnetic excitations is weak, and it is only due to recent developments in Fabry–Perot interferrometry that the above potential can be (and has been) realizable. Notable in this regard are multipass techniques, rapid scanning systems with feedback stabilization, and most recently, the single PZT scanning of tandem systems (Sandercock [10, 11, 12, 13, 14]).

With the above advances, a number of magnetic studies have been carried out. These include measurements of anisotropy in $CrBr_3$ (Sandercock [15]), exchange in yttrium iron garnet (Sandercock and Wettling [16, 17]; Wettling et al. [18]), anisotropy and magnetostatic mode dispersion in EuO (Grünberg and Metawe [19]) and magnetostatic mode dispersion in iron and nickel (Sandercock and Wettling [20, 21]; Metawe and Grünberg [22]). With a few exceptions, most of the above work serves mainly to illustrate the applicability of Brillouin scattering to magnetic studies. The data generally confirm known properties or known phenomena.

There have been several applications to new materials and to the elucidation of unknown phenomena. Work in the first category includes the light scattering characterization of amorphous metals by Chang et al. [23], Malozemoff et al. [24, 25], and Grimsditch et al. [9]. Work in the second category includes the detailed study of magnon dispersion in the weak ferromagnet $FeBO_3$ by Jantz et al. [26] and Jantz and Wettling [27, 28]. Extensive work on $CoCO_3$ has been done by Borovik-Romanov and co-workers [29, 30]. The applicability of Brillouin scattering to investigations of ferro- and antiferromagnetic resonance has also been demonstrated by Borovik-Romanov et al. [31] for $CoCO_3$ and by Wettling et al. [32] for $FeBO_3$. The applicability of Brillouin scattering to nonlinear phenomena (parametric excitation of magnons) has been shown by Zhotikov and Kreines [33, cited as Khotikov; 34] for $CoCO_3$ and by Wettling et al. [35] and Wettling and Jantz [36] for $FeBO_3$. Grünberg et al. [37] have recently demonstrated repulsion between the bulk and surface spin-wave dispersion branches in thin iron films. Wilber et al. [38] has reported the observation of spin waves in polycrystalline ferrite by light scattering.

The objective of the present work is to provide a review of the physics of low to moderate wave number (0–$10^6\,cm^{-1}$) magnetic excitations (<1000 GHz) in representative ordered magnetic systems. The theoretical emphasis is on intuitive understanding rather than mathematical rigor. The theory will be augmented by recent experimental results obtained primarily by light scattering methods. The material is divided into two sections: (1) Spin-wave excitations; (2) Anisotropy, parametric excitations, and relaxation. Brillouin light scattering techniques are discussed in the last section. This article is intended to complement the recent review by Borovik-Romanov and Kreines [39, 40, 41], which has emphasis on the weak ferromagnets, and the reviews of Brillouin scattering in condensed matter by Dil [42] and Sandercock [14].

2. Magnetic excitations

This section reviews magnetic excitations. Detailed theory is avoided. The basic ideas are presented on an intuitive level. The discussion is limited to the relatively low wavenumber, low frequency excitations, accessible with Brillouin scattering techniques. Isotropic media only are considered. The four sections deal with excitations in an infinite isotropic medium, magnetostatic modes for an isotropic thick slab, dipole-exchange modes for an isotropic thin slab, and finally, dipole-exchange modes in an isotropic thick slab.

2.1. Spin-wave modes – Infinite isotropic medium

It is straightforward to show (see Sparks [43]) that the exchange energy of a spin wave with wavenumber k varies as Dk^2, where D is an exchange parameter. When Zeeman and volume dipolar energies are included, one obtains the well known Holstein–Primakoff [44] spin-wave dispersion relation

$$\omega_k/\gamma = [(H + Dk^2)(H + Dk^2 + 4\pi M_0 \sin^2 \theta_k)]^{1/2} . \tag{2.1}$$

In the above, ω_k is the spin-wave frequency, γ is the gyromagnetic ratio of the electron ($\gamma \simeq 1.76 \times 10^7\,Oe^{-1}\,sec^{-1}$ for $g = 2$, and is taken as positive), H is the static internal field, and θ_k is the polar angle between $\boldsymbol{H}$ and $\boldsymbol{k}$. For purposes of this report, the coordinate system of fig. 2.1 will be used, with H and the magnetic induction $4M_0$ in the z-direction.

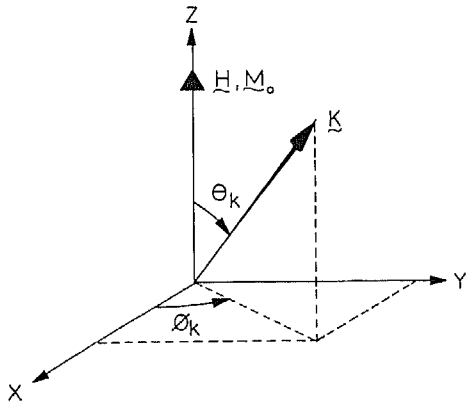

Fig. 2.1. Coordinate system for spin waves in saturated magnetic medium.

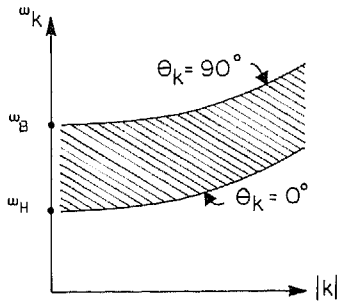

Fig. 2.2. Spin-wave manifold.

The spin-wave dispersion defined by eq. (2.1) is graphically displayed in fig. 2.2. Both positive and negative k are allowed. The lower branch, labeled $\theta_k = 0$, is for spin-wave propagation parallel to $\boldsymbol{H}$. This branch extrapolates to the Zeeman frequency $\omega_H = \gamma H$ in the $k = 0$ limit and is described by the equation

$$\omega_k(\theta_k = 0) = \omega_H + \gamma D k^2 . \tag{2.2}$$

The gyroscopic precession cone (classically speaking) for this branch is circular, and a representative spin wave is sketched in fig. 2.3a. Note that for this configuration, $\nabla \cdot \boldsymbol{M}$ is zero. The absence of dipolar contributions to the spin-wave energy leads to the circular precession and the absence of a square root in eq. (2.2). (Alternatively, one could say that the restoring torques for small deviations of $\boldsymbol{M}$ in the x- and y-directions are equivalent.)

Turn now to the upper branch, for spin waves propagating perpendicular to $\boldsymbol{H}$ ($\theta_k = 90°$). The

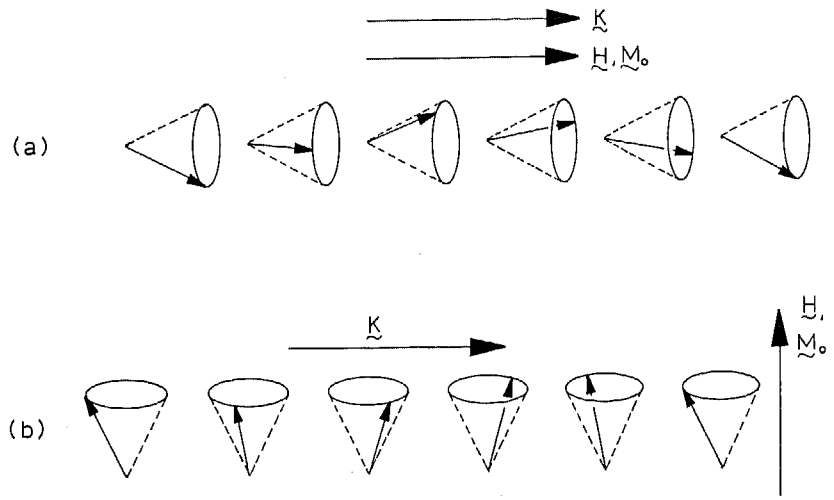

Fig. 2.3. Schematic spin waves. (a) Schematic spin wave for $\theta_k = 0$. (b) Schematic spin wave for $\theta_k = 90°$.

upward shift in ω_k is due to the nonzero volume dipolar contribution to the spin-wave energy for $\theta_k \neq 0$. From the schematic spin-wave mode in fig. 2.3b for $\theta_k = 90°$, it is observed that $\nabla \cdot \boldsymbol{M}$, and hence the dipolar energy, is nonzero. These interactions shift ω_k upward.

This dipolar interaction has two related effects, the increase in ω_k and a modification of the precession cone from circular to elliptical. The degree of the induced ellipticity, in turn, influences the magnitude of the ω_k shift. It is relatively easy to see from demagnetizing field arguments that the shift in ω_k/γ would be simply $2\pi M_0$ *if* no ellipticity were induced and the precession remained circular. This would lead to a $k = 0$ extrapolation for the upper branch of

$$\omega_k(k = 0, \theta_k = 90°) = \gamma(H_0 + 2\pi M_0)\,. \tag{2.3}$$

The induced ellipticity (the precession cone is essentially squashed with the major axis perpendicular to $\boldsymbol{k}$) leads to a reduction in the shift from $2\pi M_0$. The dispersion for the upper branch is given by

$$\omega_k/\gamma = [(H + Dk^2)(H + Dk^2 + 4\pi M_0)]^{1/2} \tag{2.4a}$$

with a $k = 0$ extrapolation of

$$\omega_k(k = 0, \theta_k = 0) = \gamma[H(H + 4\pi M_0)]^{1/2}\,. \tag{2.4b}$$

The square root in eq. (2.4a) is one reflection of the ellipticity of the corresponding precession. In the limit of a large $(H + Dk^2)$ term or a small $4\pi M_0$, the precession will be nearly circular and eq. (2.4b) will approach the expression in eq. (2.3). These considerations will be especially relevant for surface magnons in the next section.

The cross-hatched region in fig. 2.2, often called the spin-wave manifold, is not extended to $k = 0$. When k is on the order of an inverse sample dimension or smaller ($k < 10^2$–$10^5\,\mathrm{cm}^{-1}$, depending on sample size) surface dipolar interactions become important. These effects are considered in succeeding subsections. The upper limit on k for the spin-wave approximation to be valid is generally specified as $k \ll \pi/a$, where a is a lattice constant, so that k is small in comparison to the Brillouin zone edge. Typical values of the exchange parameter D for ferromagnetic materials are in the $(1\text{–}5) \times 10^{-9}$ Oe-cm^2 range. This means that exchange field shifts can range from negligible at low k to moderate (kOe) for values of k in the $10^6\,\mathrm{cm}^{-1}$ range.

Brillouin scattering was first applied to the study of spin waves in bulk YIG spherical samples (Sandercock and Wettling [16, 17]), in EuO (Grünberg and Metawe [10]), and in $CrBr_3$ (Sandercock [15]). For the latter two materials, the exchange parameter D was too small to give any appreciable exchange contribution to ω_k. For YIG, however, a backscattering configuration was used to observe $\theta_k = \pi/2$ spin waves for $k = (1.9\text{–}2.6) \times 10^5\,\mathrm{cm}^{-1}$, as schematically indicated in fig. 2.4. As indicated in the figure, one observes a light scattering peak shifted by ω_k relative to the incident light frequency. The actual data, shown in fig. 2.5, reveals two magnon peaks in symmetric positions relative to the elastic (Rayleigh) peak. This corresponds to the pair of magnons at ω_k and $\pm k$. The combination of measurements at various k-values yielded $D = 5.4 \times 10^{-9}$ Oe-cm^2, in good agreement with determinations by other methods.

It is also apparent from eq. (2.1) that measurements of ω_k vs. field H at fixed wavenumber can provide useful information. Sandercock and Wettling [20, 21] have shown that such data yield values for $4\pi M_0$ in close agreement with known values for Fe and Ni. The same approach was applied (with

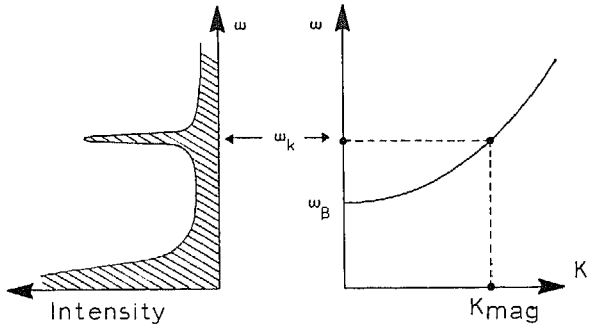

Fig. 2.4. Brillouin scattering on a spin wave.

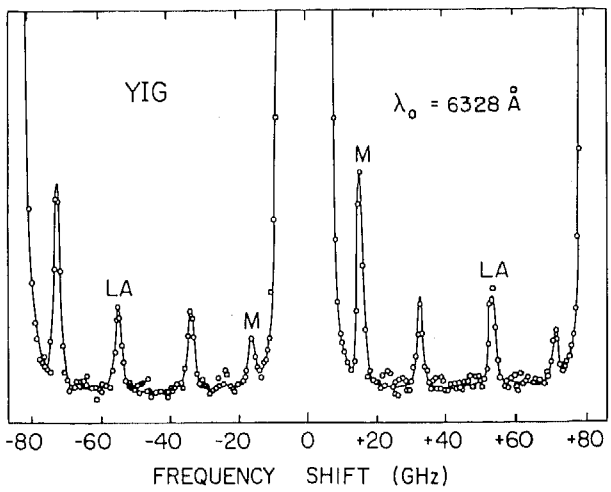

Fig. 2.5. Backscattering data on single crystal YIG (after Sandercock and Wettling [17]).

variations to be discussed later) to thin films of iron and cobalt, as well as various crystalline and amorphous alloys, by Chang et al. [23] and Malozemoff et al. [24, 25]. These later studies demonstrate the potential utility of Brillouin scattering for magnetic characterization. It is often difficult to determine M_0 (and other magnetic parameters) in thin films, foils, and irregular samples by conventional methods. Light scattering, in a number of instances, can yield such determinations with relative ease.

It is to be noted that there is a definite asymmetry between the upshifted magnon line (positive frequency) and the downshifted magnon line (negative frequency). This asymmetry has been related to three physical effects. The first involves the necessity of thermal magnons for anti-Stokes scattering (the destruction of a magnon) but not for Stokes scattering. Simply stated, a magnon must exist in order to be destroyed. The second effect involves quadratic terms in the magneto-optic dielectric tensor. The third effect involves spin correlations. Stokes, anti-Stokes assymmetry for magnon scattering has been discussed at length by a number of authors. Notable among these are the papers by Wettling et al. [18] and Camley et al. [45]. The second process appears to satisfactorily account for the observed assymmetry in YIG. The third appears to be important for absorptive materials such as iron films for

example (Camley et al. [45]). Bates et al. [46] have also discussed anomalous anti-Stokes/Stokes–Raman scattering intensity ratios for antiferromagnetic FeF_2.

2.2. *Magnetostatic modes – Isotropic thick slab*

Turn now to the low k region for which k is on the order of or smaller than the sample dimension S. In the idealized case of large samples with the exchange term of section 2.1 neglected, one obtains the well known magnetostatic modes (Walker [47, 48]; Damon and Eshbach [49]; Röschmann and Dötsch [50]).

The case of an in-plane magnetized slab, first examined by Damon and Eshbach [49], is of particular importance here. A simultaneous solution of the electromagnetic boundary value problem and the magnetic equation of motion (neglecting exchange) leads directly to a set of discrete dispersion curves. These are shown schematically in fig. 2.6 as continuous functions of the in-plane wavevector components k_y (normal to $\boldsymbol{H}$) and k_z (parallel to $\boldsymbol{H}$). The frequencies on the vertical axis are now shown in normalized units following the somewhat accepted notation:

$$\Omega_H = H/4\pi M_0\,, \tag{2.5}$$

$$\Omega_B = \omega_B/\gamma 4\pi M_0 = [\Omega_H(\Omega_H + 1)]^{1/2}\,, \tag{2.6}$$

$$\Omega_S = \Omega_H + 1/2\,. \tag{2.7}$$

The component of $\boldsymbol{k}$ perpendicular to the surface (k_x) is no longer a continuous variable but takes on discrete values allowed by the boundary conditions.

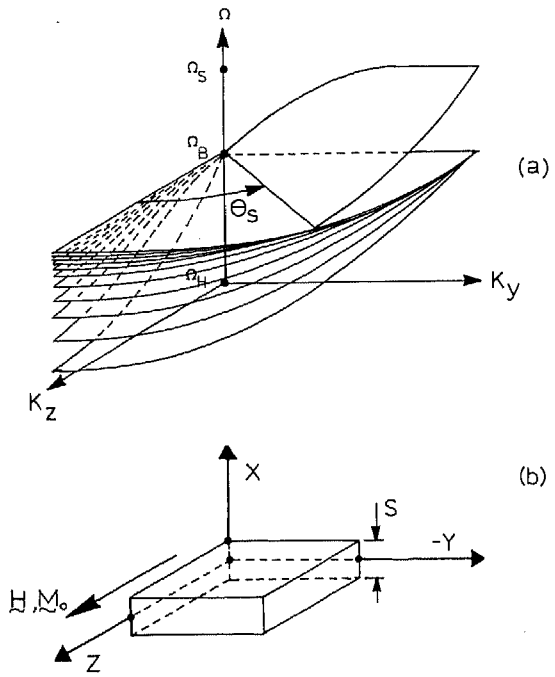

Fig. 2.6. Damon–Eshbach magnetostatic mode dispersion properties.

Consider the gross features of the perspective display in fig. 2.6. The series of sheets which lie between Ω_H and Ω_B correspond to the bulk manifold of fig. 2.1 in the low k limit. For k along $\boldsymbol{H}$ (k_z axis) the family of curves gradually droop from $\Omega = \Omega_B$ to $\Omega = \Omega_H$ at very large k_z. This corresponds to the lower, $\theta_k = 0$ branch in fig. 2.2. Recall that exchange is completely neglected here, so there is no Dk^2 upswing at large k. For k perpendicular to $\boldsymbol{H}$ (k_y axis), this entire family of curves converges to $\Omega = \Omega_B$, corresponding to the upper, $\theta_k = \pi/2$ branch in fig. 2.2. While only six separate curve sheets are shown for purposes of illustration, there is actually an infinity of such sheets, the density of which increases as Ω approaches Ω_B from below. As in the case of the bulk manifold, both positive and negative k values (k in-plane) are allowed. All curves converge to Ω_B at $k = 0$, the usual uniform mode FMR position for in-plane magnetized plates.

The family of volume branches for k along $\boldsymbol{H}$ ($k_y = 0$) is shown in fig. 2.7, along with a schematic indication of the magnetic response over the film thickness in the high k_z, large Ω_H limit. Each curve corresponds to a particular k_x solution, $k_x^n = n\pi/S$, with $n = 1, 2, \ldots$ in the large k_z limit. The solutions represent a set of standing waves across the slab, with different free propagation wavevectors in-plane.

Apart from the obvious standing wave nature of the excitation across the film cross section, it is also noteworthy that the lowest branch curve comes into $\Omega = \Omega_B$ at $k_z = 0$ with a nonzero slope, in contrast with the higher order branches which come in with zero slope. It is easy to show, in fact, that for the lowest branch, the equation

$$\Omega_1 = \Omega_B - \frac{\Omega_H}{4\Omega_B} k_z S \tag{2.8}$$

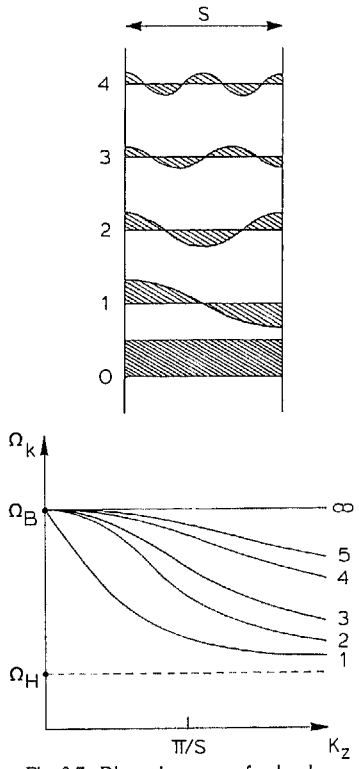

Fig. 2.7. Dispersion curves for $k = k_z$.

is satisfied in the low k_z limit. For the higher order branches, we have

$$\Omega_n = \Omega_B - k_z^2 S^2/(n-1)^2\pi^2 , \qquad n = 2, 3, 4, \ldots . \tag{2.9}$$

We will see later that this same feature is often preserved, even when exchange is included in the analysis to obtain dipole-exchange mode dispersion curves.

The remaining feature in fig. 2.6 which is perhaps of greatest interest is the dispersion sheet which originates at the θ_S cut in the flat volume mode sheet at $\Omega = \Omega_B$ and gradually shifts in frequency to yield the curve shown in fig. 2.8 for k along the k_y-axis. This branch sheet constitutes the well known Damon–Eshbach surface modes, which have several distinctive properties: (1) surface character, (2) nonreciprocal propagation, (3) disappearance at a critical angle, and (4) frequencies above the upper edge of the spin-wave manifold. These properties are discussed below.

The surface dispersion curve in fig. 2.8 is described by

$$\Omega^2 = \Omega_B^2 + [2 + 2\coth(|k_y|S)]^{-1} . \tag{2.10}$$

For $k_y S \gg 1$, Ω tends to a constant value,

$$\Omega = \Omega_H + 1/2 . \tag{2.11}$$

For $k_y S \ll 1$, Ω is a linear function of k_y,

$$\Omega = \Omega_B + k_y S/4\Omega_B . \tag{2.12}$$

For most situations involving light scattering, k (of the magnon) is on the order of $10^5\ \mathrm{cm}^{-1}$ so that the $kS \gg 1$ limit is valid for all but very thin films.

The surface character is indicated in the inset of fig. 2.8. The excitation across the film still constitutes a standing modes of sorts, but the response exhibits an exponential decay from one side of the slab only. The decay constant for pure k_y propagation (as in fig. 2.8) is simply k_y. The propagation

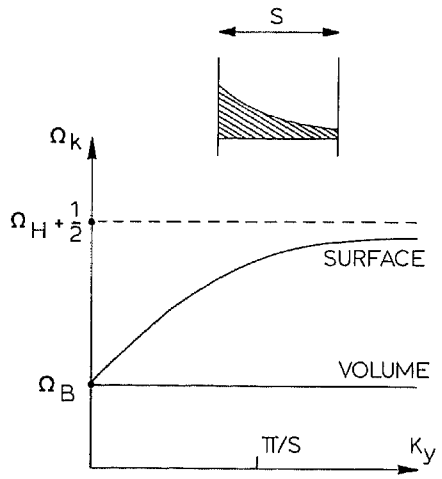

Fig. 2.8. Dispersion for $k = k_y$.

direction associated with the supporting surface at which the excitation is maximum is defined by the direction ($\boldsymbol{H} \times \hat{\boldsymbol{n}}$), where $\hat{\boldsymbol{n}}$ is an outward surface normal. For the slab geometry of fig. 2.6, pure $|k_y|$ surface modes would be directed in the $+y$ direction (to the left) on the upper surface and in the $-y$ direction (to the right) on the bottom surface. If $\boldsymbol{k}$ is rotated toward $\boldsymbol{H}$ by increasing k_z, the decay constant increases and diverges at the angle θ_S indicated in fig. 2.6, given by

$$\tan \theta_S = |k_y/k_z| = \Omega_H^{1/2} . \tag{2.13}$$

At this propagation angle, the surface branch also converges with the volume sheet at $\Omega = \Omega_B$. For iron, permalloy, and YIG at 5 kOe, θ_c is about 13°, 27°, and 71°, respectively. Thus, magnetostatic surface modes can be expected for $\boldsymbol{k}$ within a symmetric sector about the k_y direction, the size of which is determined by the ratio $H/4\pi M_0$.

At first glance, it may appear peculiar that magnetic excitations of any sort are obtained above the upper branch of the bulk spin-wave manifold in the absence of exchange. Actually, the extension of the surface branch in fig. 2.8 to $\Omega = \Omega_H + \frac{1}{2}$ for large k_y is directly related to the zero ellipticity frequency limit of eq. (2.3) for $k = 0$. For the surface mode at large k_y, the precession cones for the surface spins are circular (as pointed out by Damon and Eshbach). This leads directly to the frequency limit of eq. (2.8a).

The frequency bandwidth of the surface mode region from Ω_B to $\Omega_H + \frac{1}{2}$ can vary over a wide range, depending on the field and $4\pi M_0$. Representative values at 5 kOe for YIG ($4\pi M_0 = 1760$ G) and Fe ($4\pi M_0 = 21$ kOe) are 66 Oe and 4.1 kOe (in field units) or 0.185 GHz and 11.5 GHz (in frequency units) respectively. Generally speaking, large spin-wave ellipticity at $\Omega = \Omega_B$ (large $4\pi M_0$) leads to a large surface manifold width.

The magnetostatic mode theory for perpendicular magnetized plates yields rather different results from the parallel case. Treatments appear in two textbooks (Akhiezer et al. [51]; Bar'yakhtar and Kaganov [52]), as discussed by DeWames and Wolfram [53]. The gross features of the volume dispersion branches from the theory are shown schematically in fig. 2.9. With $\boldsymbol{H}$ along the z-axis,

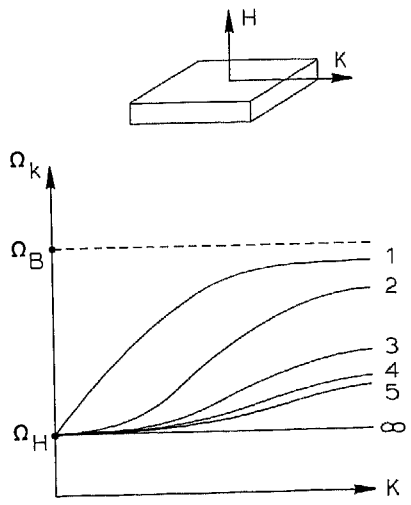

Fig. 2.9. Dispersion for $\boldsymbol{H}$ perpendicular to slab plane.

normal to the surface, x- and y-directions are equivalent ($k_x = k_y = k$). The lowest order branch converges on $\Omega = \Omega_H$ with a nonzero slope, while all higher order branches come in with zero slope, as in the parallel case (fig. 2.7). The curious feature, however, is that the low order branch lies above the higher order branches and the higher order branches effectively condense at $\Omega = \Omega_H$. Thus, in many ways, fig. 2.9 is a "flipped over" version of fig. 2.7. The problem, noted by DeWames and Wolfram [53], is that this "flipped over" magnetostatic manifold does not merge with the bulk manifold of fig. 2.1 (with a large density of states at $\Omega = \Omega_B$) in the high k, low D limit. This problem is eliminated if exchange is included (DeWames and Wolfram [53]; Wolfram and DeWames [54]), as will be discussed in a later section.

There have been several recent reports of Brillouin scattering observations of both volume and surface magnetostatic modes in in-plane magnetized films or plates. These include data on EuO (Grünberg and Metawe [19]), epitaxial Ni films (Metawe and Grünberg [22]), polycrystalline Ni and Fe films and single crystal Fe (Sandercock and Wettling [20, 21]), sputtered films of Fe-B and Co-B (Malozemoff et al. [24]; Grimsditch et al. [9]) and metallic glass ribbons (Chang et al. [23]; Malozemoff et al. [25]).

The most recent data of Sandercock and Wettling [21] on 50 μm plates of mechanically polished polycrystalline iron are shown in fig. 2.10. These data are for a fixed field of 1.9 kOe and a fixed value of $k \sim 1.7 \times 10^5\ \mathrm{cm}^{-1}$, but for various angles θ_k between $\boldsymbol{k}$ and $\boldsymbol{H}$. The spectral features are sharpest for $\theta_k = 90°$, corresponding to k_y propagation. Here, we note two somewhat broad peaks on both sides of the Rayleigh peak, at about ±20 GHz. These correspond to the volume mode line at $\Omega \sim \Omega_B$ in fig. 2.8. The volume peaks are actually a bit above the frequency Ω_B (by 1–2 GHz) due to surface mode interactions and possible exchange effects. A discussion of this problem will be deferred to a later section.

The sharper peak in the spectra of fig. 2.10 corresponds to the nonreciprocal surface branch in fig. 2.8. Since $\pi/S \sim 10^3\ \mathrm{cm}^{-1}$ is much smaller than k, the expected frequency on the scale of fig. 2.8 is $\Omega = \Omega_H + \frac{1}{2}$. This corresponds almost exactly to the peak on the right side at about 34 GHz. Note that

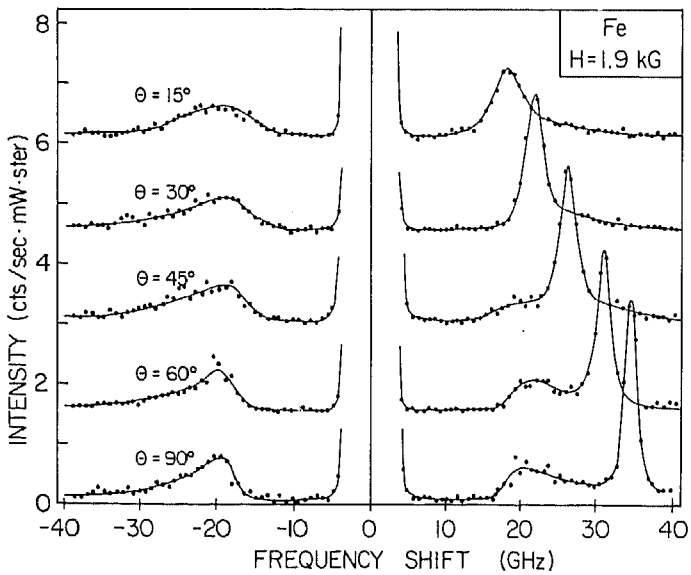

Fig. 2.10. Brillouin scattering data on an Fe plate (after Sandercock and Wettling [21]).

this sharp peak appears only on one side of the spectra, corresponding to one sign for k_y. Consideration of the field polarity and the scattering geometry indicates that the peak should be on the right side. Additionally, reversing the field flips the surface peak to the opposite side of the spectra. Hence, light scattering directly supports the nonreciprocity result of Damon and Eshbach. The upper curves show spectra as the k vector is rotated toward the field direction. As this is done, the surface peak shifts down in frequency and is merged with the volume peak at $\theta_k = 15°$. This is precisely the effect expected from the shape of the surface branch surface in fig. 2.6. The surface peak position vs. angle is shown in fig. 2.11, along with the expectation from the Damon–Eshbach theory. The dotted line indicates θ_S for iron. The agreement is seen to be excellent.

The data of Metawe and Grünberg [22] for Ni films of various thickness provide one further result of interest. Recall that the decay length of the surface modes for k_y propagation is k_y^{-1}. This length is on the order of a few thousand Ångstroms, depending on the experimental details. In films somewhat thinner than this value, one would expect the surface mode to leak through from the supporting surface to the other surface. This is precisely the observation as shown in fig. 2.12. The volume mode is presumably so close to the surface mode (2.5 GHz) and so broad that it is not resolved.

All of the scattering data which reveal surface peaks involve either light penetration depths which are relatively small (~150 Å for bulk metals and ~1000 Å for EuO) or very thin films. This is reasonable. If the scattering region is large compared to the decay length of the surface mode (~6000 Å for $k = k_y \sim 10^5\ \mathrm{cm}^{-1}$), the signal from the volume modes is likely to swamp the surface mode scattering. As briefly indicated in section 2.1, Brillouin scattering is a useful tool for the characterization of magnetic materials. It was shown that appropriate experiments could determine the exchange constant D, if γ

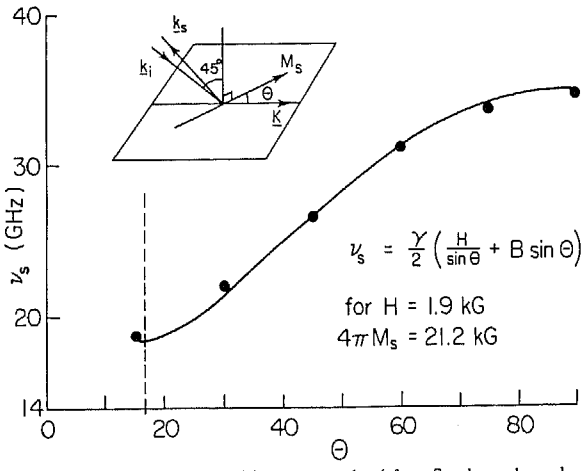

Fig. 2.11. Surface peak position vs. angle (after Sandercock and Wettling [21]).

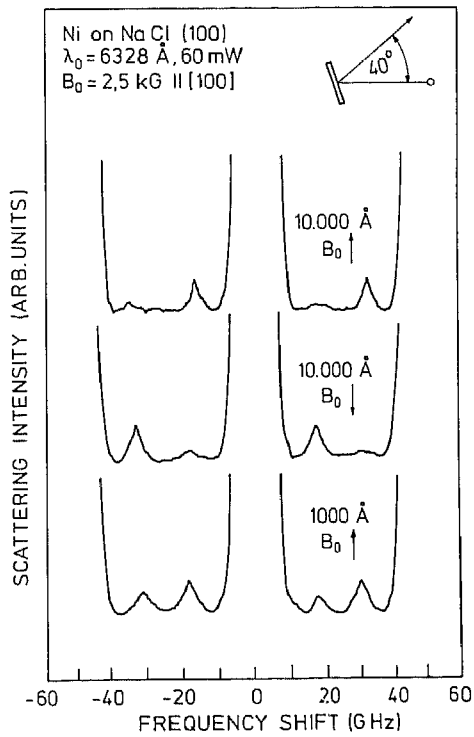

Fig. 2.12. Brillouin scattering in Ni films of various thicknesses (after Metawe and Grünberg [22]).

and $4\pi M_0$ were known, etc. By combining the properties of both the surface and volume modes, the gyromagnetic ratio (or equivalently, the g-factor) and the saturation induction $4\pi M_0$ can be deduced. This capability stems from the fact that the surface mode frequency in the high $k = k_y$ limit,

$$\omega_k^{(s)} = \gamma(H + 2\pi M_0)\,, \tag{2.14}$$

is linear in field. The slope of $\omega_k^{(s)}$ vs. H gives γ directly. If the Dk^2 term in the bulk dispersion is small compared to H and $4\pi M_0$ (as is often the case), the volume mode frequency,

$$\omega_k^{(v)} = \gamma[H(H + 4\pi M_0)]\,, \tag{2.15}$$

is not linear in field. Consequently, $4\pi M_0$ is deduced by a fitting procedure which utilizes the γ value determined from $\omega_k^{(s)}$ vs. H.

Essentially this procedure was used by Sandercock and Wettling [21] for light scattering data on Fe and Ni discussed above. Their results are presented in fig. 2.13. The fits are very good for Ni and reasonable for Fe. In the latter case, the volume mode data are above the calculated curve by a few GHz. This may be due to volume–surface mode interactions, as proposed by Sandercock and Wettling [21] or simply due to exchange (Malozemoff et al. [24]). Chang et al. [23] has applied essentially this procedure to characterize amorphous $Fe_{80}B_{20}$ ribbons. A more elaborate fitting procedure which

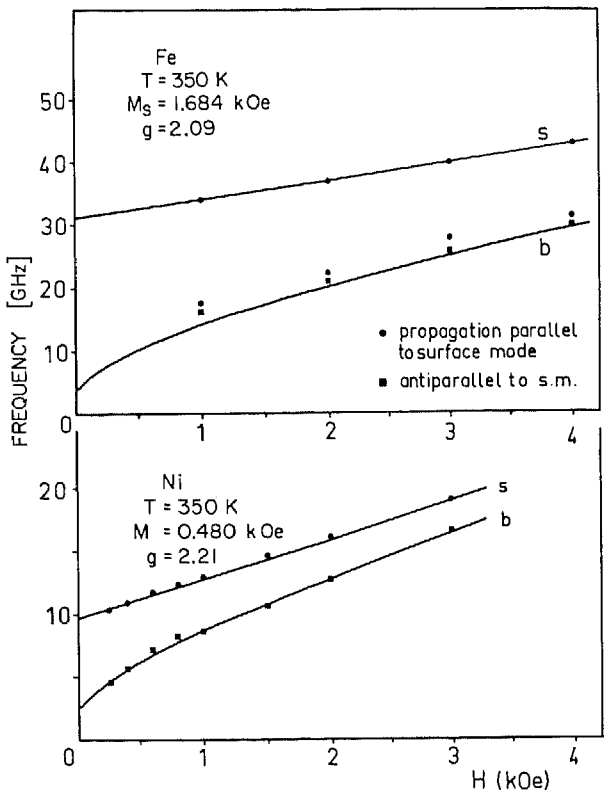

Fig. 2.13. Surface and volume mode frequencies vs. field for Fe and Ni thin plates (after Sandercock and Wettling [21]).

included the Dk^2 exchange terms as an additional parameter for the volume mode was used by Malozemoff et al. [24, 25] to characterize a variety of sputtered films (Fe-B, Co-B) and metallic glass ribbons. Exchange and additional complications will be considered in succeeding sections.

2.3. Dipole-exchange modes – Isotropic thin slab

From the preceding discussion, several questions can be asked:

(1) What is the effect of exchange on the magnetostatic mode spectra?

(2) What happened to the surface modes in the bulk limit?

In this section, the first question is considered. The second is examined in section 2.4.

The theoretical problem of dipole-exchange modes, or the calculation of the properties of magnetic excitations when both surface dipole and exchange interactions are included (in addition to the volume dipole interaction), has been treated both macroscopically and microscopically. The emphasis here will be on the macroscopic theories of Wolfram and DeWames cited in the Introduction. Microscopic theories and their relation to macroscopic results are discussed and reviewed by Wolfram and DeWames [55, 5].

The macroscopic approach of Wolfram and DeWames is simple in concept. One includes exchange fields in the formulation of Damon and Eshbach, solves the equation of motion in combination with Maxwell's equations subject to surface boundary conditions, and generates a series of discrete normal mode dispersion curves in the spirit of those presented in section 2.2. Though the mathematics is formidable, with cumbersome eigenvalue equations which require numerical solution, a number of the basic results can be obtained intuitively by simply adding a Dk_x^2 exchange term, with appropriate k_x values for the various branch curves of the previous section. This approach is utilized, where appropriate, in the discussion to follow.

The case of in-plane magnetized, isotropic thin films with no surface spin pinning (Wolfram and DeWames [56]; DeWames and Wolfram [53]) provides for a natural extension of the Damon–Eshbach results. The equivalent dispersion sheets of fig. 2.6, when exchange is included, are shown in fig. 2.14. We can see, after careful examination, two important effects. First, the degeneracy of the volume branch sheets at $\Omega = \Omega_B$ and $k_z = 0$ is lifted completely. Second, the single surface branch sheet in the Damon–Eshbach theory is now "shared" by the volume branch sheets in the regions of (Ω, k_y, k_z) space where the new volume sheets section the old surface sheets. In other words, the surface sheet acts as a transition between adjacent volume sheets.

Both features can be more easily visualized by considering the $k = k_y$ $(k_z = 0)$ family of dispersion curves, shown schematically in fig. 2.15. These results, upon examination, are intuitively reasonable. First of all, in the limit of low k_y, the k_x values for the numbered exchange branches are simply

$$k_x^{(n)} = n\pi/S. \tag{2.16}$$

The upward shift of the numbered volume branches from Ω_B at $k_y = 0$ is simply due to the $k_x^{(n)}$ contribution to the Dk^2 term in the dispersion relation of eq. (2.1). The surface branch at $k_y = 0$, however, has an infinite decay length (k_y^{-1}) across the film, and is just the uniform mode observed in FMR. There is *no* exchange shift for this branch point at $k_y = 0$. The corresponding frequencies Ω_0 (for the surviving surface branch and Ω_n $(n = 1, 2, 3, \ldots)$) at $k_y = 0$ give rise to the usual FMR and spin-wave resonance peaks observed in parallel FMR.

Ignoring the interactions between the exchange (or volume) branches and the surface branch for the

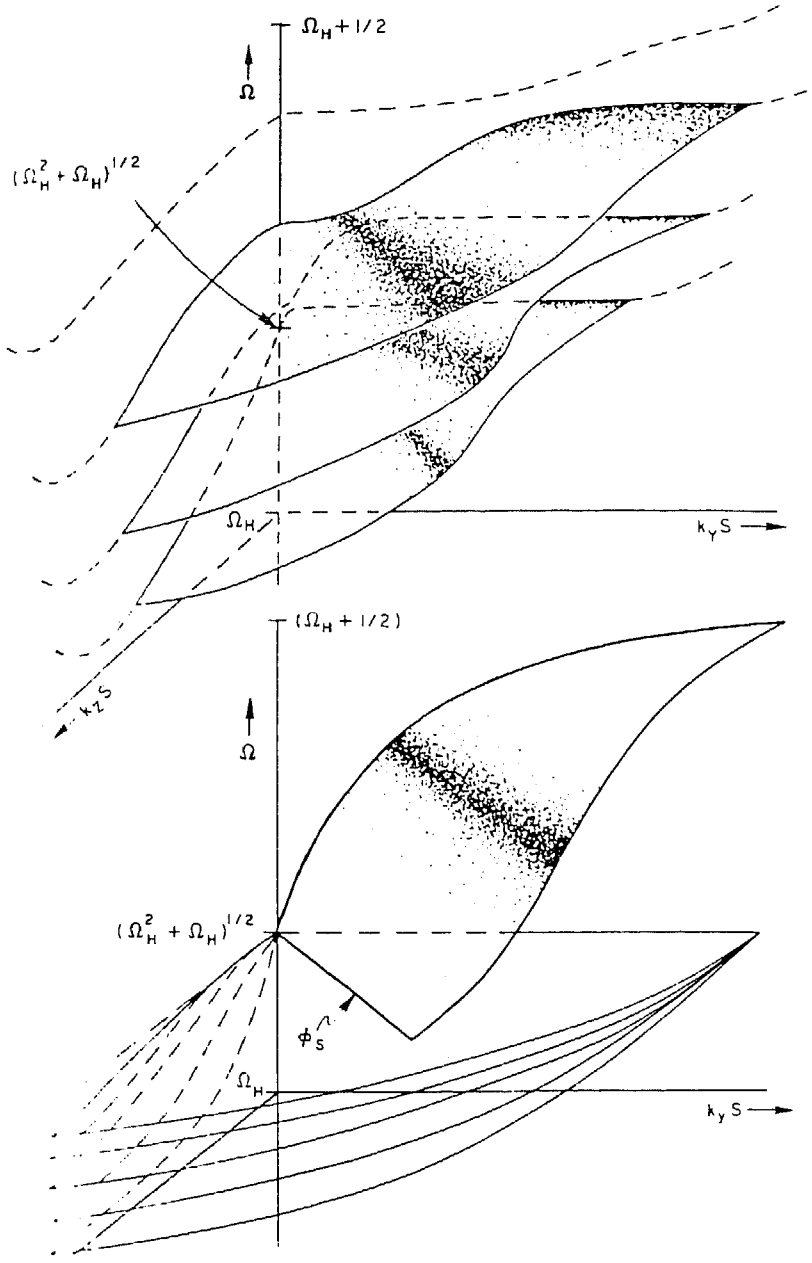

Fig. 2.14. Dispersion surfaces for dipole-exchange modes (upper) and magnetostatic modes (lower) (after Wolfram and DeWames [56]).

moment, consider the k_y contribution to the Dk^2 exchange term in the dispersion. For the volume branches, the shifts at $k_y = 0$ already account for the k_x contributions, so the upward curvature as k_y increases goes as Dk_y^2 (for small k_y). Hence, eq. (2.1) applies with $\theta_k = 90°$ and

$$k^2 = (n\pi/S)^2 + k_y^2\,, \qquad n = 1, 2, \ldots \tag{2.17}$$

as noted by DeWames and Wolfram [53].

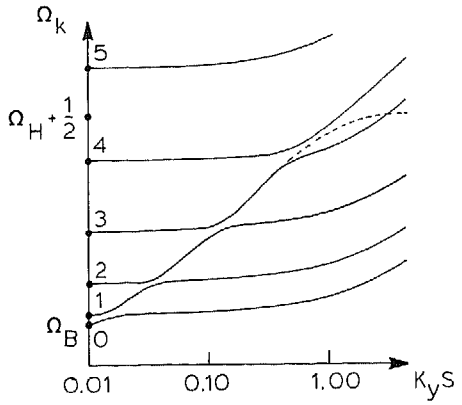

Fig. 2.15. Dipole-exchange mode dispersion for in-plane magnetized slab and no surface spin pinning (after DeWames and Wolfram [53]).

For the surface branch, however, the decay length varies as k_y^{-1} and the effective x-component of $\boldsymbol{k}$ is on the order of k_y. The appropriate exchange term is therefore

$$Dk^2 \approx 2Dk_y^2 . \tag{2.18}$$

If this term is added to the magnetostatic surface mode dispersion relation of section 2.2, one obtains

$$\Omega = \Omega_B + k_y S/4\Omega_B + 2\tilde{D}k_y^2 \tag{2.19}$$

for $k_y S \ll 1$, and

$$\Omega = \Omega_H + \tfrac{1}{2} + 2\tilde{D}k_y^2 \tag{2.20}$$

for $k_y S \gg 1$. In both cases k_y is small and $\tilde{D}$ is a normalized exchange, $\tilde{D} = D/4M_0$. In the $k_y S \ll 1$ result, the quadratic term is usually negligible (for accessible experimental conditions) and the magnetostatic expression of eq. (2.12) is adequate.

The result for $k_y S \gg 1$ (satisfied for many typical experimental conditions) shows that the effective exchange constant for the k_y dipole-exchange surface wave is enhanced by a factor of two, and is due to the correlation between the attenuation factor in the x-direction and the propagation factor (k_y) in the y-direction. The same result is obtained by a quantitative calculation for a semi-infinite slab (Wolfram and DeWames [57]). In the numerical analysis of Camley and Mills [8], the enhancement factor was found to be 1.76. The semi-infinite slab limit will be examined more closely in the next section.

As the numbered exchange branches thread the upward sloping surface branch, the Wolfram–DeWames theory shows that the intersecting branches repel each other. The resulting cross-over effect is exaggerated in fig. 2.15 for purposes of illustration. At large k_y, exchange shifts cause the surface branch to curve upward along with the volume branches and lose its distinctive character. The dotted line is simply a reminder of the shape of the original Damon–Eshbach surface mode dispersion.

Given the multiplicity of the exchange branches and the branch repulsions shown in fig. 2.15, it is clear that exchange modifies the thin film dispersion substantially from that of fig. 2.8. The question now arises: What curve (or curve segments) in fig. 2.15 corresponds to surface modes? A study of the mode

shape across the film (Wolfram and DeWames [58]) indicates three plausible trends:

(i) For regions of the curves which have exchange character, as on curves $1, 2, \ldots$ away from cross-over regions, the modes are volume-like and reciprocal.

(ii) Regions on the surface line curve away from cross-over regions, the modes are surface-like and nonreciprocal.

(iii) The surface-like character of any mode tends to diminish as the frequency increases.

It is clear from the preceding discussion that the mode shapes which lead to the indicated mode frequencies at $k_y = 0$ in fig. 2.15 are not possible if the spins at the film surfaces are pinned. These mode shapes and their pinned counterparts are schematically indicated in fig. 2.16. For the "unpinned" modes, mode "0" is the surface mode at Ω_B, and modes 1, 2, 3, ... are the volume or exchange modes discussed above. Mode "0" is just the uniform FMR mode.

For complete pinning, a uniform mode is no longer allowed. The lowest order allowed mode for pinned surface spins has $k_x \approx \pi/S$ as indicated by the right-hand counterpart to mode one. We can see, as pointed out by Wolfram and DeWames [59], that complete pinning precludes the existence of a surface mode branch originating at Ω_B. Their detailed theory shows that the first allowed nonpropagating mode ($k_y = 0$) sits at Ω_1. All of the odd modes at $k_y = 0$ resemble the unpinned counterparts, insofar as the number of "half wavelengths" across the thickness is given by n. They differ from the unpinned counterparts in that the x-variation is not purely harmonic. The even $k_y = 0$ modes are essentially the same as for no pinning, except that nodes rather than antinodes occur at the surfaces. The sketches in the right part of fig. 2.16 attempt to convey the spirit of these features.

The branches themselves, as a function of k_y are also changed significantly, as indicated schematically in fig. 2.17. The essential new or modified features can be seen by comparing the curves for "no pinning" (repeated from fig. 2.15) with the curves for "complete pinning". These are as follows:

(1) The surface mode starting at Ω_B is no longer present.

(2) The odd volume modes manifest some surface character insofar as the initial increase with k_y is linear. The slope decreases as n^{-2}.

(3) The even modes have essentially the same dispersion character in both cases.

The details of the calculation are given by Wolfram and DeWames [59]. A more systematic review of

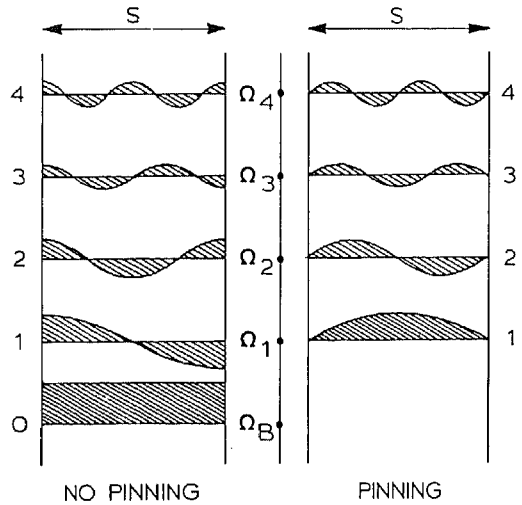

Fig. 2.16. Possible mode configurations.

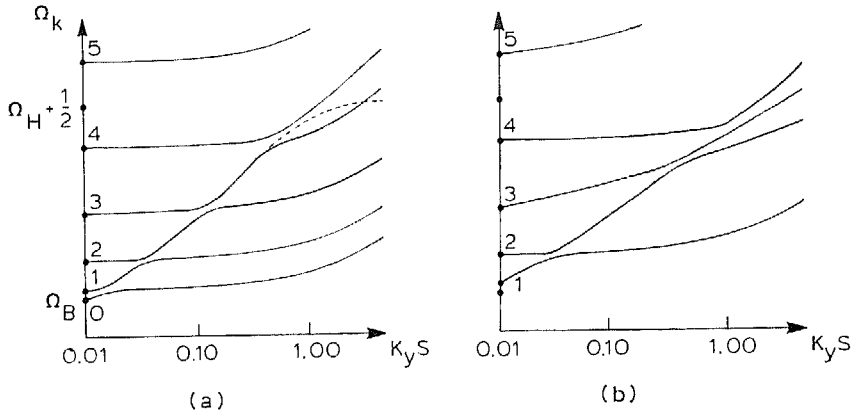

Fig. 2.17. Effect of complete pinning on dispersion curves. (a) No pinning. (b) Pinning.

pinning concepts will be given in section 3. The point to be made here is that the boundary conditions on the magnetization (or spins) at the surface of the sample can modify the dispersion relations for thin films substantially. Any method that can be used to measure these mode positions constitutes a powerful tool to probe surface magnetism.

Similar results have been obtained for thin films magnetized normal to the surface (DeWames and Wolfram [60, 53]; Wolfram and DeWames [54]). The main points have already been made within the context of the parallel case, so a detailed elaboration is not justified here. It is important, however, to show the important features and their relation to the previous discussion.

The basic dispersion curves which constitute the exchange augmented branches of fig. 2.17 are shown in fig. 2.18. As in the parallel case, we have a branch with an initial nonzero slope (labeled "0") which originates at the uniform mode FMR frequency (Ω_H for perpendicular magnetization and field). We also have other branches with zero initial slope which are shifted upward in frequency. These shifts, as in the parallel case, are due to the k_x contribution to the exchange term in the dispersion relation of eq. (2.1). For k (the in-plane k) = 0, we have $\theta_k = 0$ in eq. (2.1) and the dispersion is just

$$\Omega^{(n)} = \Omega_H + \tilde{D}(n\pi/S)^2, \qquad n = 0, 1, \ldots \tag{2.21}$$

since $k_x^{(n)} = (n\pi/S)$ at k(in-plane) = 0. These are the usual spin-wave resonance frequencies which are studied so extensively in permalloy films over the past two decades.

There are two major differences from the parallel case (apart from the shift of $\Omega^{(0)}$ from Ω_B to Ω_H and θ_k from 90° to 9° for $k = 0$). First, the branch repulsions are between even branches only, or between odd branches only. Second, there is no branch with k_x purely imaginary which can be identified as a surface mode. DeWames and Wolfram [60, 53] did find, however, that over limited regions of k for the two lowest branches, the corresponding k_x solutions are complex, that is, the corresponding modes can have a surface-like character. Those regions are indicated by the heavy blacked-in portions of the dispersion curves in fig. 2.18. These quasi-surface modes are reciprocal, in that the amplitude is large at both surfaces. Both symmetric and antisymmetric modes occur.

The problem of spin pinning and the effect on the dispersion in the perpendicular case was also considered (Wolfram and DeWames [54]). The results are similar in spirit to those for parallel magnetized slabs: (1) The lowest order branch is displaced up from the intercept at the FMR frequency

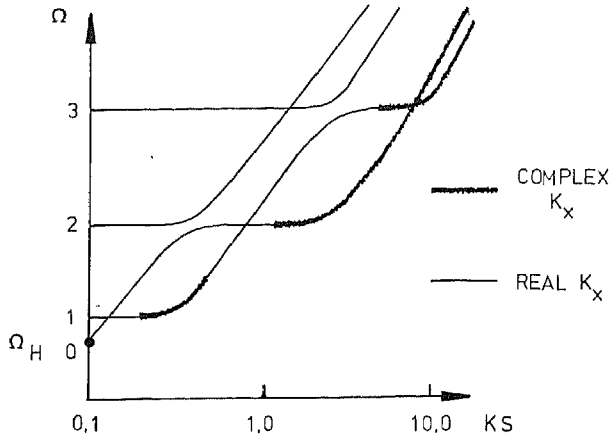

Fig. 2.18. Dispersion curves for H perpendicular to slab.

($\Omega^{(0)}$) to an intercept at $\Omega^{(1)}$. (2) The initial slope of $\Omega^{(n)}$ vs. k for all odd branches is nonzero, and diminishes as n^{-2}. (3) Even branches have a quadratic k dependence (and zero initial slope) as in the unpinned case.

The study of nonpropagating modes (those with $k_y = k_z = 0$) dates back to the initial prediction of standing spin-wave resonance in thin films by Kittel [1] and the observation of such resonances by Seavey and Tannenwald [2]. Their initial FMR observation for a 5600 Å permalloy film at 8.89 GHz in the perpendicular configuration is shown in fig. 2.19. The (approximate) quadratic spacing below the main peak and the strong–weak–strong alternation in intensities are qualitatively consistent with the dispersion curve intersections at $k = 0$ in fig. 2.18 and the even–odd–even alternation in mode shapes of fig. 2.16. (Recall that the microwave excitation in FMR is uniform, so that coupling is strongest for even modes.)

The above phenomena gave birth to an extensive research effort to understand the detailed behavior

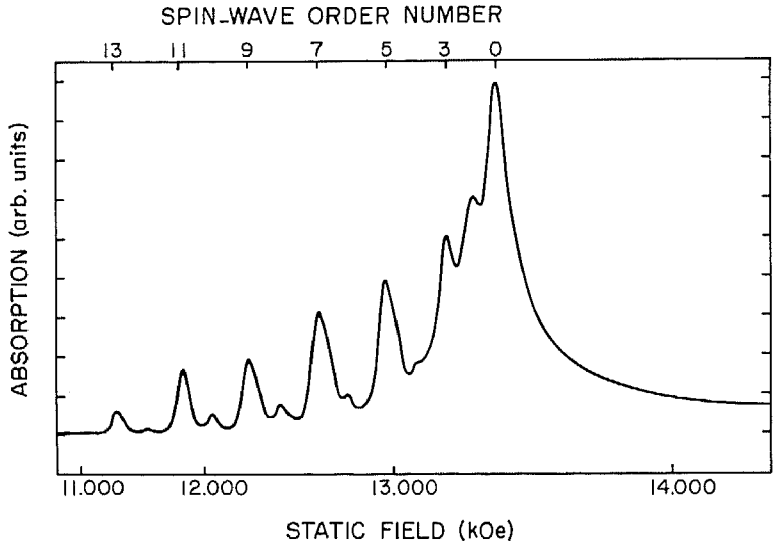

Fig. 2.19. Standing spin-wave resonance modes in permalloy (after Seavey and Tannenwald [2]).

of standing spin waves in films. Data have been reported for metallic films, insulator films, multilayer films, etc., for field configurations from parallel to perpendicular and a wide variety of surface conditions. Attempts to explain these data have involved partial pinning models, dynamic pinning models, volume inhomogeneity models, critical angle effects, tensorial surface anisotropy, etc. A complete review is not appropriate here. Some limited aspects of surface anisotropy and pinning will be discussed in section 3. The subject has been reviewed by Frait [61], Weber [62], Puszkarski [3, 63], and Wigen et al. [4] among others.

There has been, however, FMR confirmation of some of the gross properties for dipole-exchange modes predicted by Wolfram and DeWames. Notable among these is the experimental evidence for branch repulsion by Henry et al. [7]. Their data, obtained for 1.15 μ thick YIG films in the perpendicular orientation, are shown in fig. 2.20. The vertical axis may be taken as a reduced frequency. The in-plane wavenumber k_ρ (for standing waves) was controlled by varying the film diameter and associating particular resonance peaks with roots of the zero-order Bessel function, $J_0(k_\rho r) = 0$. The mode repulsion, reminiscent of that in fig. 2.18, is evident. Fits to the theory of $n = 1$ and $n = 3$ (even branches) are indicated by the solid lines.

A number of light scattering studies of standing volume and surface modes in thin films have been reported in the recent literature. Grünberg [64], Grünberg et al. [65, 37] have presented data on films of Fe, Ni, and $Ni_{0.8}Fe_{0.2}$. From spectra for Fe films ranging in thickness from 200–1500 Å, they were able to discern cross-over and mode repulsion between the volume and surface modes. Wettling and coworkers [66] have observed surface magnons on epitaxial iron films grown on GaAs substrates. Camley and Grimsditch [67] have made a detailed comparison between experimental and theoretical spectra and find excellent agreement for mode positions and cross-over behavior as a function of magnon propagation direction.

Similar but more complicated spectra have been obtained for amorphous metallic films by Chang et al. [23], Malozemoff et al. [24, 25], and Grimsditch et al. [68]. The attendant problems connected with

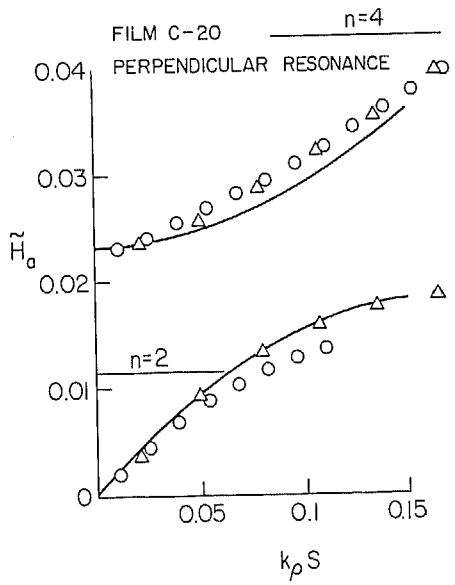

Fig. 2.20. Mode repulsion in single crystal YIG films (after Henry et al. [7]).

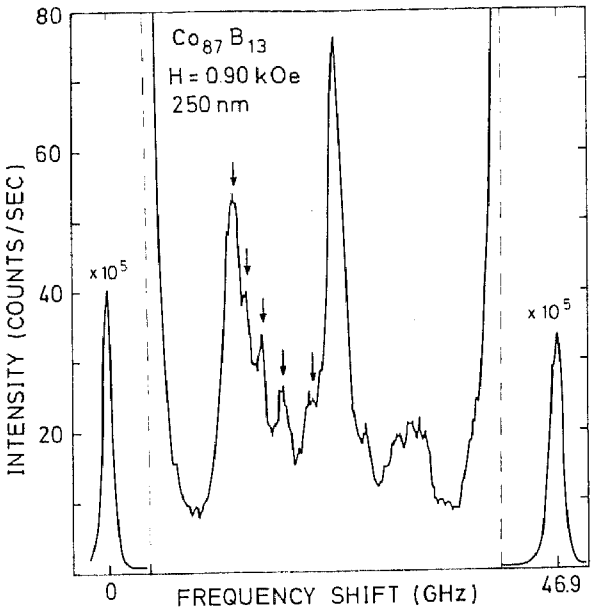

Fig. 2.21. Brillouin scattering spectra in an CoB amorphous film 2500 Å thick (after Malozemoff et al. [24]).

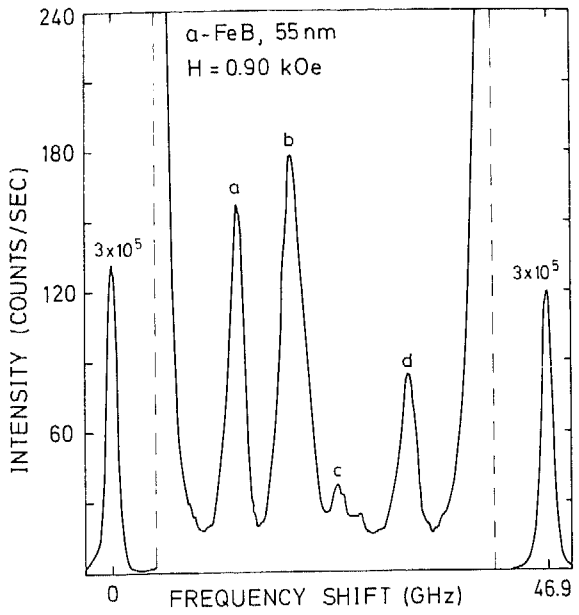

Fig. 2.22. Brillouin scattering in FeB amorphous film, 500 Å thick (after Malozemoff et al. [24]).

limited free spectral range (~23 GHz) and magnon linewidth apparently precluded unambiguous mode identification. The data on amorphous $Co_{87}B_{13}$ are shown in fig. 2.21. To quote the authors, "the regularity of these structures is reminiscent of standing spin waves often observed in ferromagnetic resonance". The modes identified by the arrows, if they are in fact standing spin-wave modes corresponding to the exchange branches of fig. 2.15 (or fig. 2.17), must be rather high order modes because of their large spacing ($n > 10$).

The same authors presented similar data for amorphous FeB films 550 Å in thickness, for which the multiple peaks are well resolved. See fig. 2.22. The problem here is that adjacent spin-wave peaks for n = 1–5 would be spaced 12, 17, 22, and 26 GHz apart, respectively. Peaks a and c are about 12 GHz apart, as are b and d. These may correspond to Stokes–anti-Stokes pairs. Peaks b and c appear to be "surface-like" in that they shift linearly with field. A nonlinear dependence would be expected for spin-wave branches. As the authors point out, however, it is likely that the inference of surface character based on eqs. (2.10) or (2.20) which assume $k_y S \gg 1$ is not entirely justified for such thin films. Equation (2.19), with a rather complex field dependence, would be a better choice. This makes the observed linear dependence even more perplexing.

Theoretical advances include extension of the theory for semi-infinite geometry by Camley and Mills [8] (to be discussed shortly) to the thin film case by Camley et al. [69] and Rahman et al. [70] and detailed comparisons of theoretical spectra with experimental data. Comparisons are made with the data of Grimsditch et al. [9]. The agreement is quite reasonable. Since the theory is evaluated numerically by computer, problems of mode identification, etc., are not encountered.

2.4. Dipole-exchange modes – Isotropic thick slab

One rather important result concerning dipole-exchange magnetic excitations remains to be considered. This involves the effect of increased film thickness. The extreme case, that of a semi-infinite

medium, is of importance both experimentally and for theoretical reasons. Light scattering from surfaces of bulk samples makes for a straightforward experiment on easily obtainable samples in many cases. Theoretical analysis is often easier when only one surface is present. This limit is applicable to much of the published data (Grünberg and Metawe [19]; Sandercock and Wettling [20, 21]) and theoretical results (DeWames and Wolfram [71]; Wolfram and DeWames [57]; Camley and Mills [8, 72]).

The evolution of the dispersion character for the in-plane magnetized slab and k_y modes is shown in fig. 2.23. Cross-over and branch repulsion effects (fig. 2.15) are ignored for the moment. The usual widely spaced volume branches, exchange shifted because of the discrete k_x values ($n\pi/S$, $n = 1, 2, \ldots$), and the surface branch emanating from Ω_B are evident for the "thin slab" limit in fig. 2.23a. This and related dispersions were the subject of section 2.3.

Figure 2.23b shows the changes (schematically) for a slab about 10 times thicker than in fig. 2.23a. We see two obvious effects: (1) the "knee" of the "surface" branch moves to lower k (by a factor of 10), (2) the volume branches condense toward Ω_B (at $k_y = 0$). Carried to the semi-infinite limit in fig. 2.23c, the surface branch now emanates from $\Omega = \Omega_H + \frac{1}{2}$ in the $k_y = 0$ limit (for all practical purposes), and the volume branch condensation yields a continuum of modes as indicated. In the analytical theory, Wolfram and DeWames [57] obtain the surface branch dispersion in the semi-infinite slab limit as

$$\Omega_k = \Omega_H + \tfrac{1}{2} + 2\tilde{D}k_y^2 . \tag{2.22}$$

This is identical with the intuitive result obtained in section 2.3 for $k_y S \gg 1$ (eq. (2.20)). The bottom edge of the continuum obeys the usual equation for the upper branch of the bulk manifold. It is important to keep in mind that this "continuum" derives from the Dk_x^2 exchange terms, with k_x quasicontinuous in the thick slab limit.

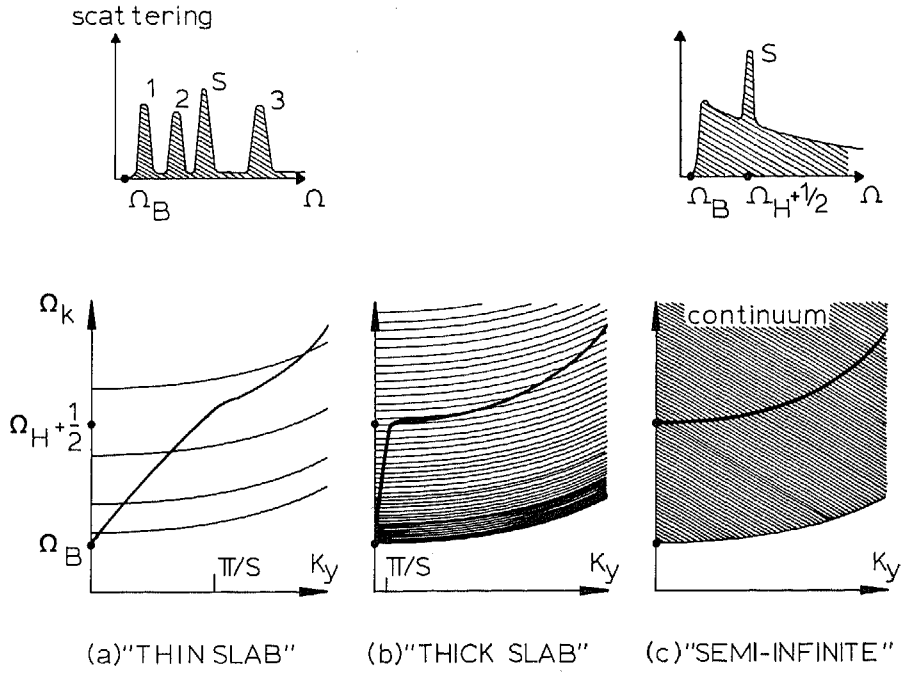

Fig. 2.23. Dispersion evolution for increasing slab thickness for in-plane magnetized slabs and k_y propagation.

The sketches in the upper part of fig. 2.23 indicate the anticipated change in the Brillouin scattering spectra (at fixed, moderate k). The "thin slab" spectra consists of distinct peaks, much like those in fig. 2.22. In the semi-infinite slab limit, we see that the possibility of observing structure is diminished. We anticipate one well resolved surface peak superimposed on a broad peak with a shoulder near Ω_B and a long high frequency tail. Although there are some quantitative differences, the data in fig. 2.10 for bulk iron are not too different from the sketch in fig. 2.23c.

The theoretical analysis of both Wolfram and DeWames [57] and Camley and Mills [8] indicate that the continuum of volume states leads to a k-dependent broadening of the surface mode. The relaxation rate (imaginary part of Ω_k) for the surface branch was found to be

$$|\Omega''| = 4[2(\Omega_H + \tfrac{1}{2})^{1/2}\tilde{D}^{3/2}k_y^3 \tag{2.23}$$

in the Wolfram–DeWames analysis. The Camley–Mills numerical calculations yielded a surface mode linewidth which increases with frequency (and hence with k) as indicated in fig. 2.24. We see that the line-broadening increases substantially as the critical angle for surface mode propagation (θ_S) is approached. Various physical interpretations of the above surface-mode broadening have been offered. Wolfram and DeWames [57] connect it with the necessary admixture of surface and volume character for the dipole-exchange branches as discussed in section 2.3. This admixture manifests itself, in the semi-infinite slab limit, as a "leaky" surface wave which loses energy to degenerate volume modes. This interpretation is similar, in spirit, to the well known two-magnon scattering relaxation mechanism due to localized scattering inhomogeneities which admix or renormalize the Holstein–Primakoff spin waves. Camley and Mills [8] refer to this scattering as "radiative damping".

Some rather illuminating numerical results on the same problem have been obtained by Camley and Mills [8, 72]. Their approach was to calculate a spectral density function $A(k, \Omega; x)$ (in our notation)

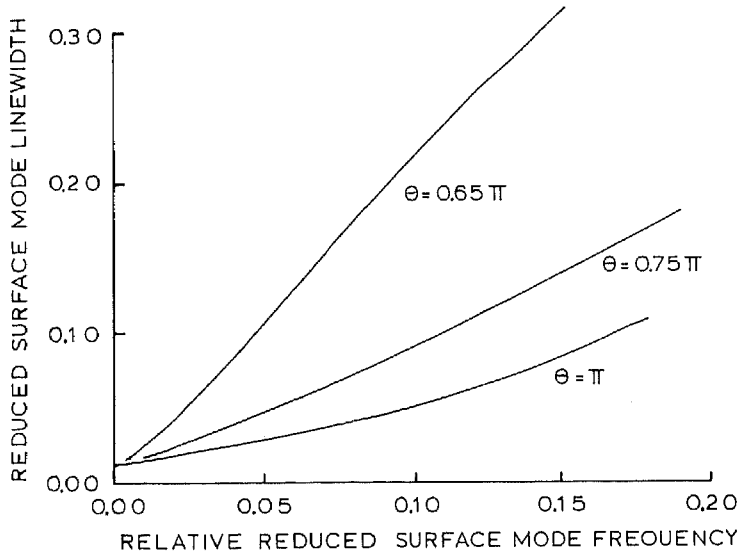

Fig. 2.24. Frequency and angle dependence of surface mode linewidth for the semi-infinite slab. $\omega(0)$ corresponds to Ω_B (adapted from Camley and Mills [8]).

which is simply a measure of the spatial-temporal component of the thermal spin fluctuation at wave-vector $\boldsymbol{k}$ (in plane) and frequency Ω, a distance x into the slab. Plots of A vs. the various parameters in the variable list allow one to map out the magnetic excitations of the magnetic system. Interestingly, A vs. Ω is almost exactly the kind of information one gleans from a Brillouin scattering experiment.

The spirit of their results, adapted for k_y propagation, is indicated in fig. 2.25. Each curve of A (spectral density) vs. Ω at fixed k_y is essentially a measure of the spin-wave excitation amplitude at k_y and the penetration distance indicated versus Ω. It is easy to see that the distribution depends on penetration depth rather significantly.

At the surface, $x = 0$, the spectral density shows one sharp peak at $\Omega \gtrsim \Omega_H + \frac{1}{2}$, corresponding to the surface mode, and a small reduced background extending upward in Ω from Ω_B. This background is the signature, at the surface, of the continuum of volume modes. As we move into the interior of the slab, the surface peak diminishes in prominence and is not resolved for $x > \lambda_k$. At the same time, the continuum spectral density evolves in a complex way from a spectrum with a few prominent, if broad, peaks, to a spectrum with a multitude of rapid oscillations, and finally to a smooth continuum at $x = \infty$. At $x = \infty$, corresponding to the interior of the slab, one encounters the prominent shoulder at $\Omega \sim \Omega_B$ and the high frequency tail corresponding to the continuum. The actual results of Camley and Mills, for $\theta_k < 90°$, show additional features of the spectra which are not considered here. The essential result for our purposes is the strong variation in the magnon spectral density with distance into the slab, as evident from the above discussion.

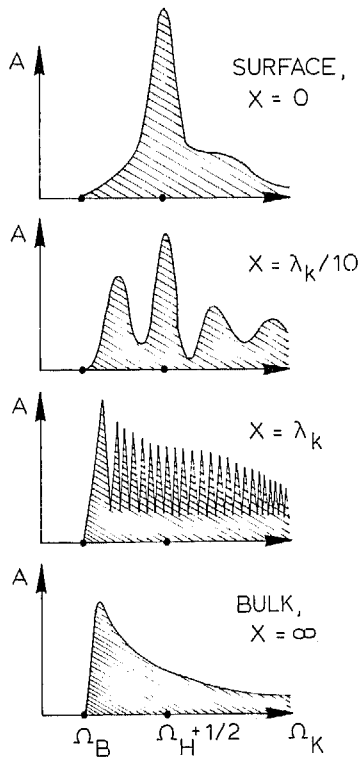

Fig. 2.25. Schematic representation of spectral density vs. frequency at various depths into the in-plane magnetized semi-infinite slab for k_y-propagation at moderate k_y (adapted from Camley and Mills [8]).

The remaining numerical calculations by Camley and Mills focus on the surface spectral density as a function of the (in-plane) propagation angle θ_k, the propagation wavenumber k, and various pinning conditions for the surface spins. Very briefly, these theoretical results are as follows:

(1) The surface mode (at low k) shifts down in frequency as the propagation angle is decreased from 90° to the critical angle θ_S. At $\theta_k \sim \theta_S$, the peak merges with the bulk manifold. These properties are expected from and consistent with the Damon–Eshbach theory.

(2) Concurrent with the above shift, the linewidth of the surface mode broadens as the critical angle is approached. As the k of the mode is increased, the broadening starts sooner (e.g., at larger θ_k). In line with the Wolfram–DeWames results on "leaky surface waves" at $\theta_k = 90°$, this result indicates that the damping due to interaction with the continuum bulk states also increases as Ω_S approaches the bulk manifold at Ω_B. We note, from fig. 2.25, there is a peak in the spectral density near Ω_B in the bulk.

(3) As the wavenumber k is increased, the position of the surface mode shifts up in frequency. For $\theta_k = 90°$, the numerical data support eq. (2.22) if the $2\tilde{D}k_y^2$ term is replaced by $1.76\tilde{D}k_y^2$. The linewidth also increases with k_y.

Other results on the effect of surface spin pinning on the surface mode character are also presented. This subject is deferred to section 3.

Further calculations in the same paper by Camley and Mills relate aspects of the above magnon dispersion to theoretical Brillouin scattering. Rather than limit the closing discussion in this section to data only, an integrated overview of these theoretical results with some of the data already mentioned is given below.

A representative theoretical curve for an "Fe-like" slab is presented in fig. 2.26. The vertical axis is scattered intensity and the horizontal axis is frequency in normalized units relative to the Rayleigh peak. Curves are for three propagation angles; the ϕ values for (a), (b), and (c) correspond to $\theta_k = 36°$, 27°, and 18°, respectively, with θ_c (the critical DE angle) at 21.6°. The gross features of these curves are in excellent agreement with the data of Sandercock and Wettling [21] in fig. 2.10. The shapes of the bulk magnon peaks are similar, and the behavior of the single surface peak is similar. Notable are the high frequency tails for both the experimental and theoretical bulk modes. Presumably, this is connected with the "bulk continuum" for the semi-infinite slab (fig. 2.23c) and the tail in the spectral density for $\nu = \infty$ in fig. 2.25.

Camley and Mills note that the peaks for both the surface and bulk modes are upshifted due to exchange and that the shift is substantially larger for the bulk peak. This is consistent with the discrepancy in the fit of Sandercock and Wettling's [21] Fe data (fig. 2.13) to equations without exchange. It appears that the bulk peaks lie at a frequency slightly above the lower boundary of the bulk continuum (figs. 2.23 and 2.24), even at low k.

Although the above theoretical results are illuminating, they provide (at least to this writer) little intuitive understanding of the shapes of the Brillouin scattering peaks. The data indicate a rather abrupt low frequency shoulder for the volume peak and a very sharp surface peak for $k = k_y$; for $k = k_z$, the surviving volume peaks are broadened and more symmetric. Is it possible to understand these shapes intuitively?

Sandercock and Wettling [21] have given such an explanation based on simple mode dispersion arguments. The crucial ingredient is the realization that the limited penetration depth for light in metals ($\delta \sim 100$ Å) leads to a spread in possible k_x values for the bulk magnons. This spread, in turn, leads to a significant broadening of the bulk magnon peak in Brillouin scattering. The shape of the peak depends on θ_k in an intuitive way which agrees with the data.

The situation for $k = k_y$ ($\boldsymbol{H}$ perpendicular to the incident k_{light}) is indicated in fig. 2.27. The limited

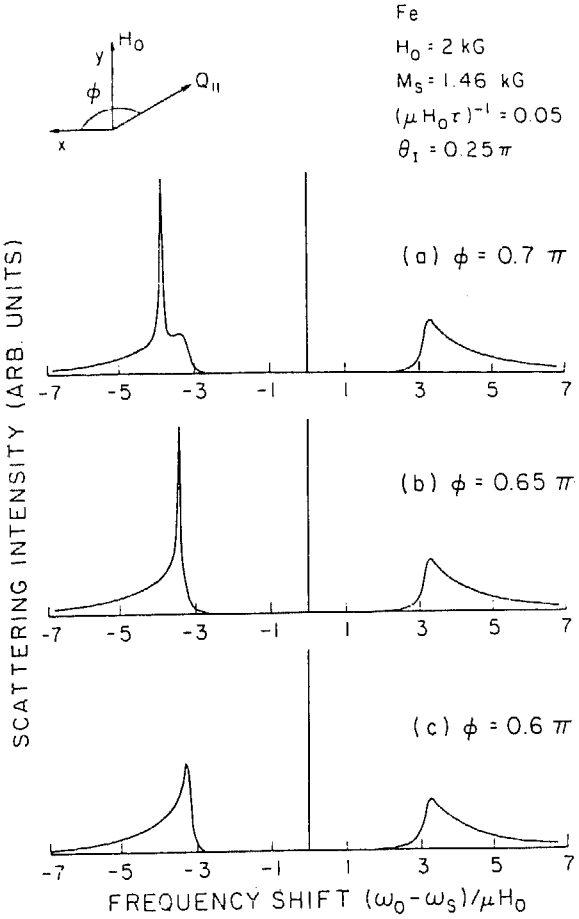

Fig. 2.26. Theoretical Brillouin spectra for Fe (after Camley and Mills [8]).

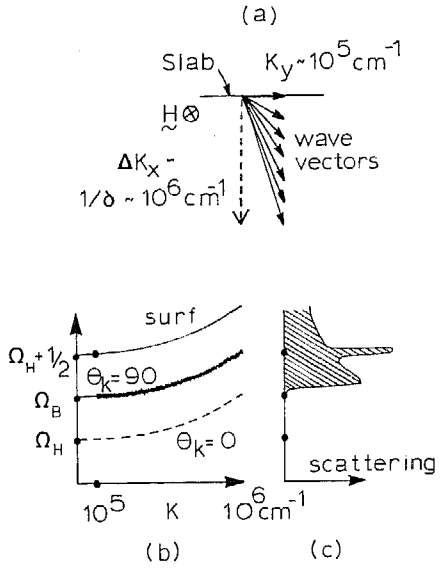

Fig. 2.27. Scattering in Fe for $k \perp H$.

light penetration depth implies, from the uncertainty principle, a spread in the x-components of $\boldsymbol{k}$ from zero to about $10^6\,\mathrm{cm}^{-1}$. All of the possible $\boldsymbol{k}$ vectors for scattering are perpendicular to $\boldsymbol{H}$ and constrained to the $\theta_k = \pi/2$ branch of the bulk manifold. The participation of those modes in the scattering is indicated by the heavy blacked-in line in fig. 2.27b extending from $k_y \sim 10^5\,\mathrm{cm}$ to $k \sim 10^6\,\mathrm{cm}^{-1}$ on the $\theta_k = 90°$ branch of the bulk manifold. The surface mode is observed only at $k_y = 10^5\,\mathrm{cm}^{-1}$. The bottom branch of the bulk manifold for $\theta_k = 0$ (not accessible in this configuration) is indicated by the dotted line. The qualitative shape of the Brillouin spectrum is sketched in fig. 2.27c, in which the standard display is rotated 90° to allow the frequency scale to match the spin-wave manifold. The spectral shape agrees qualitatively with the data.

Note, from fig. 2.27c, that the onset of scattering is expected to occur at a frequency just slightly above Ω_B (by about 7 MHz for Fe). In order for the bulk mode peak to be substantially shifted above Ω_B, as indicated by Camley and Mills, some selective process for strong scattering from moderate k magnons must be invoked. The data of Malozemoff et al. [24] in fig. 2.28 show that the theory fits the data for the bulk branch best for $k \sim 4 \times 10^5\,\mathrm{cm}^{-1}$. In order to qualitatively account for this shift, Malozemoff et al. [24] invoke a rudimentary but plausible pinning model.

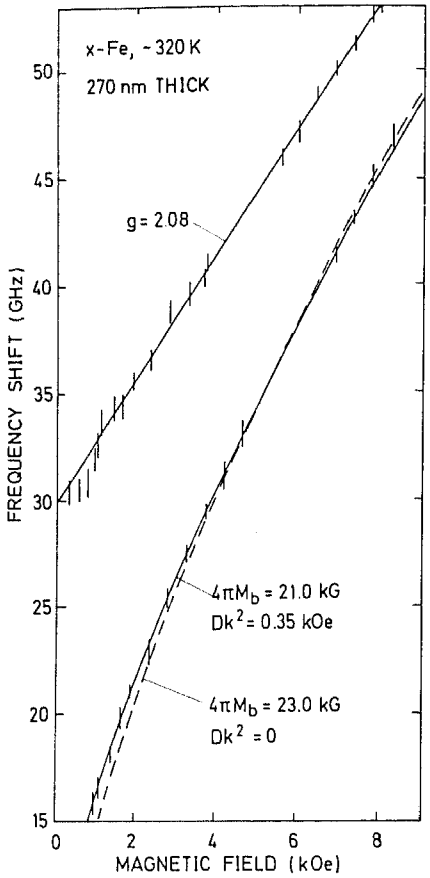

Fig. 2.28. Surface and volume magnon frequency vs. field for a sputtered Fe film (after Malozemoff et al. [24]).

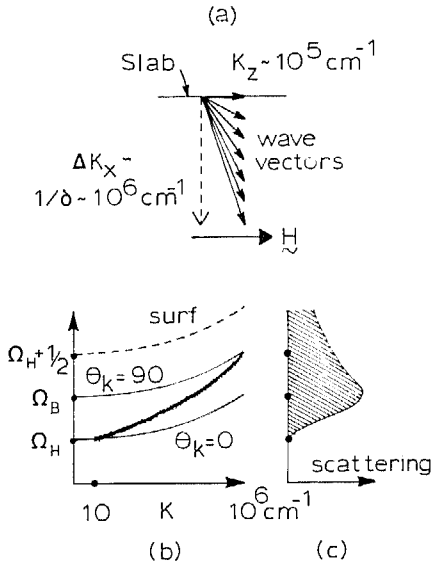

Fig. 2.29. Scattering in Fe for $k \parallel H$.

Turn now to the case where the in-plane wavevector is *not* perpendicular to H. Relative to the case just discussed, if k is rotated toward H, the surface peak moves down in frequency, broadens and merges with the bulk manifold, etc., as discussed above. For k parallel to H, we have the situation of fig. 2.29. The spread and distribution in k values are the same as before, except that θ_k varies from zero to $\pi/2$ as k rotates from in-plane (k_z) to perpendicular (k_x). The "trajectory" of the magnon frequency Ω_k relative to the bulk manifold at fixed field is shown in fig. 2.29b. This results in the broadened Brillouin scattering response of fig. 2.29c. Note that a surface excitation is not allowed for $\theta_k = 0$. This result qualitatively matches the data also for small $\theta_k < \theta_S$.

This explanation is appealing in that it depends only on the rather basic dispersion character. Quantitative density of states calculations based on the model could yield Brillouin scattering lineshape curves for use in evaluating data. The model also provides an easy explanation of the fact that other materials with either weak exchange, large light penetration depths, or both, do not evidence such line-broadening effects (see data on EuO by Grünberg and Metawe [19]). It is easy to see that the lines

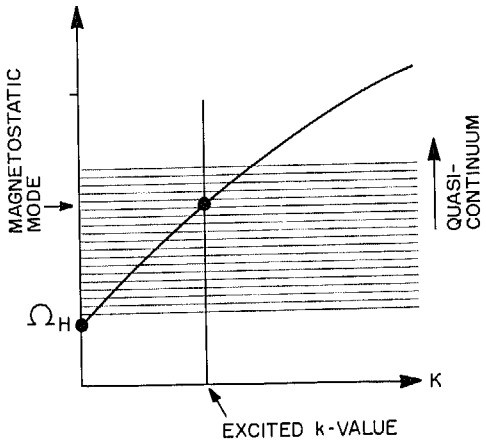

Fig. 2.30. Spin-wave dispersion at low k for $H\perp$ slab surface.

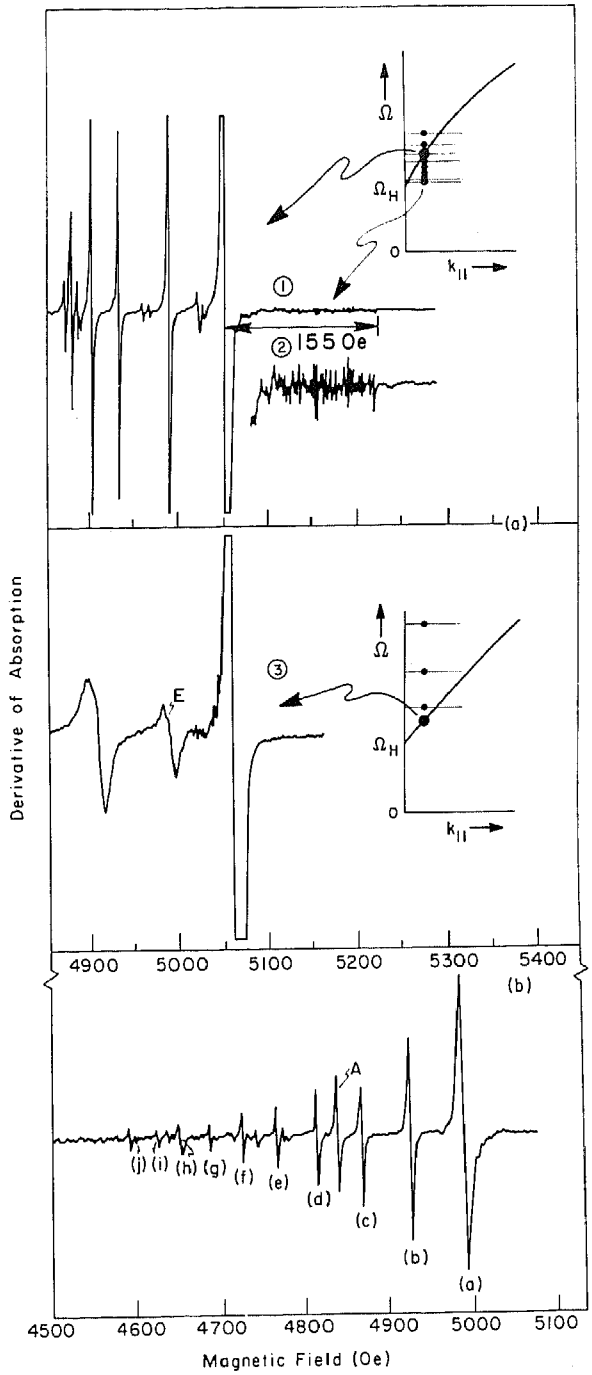

Fig. 2.31. FMR data for a thick YIG film, magnetized ⊥ to the surface (after Tittmann and DiWames [6]).

for $k \perp H$ will be extremely sharp if the branches in fig. 2.27 extend out horizontally (as would be the case for small exchange).

All of the results discussed so far are for in-plane magnetized slabs. In the perpendicular configuration one would also expect a condensation of the bulk (or volume) branches. The dispersion which results is sketched in fig. 2.30 for a "thick" slab, so that the exchange branches condense to a quasicontinuum of closely spaced (quadratic spacing) lines as schematically indicated. The lowest order "magnetostatic" branch threads these other branches, with all the effects discussed in section 2.3.

Figure 2.30 is deliberately limited to very low k, with no exchange curvature in evidence, in order to demonstrate a particular point. Consider the excitation of very low k modes at the indicated vertical line. The excited modes would consist of the quasicontinuum of states extending upward from $\Omega \sim \Omega_H$, decorated by a magnetostatic peak as indicated and possibly other resonances at higher Ω.

Precisely this experiment has been done by Tittmann and DeWames [6] for a thick (12.4 μ) YIG film by FMR at fixed frequency. Their data are shown in fig. 2.31. The field sweep yields the expected series of magnetostatic peaks and a complicated series of finely spaced resonances of low amplitude extending up in field from the last strong peak to an abrupt cut-off. This cut-off is interpreted as the point at which the bottom of the spin-wave manifold (at Ω_H for low k) passes above the excitation frequency.

3. Anisotropy, parametric excitations, and relaxation

The previous section surveyed magnetic excitations in isotropic ferromagnetic media. This section examines selective aspects of anisotropy as related to magnetic excitations, nonlinear (parametric) excitations, and relaxation. The four parts are specifically concerned with surface anisotropy, dispersion modifications due to crystalline anisotropy and nonferromagnetic exchange, nonlinear excitations, and relaxation.

3.1. Surface anisotropy and pinning

The effect of pinning on dipole-exchange dispersion was seen in section 2.3 to be important. In going from the usual antinode surface constraint on the dynamic component of $\boldsymbol{M}$,

$$\partial m/\partial x = 0 \tag{3.1}$$

to the "pinned" condition,

$$m = 0\,, \tag{3.2}$$

at the surfaces, significant modifications occur for the dispersion curves in both the parallel and the perpendicular configurations. Notably, one effect was the elimination of modes with pure surface character in the parallel case.

In this discussion, we begin with a consideration of partial pinning as it relates to the surface modes discussed in section 2, and then move on to consider more general aspects of surface anisotropy. Surface anisotropy, in itself, can give rise to excitations with surface character. These excitations are termed acoustic or Heisenberg surface waves, with frequencies below the bulk manifold. We close this section with a brief discussion of various sources of surface anisotropy.

The Camley and Mills [8] theory included a general surface condition, given below in the more conventional format:

$$\frac{\partial m}{n} + \frac{K_s}{A} m = 0 . \tag{3.3}$$

Here, n is an outward pointing surface normal, K_s is a surface anisotropy constant, and A is an exchange parameter related to D ($2A/M_0 = D$). Their numerical results indicated an upshift in frequency for the surface mode if K_s were increased from zero in a positive sense ($K_s > 0$), and a downshift for negative K_s. The discussion implies that positive K_s corresponds to an easy axis in the direction of $\boldsymbol{H}$ and $\boldsymbol{M}_0$. This is consistent with the classic Rado and Weertman [73] calculation of surface anisotropy. If one assumes a uni-axial surface anisotropy with an easy axis parallel to $\boldsymbol{M}_0$ (and $\boldsymbol{H}$ in our case), characterized by K_s (in erg/cm^3), the Rado and Weertman formalism leads precisely to eq. (3.3).

Camley and Mills also indicated that positive K_s causes the surface mode to broaden and that the broadening so induced increases with k (e.g., exchange). As they point out, this trend is consistent with the "leaky surface wave" idea for the semi-infinite slab. When K_s is decreased from zero (negative K_s), they report an initial narrowing followed by the expected broadening as K_s becomes large and negative.

The narrowing of the surface mode linewidth and its downshift in frequency may be related to the well known fact that a negative value of K_s leads, *in itself*, to imaginary values of k_x and, hence, to modes with surface character.

Consider the simple case of a finite film of thickness S, with surfaces at $x = \pm S/2$. The allowed values of k_x for a mode pattern,

$$m(x) \propto \exp(ik_x x) + \exp(-ik_x x) , \tag{3.4}$$

with the surface condition of eq. (3.3), are simply the k_x solutions to

$$k_x (A/K_s) \tan(k_x L/2) = 1 . \tag{3.5}$$

The behavior of these solutions as a function of K_s/A is indicated in fig. 3.1. Solid circles denote even volume modes. Half solid circles denote odd volume modes. Solid (half solid) squares denote even (odd) surface modes. Start at the upper extreme, for $K_s/A = +\infty$ (infinite, positive pinning). We obtain standing modes at $k_x = n\pi/S$ ($n = 1, 2, 3, \ldots$) which alternate from even symmetry ($n = 1, 3, \ldots$) to odd symmetry ($n = 2, 4, \ldots$) in the expected way for pinned spins. As K_s/A is reduced, the allowed k_x values shift down in k (and hence in frequency). At $K_s/A = 0$, the lowest order even mode has become a uniform mode, and the higher order modes sit at $k_x = n\pi/S$ with even symmetry for $n = 1, 3, \ldots$ and odd symmetry for $n = 2, 4, \ldots$. The mode shapes are sketched in the lower part of the figure.

The interesting result, in the present context, is for negative K_s/A. As K_s/A is initially decreased from zero, the lowest order mode develops surface character. Crudely speaking, the uniform ($k = 0$) character at $K_s = 0$ starts to show a droop in the middle of the film as K_s/A becomes negative, which develops into an even surface mode. Additionally, as K_s/A decreases from zero, the lowest order odd mode departs from its previous trajectory in the sketch and arrives at $k_x = 0$ for $K_s/A = -2/S$. A mode of odd symmetry at $k_x = 0$ is a null mode by definition. As K_s/A decreases further, this mode evolves into an odd surface mode. It is to be noted that these features follow directly from the surface constraint on m.

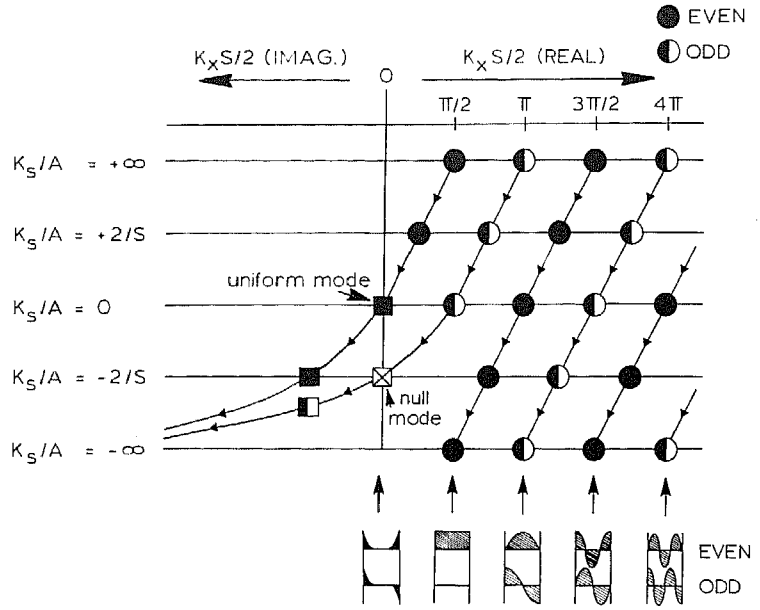

Fig. 3.1. Standing modes vs. K_s/A.

We see, therefore, that surface character, with decay from both sides of the slab, is a natural consequence of negative K_s in the in-plane uni-axial model. It is reasonable to speculate that such effects could influence the original nonreciprocal surface mode in a nontrivial manner. The behavior noted by Camley and Mills may be due to such influences.

There has been extensive work on surface anisotropy theory and the use of various models of the anisotropy to explain ferromagnetic resonance and spin-wave resonance data. A complete review would not be appropriate here. It is appropriate, however, to comment on several of the recent developments in this field concerning symmetry consistent surface anisotropy and high field surface mode observations.

The pure uni-axial surface anisotropy implicit in eq. (3.3) is not entirely satisfactory from the point of view of symmetry. One would expect that different restoring torques would be found for surface spin deviations in-plane and out-of-plane, relative to the direction of $\boldsymbol{M}_0$ along z. Pure uni-axial anisotropy yields equivalent torques. It is straightforward to apply the Rado–Weertman equations to various possible surface anisotropy equations and various field orientations relative to the surface of the slab to obtain constraints on $\boldsymbol{m}$ analogous to (but more complicated than) eq. (3.3).

A somewhat more unified approach has been developed by Puszkarski [3, 63, 74, 75], with a very readable summary by Yu et al. [76]. Puszkarski describes the pinning condition at a given surface in terms of a surface parameter A_p:

$$A_p = 1 - (g\mu_B/2SzJ)(\boldsymbol{\gamma} \cdot \boldsymbol{K}_s \cdot \boldsymbol{\gamma}) \tag{3.6}$$

where g, μ_B, S, z, and J represent the usual g-value, Bohr magneton, spin, number of nearest neighbors, and Heisenberg exchange parameter, respectively. $\boldsymbol{K}_s$ represents a surface anisotropy tensor and $\boldsymbol{\gamma}$ is a unit vector in the direction of $\boldsymbol{M}_0$. As discussed in the above references, the limiting case

$A_p = -\infty$ corresponds to complete pinning as for $K_s = +\infty$ in fig. 3.1. The value $A_p = 1$ corresponds to no pinning. For $A_p > 1$, surface modes are allowed (as for $K_s < 0$ in fig. 3.1). $A_p = +\infty$ corresponds to complete pinning and $K_s = -\infty$.

In the spirit of eq. (3.6), consider the form of the surface anisotropy consistent with symmetry. In reference to fig. 3.2, it is easy to see that conical symmetry is the most general possibility. Any orientation of $\boldsymbol{M}_0$ at an angle ϕ relative to the slab normal should correspond to the same anisotropy. Yu et al. [76] have written the anisotropy and the Puszkarski pinning parameter in terms of two anisotropy constants, $K_\perp$ and $K_\parallel$,

$$A_p = 1 - (g\mu_B/2SzJ)\,(K_\perp \cos^2\phi + K_\parallel \sin^2\phi)\,. \tag{3.7}$$

$K_\parallel$ alone corresponds to a perpendicular easy-axis for $K_\parallel > 0$ or an easy plane for $K_\parallel < 0$. $K_\perp$ alone corresponds to a perpendicular easy-axis for $K_\perp < 0$ or an easy plane for $K_\perp > 0$. Together, they yield the requisite conical symmetry. There is a nice parallel here with the uni-axial symmetry of hexagonal ferrites, which (in some cases) exhibit conical crystalline anisotropy.

In the above formulation, we note that if $K_\parallel$ and $K_\perp$ are of opposite sign, there exists a critical angle $\phi = \phi_c$ at which the pinning is effectively zero ($A_p = 1$),

$$\phi_c = \tan^{-1}(-K_\perp/K_\parallel)\,. \tag{3.8}$$

Given a critical angle ϕ_c, surface modes are allowed for $\phi > \phi_c$ if $K_\parallel$ is negative or for $\phi < \phi_c$ if $K_\parallel$ is positive. (Recall that surface modes are possible for $A_p > 1$, in the Puszkarski model.)

Surface modes have been detected in FMR experiments on single crystal YIG films (Brown et al. [77]; Henry et al. [78]; Yu et al. [76]) which have the general features expected from the above model. Sample data by Yu et al. [76] are shown in fig. 3.3 for a 3700 Å film at 9.2 GHz. For $\phi = 90°$, 60°, 55°, and 50°, the high field resonance was identified as a surface mode through various etching and annealing procedures. The lower mode for these same angles corresponds to the lowest order volume mode.

Decreasing the field angle ϕ from 90° causes the surface mode to shift and grow in intensity. The volume mode shifts and decreases in intensity. At $\phi = 40°$, the intensity of the surface mode is very large, its position is almost exactly that expected for the uniform mode, and the lowest order volume mode has disappeared.

These behaviors are consistent with the Puszkarski model, assuming $K_\parallel < 0$ and $K_\perp > 0$ at the film-substrate interface, no pinning at the other surface ($A_p = 1$), $\phi_c = 40°$, and the mode shapes sketched in fig. 3.1 (modified for asymmetric pinning).

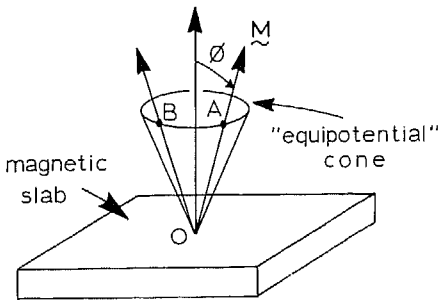

Fig. 3.2. "Equipotential" surface anisotropy cone for isotropic slab.

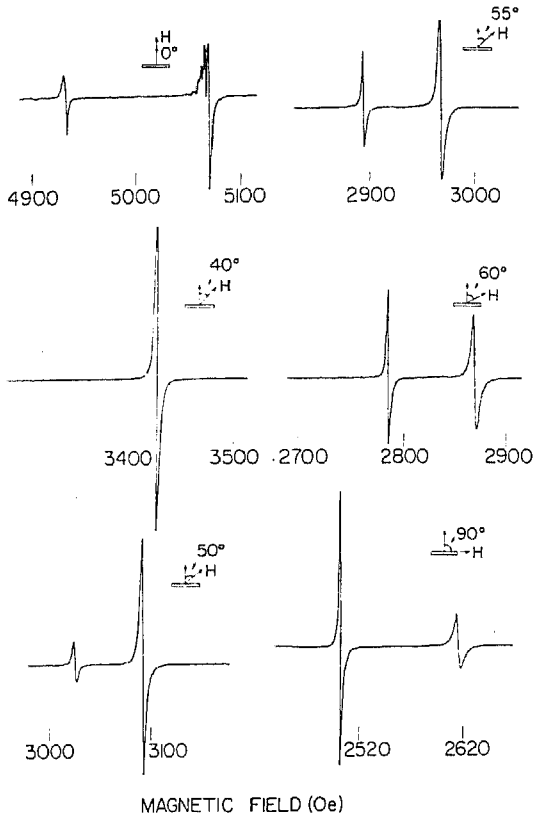

Fig. 3.3. Surface mode resonance in a YIG film; angle dependence (after Yu et al. [76]).

The shift of the surface mode (relative to the position of the uniform mode) as the pinning parameter decreases is due to the decrease in $|k_x|$. This decrease (k_x is imaginary) also causes the mode to become more uniform. At $\phi = \phi_c = 40°$, k_x is zero and the mode *is* the uniform mode. This increase in uniformity also results in a stronger resonance.

The behavior of the volume mode can be similarly explained. Strong pinning at one surface ($A_p > 1$) for parallel resonance makes this odd mode asymmetric and hence strongly excited. As K_s approaches zero ($A_p \to 1$), the pinning strength decreases and this mode becomes more symmetric. In the $A_p = 1$ limit at $\phi_c = 40°$, this mode has near perfect odd symmetry and does not couple to the uniform microwave field. Hence, its intensity vanishes.

For orientations $\phi < \phi_c$, we have $A < 1$ so that all allowed modes become volume modes ($K_s > 0$ in fig. 3.1). The nonzero pinning at one surface causes all of these modes to become asymmetric once again. Hence, they can be excited by the uniform microwave field.

It is to be recalled that the simple arguments in connection with fig. 3.1 showed that two surface modes are possible. We note that two surface modes at high field have also been detected by FMR in suitably prepared films (Yu et al. [76]), as indicated in fig. 3.4.

These high field surface modes differ conceptually from those of section 2. These modes, by their very nature, depend on the surface boundary conditions and are downshifted in frequency from the $k = 0$ resonances. These modes have been labeled as acoustic surface modes or Heisenberg surface modes by various authors as cited above. The discussion, limited to previous work, was for standing

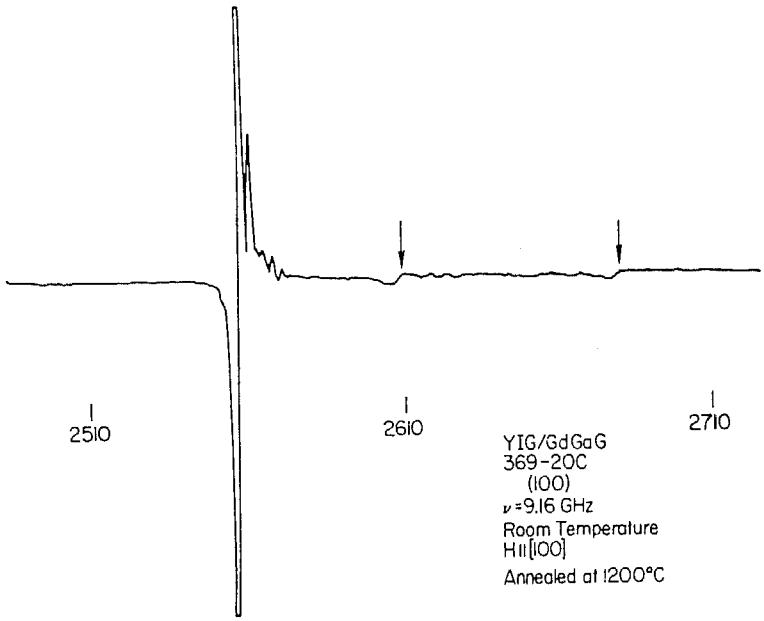

Fig. 3.4. FMR spectra for YIG film with two surface modes (after Yu et al. [76]).

modes ($k_y = k_z = 0$). The propagation characteristics of these modes do not appear to have received much attention.

While there have been no explicit studies of surface anisotropy by Brillouin scattering techniques, pinning has been invoked by various authors (as discussed in section 2) as a possible source of the discrepancy between data and theory. In addition to the use of pinning to account for small shifts in the Damon–Eshbach mode positions, as already considered, several authors (Camley and Mills [8]; Rahman and Mills [79]) have commented on the possibility of pinning effects with a strong temperature and field dependent character, due essentially to a phase transition connected with the surface spins.

This effect, termed "magnetic surface reconstruction" in several theoretical treatments (Trullinger and Mills [80]; Demangeat and Mills [81, 82]), is related to competing exchange forces on an atomic scale for the surface spins. The idea is that alternate surface spin configurations (relative to those in the bulk) may be more stable at low temperature. Specific proposals involve antiferromagnetic exchange and surface spin canting. It is argued that such surface reconstruction would be dominant at low temperature and zero field, and lead to strong pinning. An increase in temperature or field, however, would tend to destroy the "reconstructed" surface spin order. The pinning would therefore decrease.

Demangeat and Mills [82] have suggested that the strong temperature dependence of the pinning for EuS, inferred from FMR (Schwob et al. [83]), is due to such effects. Rahman and Mills [79] have suggested that the strong temperature dependence of the DE surface mode frequency in EuO (Grünberg and Metawe [19]) may be a surface reconstruction effect, as well. A conclusive connection between data and the theory has yet to be demonstrated.

Surface reconstruction effects of a somewhat crude level have, however, been observed in permalloy films for over a decade. Such effects were manifested in anomalous hysteresis and FMR behaviors at low temperature in the range of 4 to 100°K. The matter is reviewed by Bajorek and Wilts [84, 85]. All of these particular anomalies are related to a thin oxide layer. The surface layer, while complex (Pollak

and Bajorek [86]), appears to order antiferromagnetically at low temperature and give rise to magnetic behavior consistent with the well known exchange anisotropy between ferro- and antiferromagnetic phases (Meiklejohn and Bean [87, 88]).

3.2. Dispersion modifications

In the discussion so far, only isotropic ferromagnetic media have been considered, with a bulk dispersion as given by eq. (2.1). However, magnetic systems possess a variety of properties which can result in substantial modifications to the dispersion character and frequencies of magnetic excitations. These include crystalline anisotropy, anisotropic symmetric exchange (in noncubic systems), two sublattice effects in ferrimagnets (formally related to antiferromagnetic resonance), and antisymmetric exchange in weak ferromagnets. Most of these subjects are textbook topics. The common feature of relevance to this discussion is the rather high frequency of the magnetic excitations (tens of GHz to hundreds of GHz) and their potential accessibility through light scattering methods. In the remarks below, we touch briefly on these modifications and their study by various techniques.

Crystalline anisotropy alone is one source of additional effective fields in ferromagnetic media. These fields also serve to shift the magnetic excitation frequencies and, in some cases, complicate the k-dependence. We consider two simple situations, cubic anisotropy in YIG and easy plane anisotropy in hexagonal ferrites, to demonstrate the relevant effects on dispersion.

For cubic crystals, the free energy associated with the magnetocrystalline anisotropy is written as

$$F_A = K_1(\alpha_1^2\alpha_2^2 + \alpha_3^2 + \alpha_3^2\alpha_1^2) + \cdots \tag{3.9}$$

where K_1 is the first order anisotropy constant and the α_i are direction cosines relative to the crystallographic axes. For purposes of this discussion, second order terms are not considered. The above energy term can be included in spin-wave theory as shown by several authors and reviewed recently by Patton [89]. The essential result is that the dispersion of eq. (2.1) and fig. 2.2 is modified by the presence of anisotropy. For YIG, K_1 is negative, the effective anisotropy field, $H_A = 2|K_1|/M_0$, is about 90 Oe, and [111] is the easy direction. The biggest effect of anisotropy on dispersion is for [110] magnetized YIG. These effects are graphically demonstrated in fig. 3.5. The coordinate system of fig. 2.1 applies, with the x-axis along $[00\bar{1}]$, the y-axis along $[\bar{1}10]$, and the z-axis along [110]. For this particular case, we see that the various branch curves (fixed θ_k) have become branch *surfaces*. For $\theta_k \neq 0$, the spin-wave frequency ω_k is a function of the azimuthal spin-wave angle ϕ_k as well as k and θ_k. The upper branch surface ($\theta_k = \pi/2$) is decorated to emphasize this dependence on ϕ_k; the surface appears as warped. The amount of the warp is about 50 Oe (in field units).

The details of the anisotropic bulk manifold will, of course, depend on the orientation of $\boldsymbol{M}_0$, the values of K_1 (and perhaps K_2), and other material parameters (γ, M_0, D). The analytic expressions for the general dispersion function and the $k = 0$ intercepts in fig. 3.5, analogous to ω_H and ω_B in the isotropic case, are too cumbersome to present here. It should be clear, however, that dispersion can be anisotropic. This observation will become increasingly apparent as we consider hexagonal, easy plane systems. In section 3.4, the relaxation properties of magnetic excitations will be seen to be very sensitive to the anisotropic dispersion in certain instances.

Hexagonal ferrites exhibit a variety of complex anisotropy features, ranging from uni-axial to conical to easy-plane, depending on the particular composition and temperature. The complex structural variations and magnetic properties are discussed by Smit and Wijn [90], Von Aulock [91].

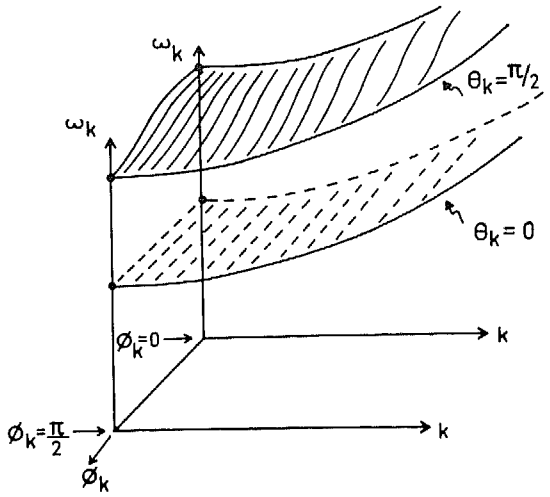

Fig. 3.5. Schematic representation of the spin-wave dispersion for [110] magnetized YIG.

Of particular interest here is the large class of planar hexaferrites. The high anisotropy material Co_2Y ("Y" denotes a particular structure class) has a planar anisotropy field $H_A \simeq 28$ kOe and a saturation induction $4\pi M_0 \simeq 2400$ G at 300°K. This large planar anisotropy effectively constrains the magnetization vector $\boldsymbol{M}$ (and hence the precession) to lie in the easy plane. The precession cone, therefore, is highly elliptical. These effects are schematically indicated in fig. 3.6, with the spin-precession cone essentially "squashed" in the easy basal plane.

If the hard c-axis is taken as the y-direction in the reference frame of fig. 3.6, with $\boldsymbol{H}$ along the z-axis, the spin-wave dispersion is (Schlömann et al. [92]):

$$(\omega_k/\gamma)^2 = (H + Dk^2)\,(H + Dk^2 + 4\Pi M_0 \sin^2\theta_k) + H_A(H + Dk^2 + 4\Pi M_0 \sin^2\theta_k \cos^2\phi_k)\,. \tag{3.10}$$

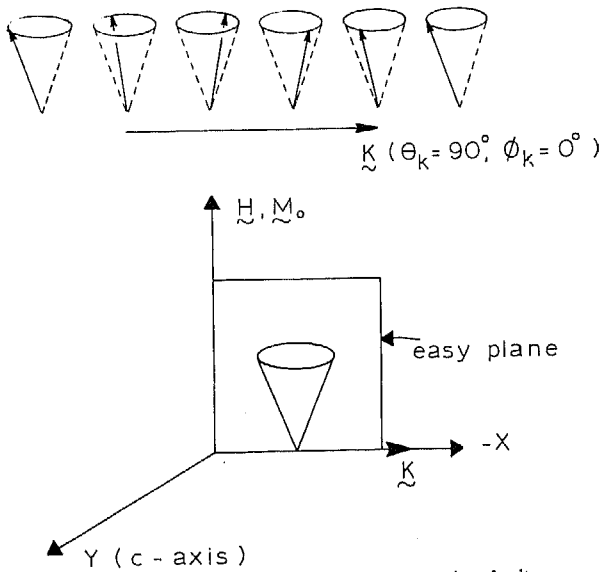

Fig. 3.6. Elliptical spin-wave precession for planar hexaferrite.

The first term on the right-hand side is the same as for an isotropic medium. Anisotropy modifications are in the second term. Recall that H_A is large. Planar hexaferrites can also have basal plane anisotropy which is usually small compared to H_A and is neglected here. Strictly speaking, the Dk^2 exchange term should be expressed as $D(k_x^2 + k_z^2) + D'(k_y^2)$, since the c-axis ($y$-direction) is not equivalent to the a- and b-axes (Mita and Shimizu [93, 94]). The general shape of the dispersion is sketched in fig. 3.7. The anisotropic effects are clearly evident. For Co_2Y, the "gap" at $k = 0$ for the $\theta_k = \Pi/2$ branch surface is about 10 GHz for $H = 2$ kOe. The gap at $k = 0$ for $\phi_k = 90°$ is only 1 GHz. The large upshift for the ($\theta_k = 90°$, $\phi_k = 0°$) branch curve, blacked-in in fig. 3.7, is due to the large in-plane anisotropy.

The above two examples illustrate the effect of crystalline anisotropy on the magnetic excitation spectrum of bulk ferromagnetic media. It is well known that many classes of magnetic materials which possess a net magnetization are not, strictly speaking, ferromagnetic. These include two important types of systems of relevance here, ferrimagnets (such as the spinel ferrites and magnetic garnets) and weak ferromagnets (sometimes called parasitic ferromagnets or canted antiferromagnets). In closing this subsection, we consider those properties of magnetic excitations peculiar to these types of multiple sublattice magnetic order.

The general problem of ferrimagnetic resonance was discussed extensively in the early 1950's by Wangsness [95, 96, 97, 98] and Kaplan and Kittel [99], among others. The essential result is the occurrence of more than one resonance frequency. The low frequency resonance is the usual uniform mode resonance expressed by the Kittel condition, but with γ replaced by an effective gyromagnetic ratio γ_{eff} given by (in the two sublattice theory)

$$\gamma_{eff} = (M_A - M_B)/(M_A/\gamma_A - M_B/\gamma_B)\,. \tag{3.11}$$

M_A and M_B are the magnetizations and γ_A and γ_B are the gyromagnetic ratios for the two separate sublattices. The net magnetization for the system of two antiparallel sublattices is just $(M_A - M_B)$. We see that the behavior of γ_{eff} can be quite complicated in the vicinity of compensation points for M ($M_A = M_B$) and for angular momentum ($M_A/\gamma_A = M_B/\gamma_B$).

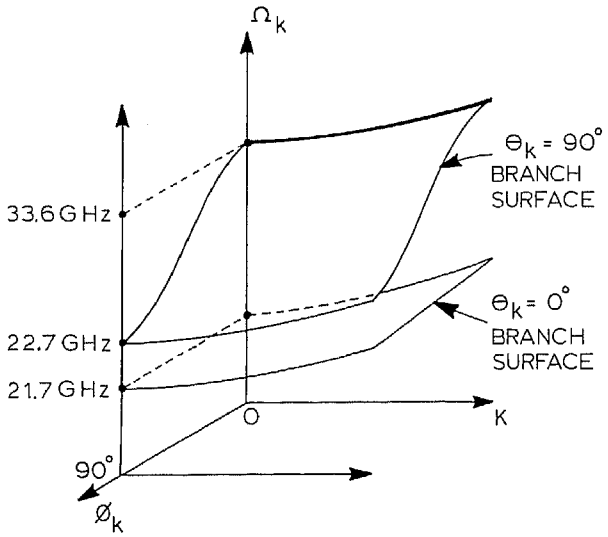

Fig. 3.7. Anisotropic spin-wave dispersion for planar hexaferrite (schematic).

In addition to the Kittel mode, an exchange resonance was also predicted,

$$\omega_e = 2(\gamma_A \gamma_B / \gamma_{eff}) H_E , \tag{3.12}$$

with $H_E = \frac{1}{2}\lambda_{AB}(M_A - M_B)$ an effective exchange field (λ_{AB} is the usual Weiss molecular field constant between the A and B sublattices). Due to the large exchange fields involved ($\sim 10^6$ Oe), the exchange resonance frequencies generally lie in the infrared or optical range. This exchange resonance is closely related to high frequency modes encountered in antiferromagnetic resonance.

It is clear from the above rudimentary equations that interesting effects can occur near compensation points. One expects increases in γ_{eff} and large reductions in the exchange resonance frequency ω_e. Such effects have been observed in Li-Cr ferrite (van Wieringen [100]; McGuire [101]), gadolinium iron garnet (Geschwind and Walker [102]), and europium iron garnet with gallium (LeGraw et al. [103]). The result for Li-Cr ferrite is shown in fig. 3.8. We see that both resonances are observable in the vicinity of the compensation point. Data were obtained (McGuire [101]) at 22.5 GHz. The resonances were rather broad, on the order of kOe.

Light scattering studies of the low frequency magnon mode in ferrimagnetic systems fall in the category discussed in section 2.1. Optical magnons have been investigated in a variety of ferrimagnetic systems, as well as a multitude of antiferromagnets, by Raman scattering techniques (because of the high frequencies involved under normal conditions). The literature is extensive, with representative papers in the proceedings for the first, second, and third conferences on light scattering in solids (Wright [104]; Balkanski [105]; Balkanski et al. [106]).

A distinct class of nonferromagnetic, net moment systems remain to be considered. These are the "weak ferromagnets" with (in the two sublattice approximation) two equal sublattice moments ($M_A = M_B$) oriented antiparallel except for a small canting. The magnetic structure, sublattice moments, and net moment are indicated schematically in fig. 3.9. The discussion below focuses on $FeBO_3$, one member of a group of rhombohedral "easy-plane" canted antiferromagnets which includes α-Fe_2O_3, $CoCO_3$, and $MnCO_3$. We conclude the discussion with brief comments on a second group of canted

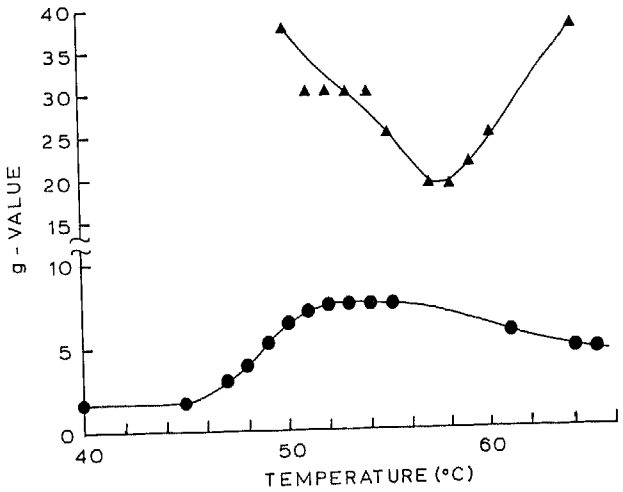

Fig. 3.8. Effective g-values in Li-Cr ferrite near the compensation point (adapted from McGuire [101]).

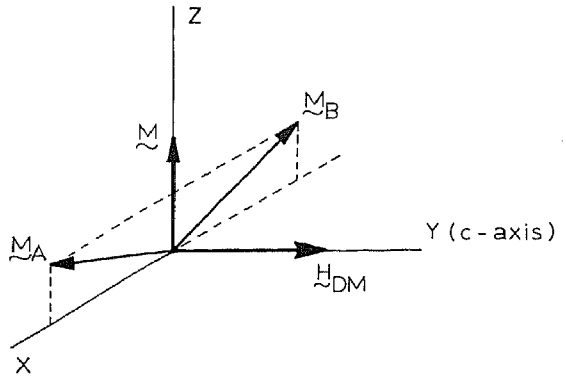

Fig. 3.9. Spin configuration for a canted antiferromagnet, such as $FeBO_3$.

antiferromagnets, comprised of yttrium and the rare-earth orthoferrites, orthochromites, and several manganese fluoride salts.

The canting in $FeBO_3$ is attributed to antisymmetric exchange with a free energy of the form

$$\boldsymbol{H}_{DM} \cdot (\boldsymbol{M}_A \times \boldsymbol{M}_B), \tag{3.13}$$

as proposed by Dzyaloshinski [107] and Moriya [108]. The effective exchange field H_{DM} is on the order of 60 kOe at room temperature. With $\boldsymbol{H}_{DM}$ in the y-direction (along the c-axis) as in fig. 3.9, the canting is about 0.7° with a net induction ($4\pi M_0$) of 120 G, effectively constrained to the x–z plane. Anisotropy in the basal plane appears to be negligible. Representative papers on the crystallographic and magnetic properties include Bernal et al. [109], Joubert et al. [110], Kurtzig et al. [111], LeCraw et al. [112, 113], Wolfe et al. [114], Kurtzig [115], Seavey [116], and Schober [117].

From the above properties, it is clear that $FeBO_3$ is an easy-plane weak ferromagnet in which the planar character (as well as M_0 itself) derive from a Dzyaloshinski–Moriya antisymmetric exchange field, in contrast to the anisotropy origin of the planar properties for Co_2Y. Since the exchange field H_{DM} is larger and $4\pi M_0$ smaller, we anticipate that the dispersion is even more anisotropic than for planar hexaferrites. This is indeed the case, along with a number of additional differences. The qualitative features of the $FeBO_3$ low frequency magnon dispersion at zero field ($H = 0$) are shown in fig. 3.10, based upon the Brillouin scattering studies of Jantz et al. [26], and Jantz and Wettling [27, 28], as well as theoretical considerations by Ozhogin [118]. In addition to the anticipated easy-plane character, several new features are apparent.

First, note the different behavior of the exchange branches at the two opposite sides of the $\theta_k = 90°$ surface. The branch at $\phi_k = 90°$ corresponds to $\boldsymbol{k}$ parallel to the c-axis. It is apparent that the exchange term for this branch ($D_\parallel k^2$) grows more rapidly with k than the other two branches shown (for which $\boldsymbol{k}$ is perpendicular to the c-axis). A careful analysis by Jantz et al. [26] shows that the rhombohedral structure results in a direction-dependent (relative to the c-axis) exchange, with $D_\parallel/D_\perp \simeq 1.6$. This allows the parallel branch to overtake the perpendicular branch at about $k \simeq 10^5\ \mathrm{cm}^{-1}$. At this k-value, ω_k is independent of ϕ_k for $\theta_k = 90°$.

Second, we note a gap frequency of about 2.5 GHz (about 900 Oe in field units) for $H = 0$. (FMR and light scattering yield 3 and 1.5 GHz, respectively. The 2.5 GHz value in fig. 3.10 is intended only as an indication of the magnitude of the gap.) Because of the negligible basal plane anisotropy for $FeBO_3$, this

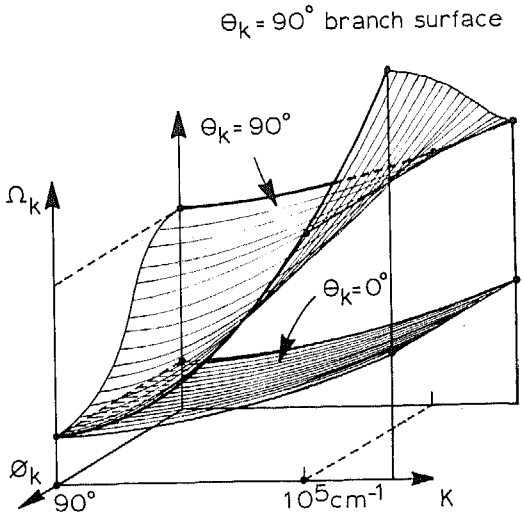

Fig. 3.10. Magnon dispersion in $FeBO_3$ at $H = 0$.

gap is generally attributed to magneto-elastic interactions. A quantitative explanation, however, remains elusive.

The $k = 0$ acoustic spin-wave frequency is specified by (Ozhogin [118])

$$(\omega_{k=0}/\gamma)^2 = H(H + H_{DM}) + \frac{4\Pi M_0}{H_{DM}}(H + H_{DM})^2 \sin^2\theta_k \cos^2\phi_k + (\omega_\Delta/\gamma)^2 . \tag{3.14}$$

Ozhogin [118] has also done the analysis to calculate the general dispersion for both acoustic and optical spin waves (the acoustic manifold is shown in fig. 3.10). The expressions (and the mathematics) are tedious, and it appears that equivalent dispersion equations can be obtained from carefully constructed stiffness arguments. Notable in eq. (3.10) are the high frequencies which are possible (for the acoustic spin waves) at moderate fields; tens of kOe yield a hundred GHz or higher. Wettling et al. [32] have recently succeeded in measuring both the thermal $k = 0$ magnon and the thermal optical magnon in $FeBO_3$. Zero wavevector magnons excited during ferromagnetic resonance have been observed by Borovik-Romanov et al. [119].

The second group of canted antiferromagnets is comprised mostly of the orthoferrites and related compounds. At room temperature these materials have the magnetic structure indicated in fig. 3.9 with $\boldsymbol{M}_A$ and $\boldsymbol{M}_B$ nearly parallel to the x-axis (crystallographic a-axis) with canting in the x–z plane and a net moment in the z-direction (c-axis for the orthoferrites). Anisotropy fields on the order of kOe make the a-axis an easy direction for the sublattice moments. Canting in the x–z plane to yield the net z-moment is induced by a combination of antisymmetric exchange (H_{DM}) and single-ion anisotropy terms with antisymmetric exchange usually dominant. For these materials, then, the x–z plane is not an easy plane. The net spontaneous moment is parallel to the z-direction (c-axis).

The low temperature behavior of the orthoferrites is nicely summarized in graphical form, as shown in fig. 3.11 (after White [102]). We see that four orthoferrites, $YFeO_3$, $LuFeO_3$, $EuFeO_3$, and $LaFeO_3$ keep the order described above down to low temperature. (The notation $\Gamma_4(F_z)$ indicates this structure, in the two sublattice approximation.) The remainder exhibit spin reorientation (M_A and M_B flip to the

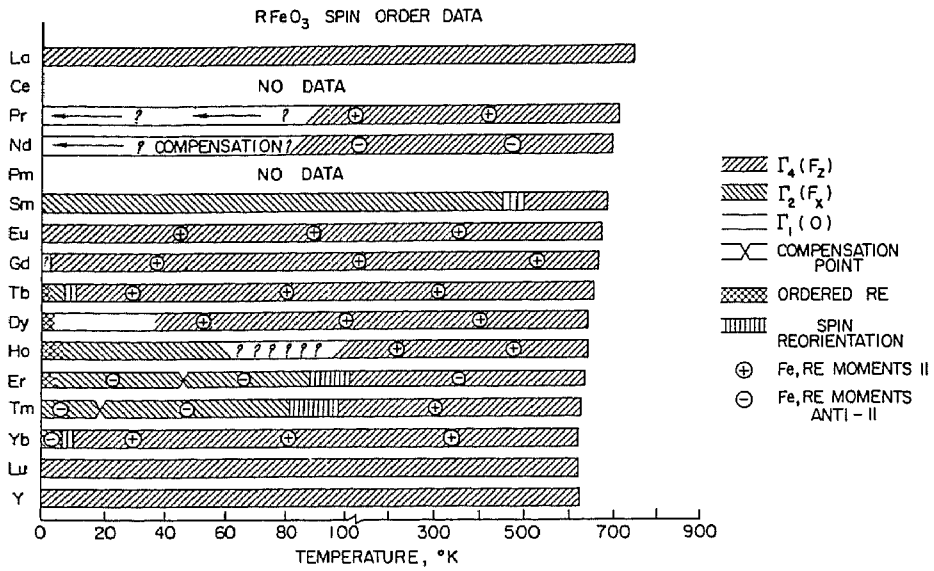

Fig. 3.11. Summary of orthoferrite properties as a function of temperature (after White [120]).

z-axis, with $\boldsymbol{M}_0$ along the x-axis, $\Gamma_2(F_x)$), compensation points, and other complex behavior. Both categories exhibit basic properties that are easily accessed by both FMR and light scattering techniques.

The prototype "simple" orthoferrite, $YFeO_3$, with an easy direction along the z-axis, was probably the first bubble material (see fig. 8 in Sherwood et al. [1959]). It has received renewed attention recently because of its relatively low resonance frequencies (for orthoferrites) of 330 GHz and 519 GHz for the acoustic and optical $k = 0$ magnon, respectively (White et al. [122, 123, 124]). To a good approximation, these resonance frequencies are given by (Hermann [125])

$$(\omega_0/\gamma)^2 = 2H_E H_{K'} + H(H + H_{DM}), \tag{3.15a}$$

$$(\omega_e/\gamma)^2 = 2H_E(H_K + H_{K'}) + H_{DM}(H + H_{DM}), \tag{3.15b}$$

for a field H along the z-axis. From the above frequency determinations and other data (Jacobs et al. [126]), one may estimate the various interaction fields as follows:

H_E (symmetric exchange) ~ 6400 kOe,

H_{DM} (antisymmetric exchange) ~ 140 kOe,

H_K (x–z easy plane anisotropy) ~ 3 kOe,

$H_{K'}$ (easy z-axis anisotropy for $\boldsymbol{M}_A$ and $\boldsymbol{M}_B$) ~ 1.2 kOe.

We see from eqs. (3.15a,b) that the mode frequencies are determined by an effective field which is the geometric mean of the exchange field H_E and some anisotropy field. In effect, H_E serves as an amplification factor for the relatively small anisotropy fields to yield high frequencies. It has been proposed recently (White and Patton [127]) to utilize magneto-elastic interactions to tune the low

frequency mode. Estimates of the possible tuning due to the application of uni-axial stress are on the order of MHz/bar.

Microwave resonance in the second group of rare earth orthoferrites near their reorientation temperatures has been a subject of intense study, both theoretically (Hermann [125, 128]; Hagedorn and Gyorgy [129]; Shane [130]) and experimentally (Hagedorn et al. [131]; LeCraw et al. [132]). The reorientation region is of interest because of the large drop in the acoustic mode frequency. The "softening" of the anisotropy at reorientation pushes the frequencies down into the accessible microwave range.

The results of the experimental studies were peculiar, with resonance positions (in field) independent of frequency over tens of GHz, and complex spectra which were sensitive to very small changes in the applied field direction. The comprehensive analysis of Hagedorn and Gyorgy [129], which included two- and three-fold anisotropy, arbitrary field direction in the x–z plane, and phenomenological damping, appears to explain the available data.

Noteworthy in the analysis of Hagedorn and Gyorgy [129], as well as that of Cinader [133] and Ozhogin et al. [134], is the effect of a field applied perpendicular to the weak moment and parallel to the antiferromagnetic easy axis. Theoretical curves for $TmFeO_3$ at 81°K (just below the reorientation region, so the weak moment is along the x-axis, with sublattice spins parallel to the z-axis in zero field) for the low frequency branch frequency vs. field are shown in fig. 3.12. With the field aligned exactly along the z-axis (0° curve), the resonance tunes down as the field is increased. As the field strength crosses the value required to rotate the weak moment into the field direction, we have a soft mode situation and $\omega_{res} = 0$.

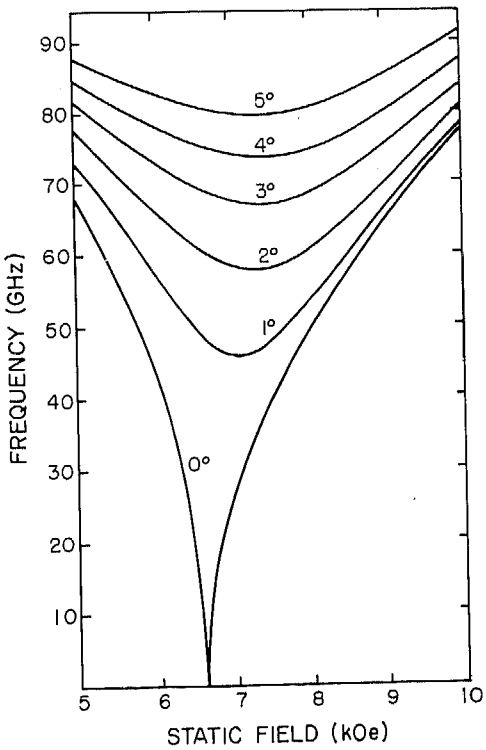

Fig. 3.12. Resonance frequency vs. field for $TmFeO_3$ at 81°K, just below the reorientation temperature region (after Hagedorn et al. [131]).

This cusp-like behavior is qualitatively similar to that for FMR with the field along a hard direction in uni-axial materials, etc. The full-rotation field in fig. 3.12 is about 6.6 kOe, a relatively low value, because the anisotropy is reduced near reorientation. The fields required to align the weak moment in the hard direction at room temperature are generally much larger; they are about 20 kOe for $SmFeO_3$ (Cinader [133]) and 70 kOe for $YFeO_3$ (Jacobs et al. [126]; Ozhonin et al. [134]).

The other curves in fig. 3.12 are for small deviations in field direction from the hard axis in the x–z plane. We see that very small deviations, as low as a fraction of a degree, serve to effectively wipe out the sharp cusp behavior. Deviations of a few degrees are sufficient to shift the mode frequencies above the easily accessible microwave frequencies of a few tens of GHz. Such orientation effects have been invoked to explain many of the complex microwave results noted above. Ozhogin et al. [134] were able to actually measure the cusp wipe-out effect in $YFeO_3$ and $SmFeO_3$ at 128 GHz.

The magnon frequencies involved in orthoferrites ranged from tens to hundreds of GHz, and hence straddle the accessible regions for Brillouin scattering (up to about 100 GHz) and Raman scattering (usually above a few hundred GHz). White et al. [122, 123, 124] and Koshizuka et al. [135] have used inelastic light scattering to study the magnon frequency behavior in the spin reorientation temperature regime for various orthoferrites.

3.3. *Nonlinear excitations*

The emphasis of this section is on the parametric excitation of spin waves in magnetic systems, often termed "spin-wave instability". Work in this area dates back to the original observation of ferromagnetic resonance saturation for power levels well below those at which the small signal, linear response models should break down (Damon [136]; Bloembergen and Wang [137]). Explanations of these and other nonlinear effects were provided by Suhl [138], Morgenthaler [139], and Schlömann et al. [140]. Reviews of the literature on spin-wave instability effects are provided by Sparks [43] and Patton [141, 89, 142].

There has been a revival of interest in nonlinear phenomena in recent years with the discovery of "fine structure" by Jantz and coworkers (Jantz and Schneider [143, 144]). The details will be elaborated upon in the discussion to follow, but the basic effect is shown in fig. 3.13. The figure shows microwave absorption vs. static field for transverse pumping at a moderate power level sufficient to excite unstable

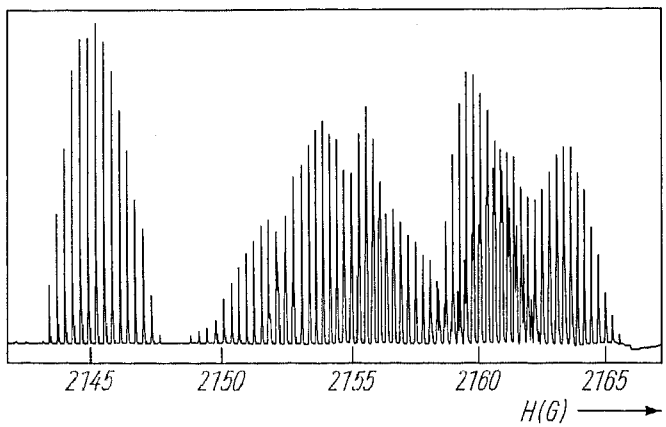

Fig. 3.13. Fine structure peaks for subsidiary absorption in single crystal YIG (after Jantz and Schneider [144]).

spin waves. The spectra consists of a multitude of very narrow instability spikes 5–10 mOe in width. Each spike corresponds to the excitation of one discrete standing spin-wave mode. The use of such fine structure to study the properties of spin-wave excitations is detailed in the above references.

The easiest and most intuitive approach to spin-wave instability phenomena involves a consideration of parallel pumping, in which a microwave magnetic field at frequency ω is applied parallel to the state field. For spin waves with $\theta_k \neq 0$, the precession cones are elliptical. This leads to a "wobble" in the z-component of $\boldsymbol{M}$ at $2\omega_k$ which can couple to (and be driven by) the parallel pumping field. As the pump power input is gradually increased, a critical point is reached at which the power input exceeds the magnon relaxation rate. At this point, spin-wave instability occurs and the magnon occupation number is pumped above the thermal value. Experimentally, this shows up as an abrupt increase in microwave power absorption. The microwave field amplitude at which this abrupt "break" in absorbed power occurs is termed h_{crit}.

The isotropic medium theory yields a threshold field amplitude h_c, for the potential instability of a general $(k, \theta_k, \omega_k = \omega/2)$ spin-wave,

$$h_c = (\Omega/\sin^2 \theta_k)\, \Delta H_k\,, \tag{3.16}$$

where ΔH_k is the relaxation rate of the magnon in linewidth units. ΔH_k is generally termed the "spin-wave linewidth". The *observed* threshold (h_{crit}) in a typical experiment is the microwave field amplitude corresponding to the lowest possible value of h_c under the dispersion constraints. Elaboration follows below.

From eq. (3.16), the lowest h_c (h_{crit}) corresponds to the largest possible θ_k. We denote that (k, θ_k) mode with the lowest threshold as $(k^{(\text{crit})}, \theta_k^{(\text{crit})})$. Recall the frequency constraint, $\omega_k = \omega/2$. The position of the spin-wave manifold, relative to ω_k, determines the available k and θ_k values. The situation is indicated in fig. 3.14. At low field (left-hand diagram), the manifold at $k = 0$ is well below $\omega_k = \omega/2$, all θ_k modes are available and the lowest threshold is for $\theta_k^{(\text{crit})} = 90°$ and $k^{(\text{crit})}$ as indicated. As the field is increased, the manifold shifts up, $\theta_k^{(\text{crit})}$ stays at 90° and $k^{(\text{crit})}$ decreases. This situation continues until H exceeds H_{90}. At this field the upper branch at $k = 0$ crosses $\omega/2$. For $H > H_{90}$, the maximum θ_k is less than 90°. When the field exceeds H_0, no modes are degenerate with $\omega_k = \omega/2$. The resulting variation in $k^{(\text{crit})}$ and $\theta_k^{(\text{crit})}$ with field is indicated in the bottom part of the figure.

We can see from eq. (3.16) and the graphs in fig. 3.14 that the k-dependence of the spin-wave linewidth will determine the general shape of the observed (or predicted) h_{crit} vs. H curve. Consider the schematic curves in fig. 3.15. Noting that $\theta_k^{(\text{crit})} = 90°$ is satisfied for $H < H_{90}$, the flat curve (curve A) would imply that ΔH_k is independent of k. An increasing curve (curve B) would indicate that ΔH_k is an increasing function of k. Representative x-band data for [111] magnetized YIG are shown in fig. 3.16. For a large variety of ferrite materials (and metals as well, in the limited cases reported), ΔH_k appears to have a k-dependence as indicated by curve B in fig. 3.15 and the data of fig. 3.16. Anisotropic (k dependent relaxation) will be considered further in section 3.4. The characteristic shape of these data have led to the label "butterfly curve", even in other cases where (as we shall see) the shapes are quite different.

Similar considerations apply to transverse pumping, with the microwave field perpendicular to the static field. The details of the coupling between the microwave field and the spin waves involve the uniform precession as an intermediary. For isotropic media, the threshold field expression is, to a good approximation,

$$h_c \approx \alpha_0^{-1}(\Omega/\sin \theta_k \cos \theta_k)\, \Delta H_k\,, \tag{3.17}$$

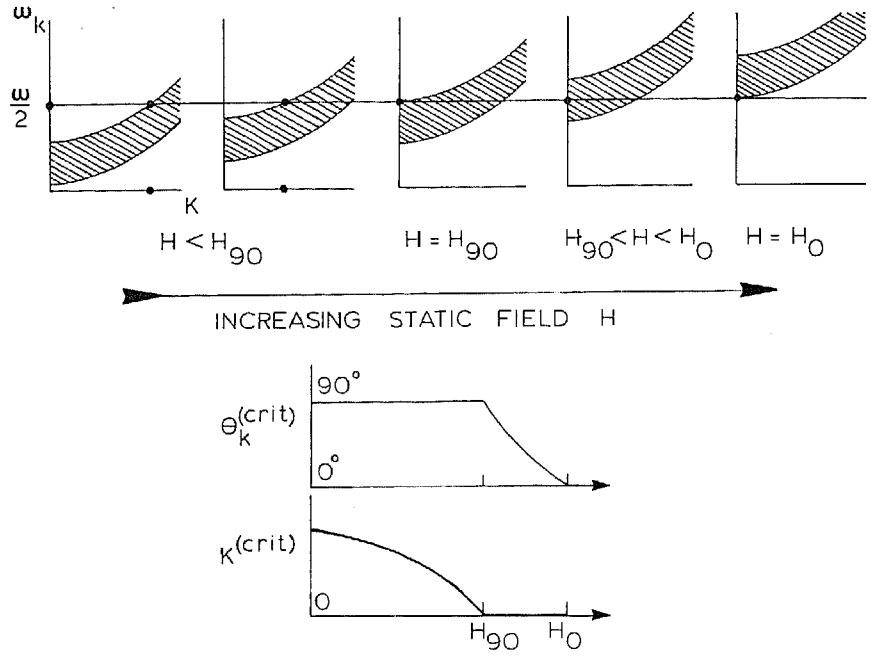

Fig. 3.14. Mode conditions for parallel pumping.

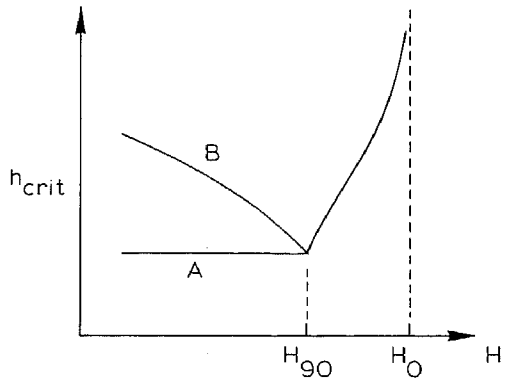

Fig. 3.15. Schematic parallel pump butterfly curves (h_{crit} vs. H).

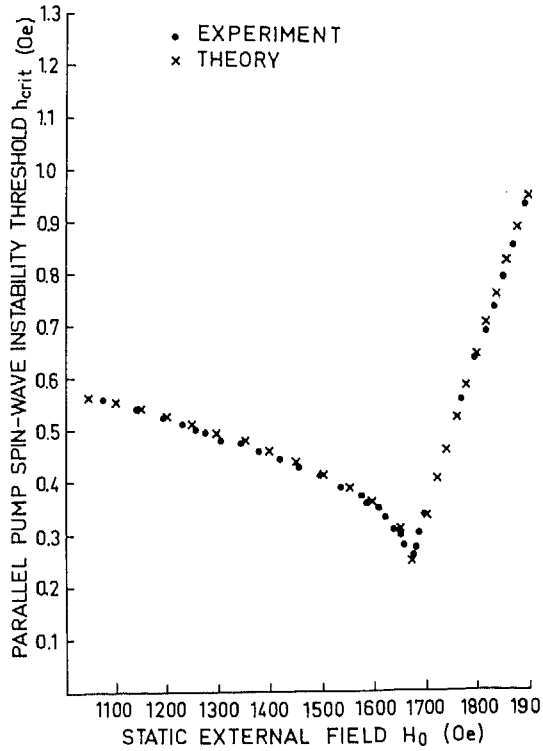

Fig. 3.16. Parallel pump butterfly curve data for [111] magnetized YIG (after Yakovlev et al. [145]).

where α_0 indicates the uniform precession (FMR) amplitude. We can see that the θ_k dependence in eq. (3.17) will tend to select out $\theta_k \sim 45°$ spin waves for instability. Since H_{45} (the field for $k = 0$ spin waves at $\theta_k = 45°$ and $\omega_k = \omega/2$) is above H_{90}, the minimum of the "butterfly curve" will occur at higher static field for transverse pumping than for parallel pumping. Noting that α_0 will increase with field (as the bias point moves closer to FMR), we also expect a somewhat stronger fall-off in h_{crit} with increasing field than for parallel pumping. Some representative data for single crystal YIG at x-band are shown in fig. 3.17. In an FMR field sweep at moderate power levels, the low threshold in the 2–2.5 kOe range (at x-band) gives rise to a broad apparent absorption peak well below the FMR line (3–3.5 kOe at x-band). This bump was originally termed "subsidiary absorption" and the transverse pumping instability process often goes by this label.

We are now in a position to consider the origin of the "fine structure" shown in fig. 3.13. A schematic subsidiary absorption butterfly curve is indicated in fig. 3.18a. Consider one particular (h_{crit}, H) point on the butterfly curve, and two different types of experiments which would (in concept) show an instability at that point. Type I is indicated by the vertical arrow, and corresponds to an experiment in which the static field is held constant and the microwave field is gradually increased. Type II, indicated by the horizontal arrow, corresponds to an experiment in which the microwave field h is held constant and the static field is gradually increased.

The conventional approach has generally involved Type I experiments, indicated in fig. 3.18b. As the microwave field amplitude is gradually increased, the microwave absorption is small until point "A" is reached. At that power level, an abrupt increase in absorption occurs. Point A corresponds to h_{crit} (at

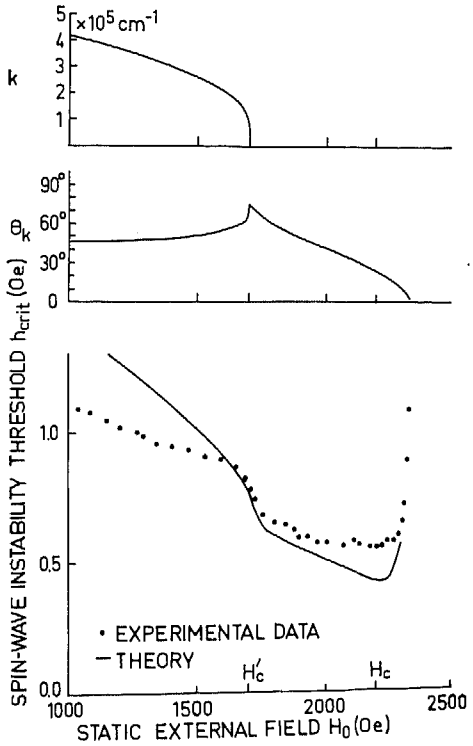

Fig. 3.17. Transverse pumping (subsidiary absorption) butterfly curve data for single crystal YIG (after Yakovlev et al. [145]).

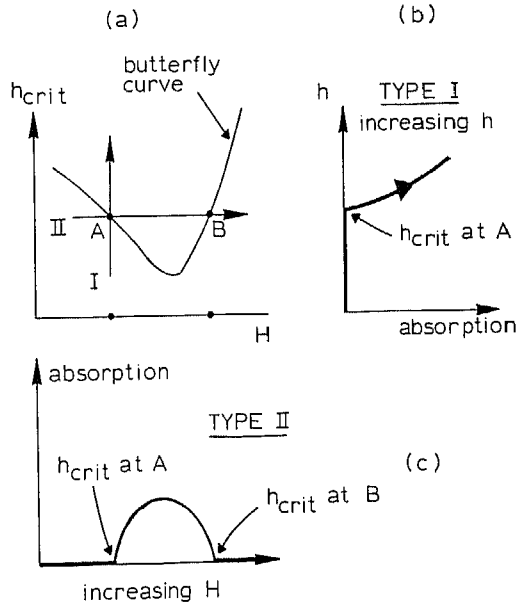

Fig. 3.18. Schematic description of "Type I" and "Type II" instability experiments.

the chosen field H). The second approach is indicated in fig. 3.18c. When the static field H is swept at constant h, one obtains a "bump" with abrupt cut-offs at points "A" and "B". This result is similar in principle to the subsidiary absorption peaks observed in the pioneering high power FMR studies. However, the use of stable fields and highly polished, narrow linewidth single crystal YIG samples allowed Jantz and Schneider to resolve the fascinating fine structure shown in fig. 3.13.

An expanded view of the fine structure at a lower power level is shown in fig. 3.19. The regular spacing and very narrow spikes are clearly in evidence. From a detailed analysis of the spacing versus field, Jantz and Schneider were able to connect the sequence of spikes within individual groups (such as the one in fig. 3.19 and the three somewhat overlapping groups in fig. 3.13) with jumps in k_z by π/d, where d is the sphere diameter, with the transverse component constant. A systematic change in spacing from group to group and overlap between groups appears to confirm this identification. The mode-peak correspondence is indicated schematically in fig. 3.20. Semiquantitative fits imply $|k|$ on the order of $10^4\,\mathrm{cm}^{-1}$. These results show that nonlinear effects can be used to great advantage in the study of fundamental excitations. Similar results are found in parallel pumping (Jantz, Schneider, and Andlauer [146]).

The above data reveal the presence of quantized spin-wave excitations in a rather graphic manner. The analysis indicates that intermediate k-values ($\sim 10^4\,\mathrm{cm}^{-1}$) are involved, and these are consistent with the dispersion constraints on k as indicated in fig. 3.14 (modified for transverse pumping). However, the gross structure of the instability evident in fig. 3.13 indicates that very low k modes in the magnetostatic regime ($k \sim 10$–$100\,\mathrm{cm}^{-1}$ for these sample sizes) also play a role.

Ignoring the fine structure and taking the edge of each group (points A and B in fig. 3.18) as a measure of h_{crit}, one obtains a rather complicated butterfly curve. The entire curve will be relevant to the discussion of section 3.4, but the bottom portion corresponding to the field interval over which fine structure is found is important here. This bottom portion is shown in fig. 3.21. It is noteworthy that the two sharp dips at 1700 Oe and 1875 Oe correspond precisely to the expected locations of the two lowest order magnetostatic modes with frequency $\omega/2$. Under the assumption that the instabilities correspond to $k \sim 10^4\,\mathrm{cm}^{-1}$ excitations, it appears that there is some interaction with degenerate ($\omega_k = \omega/2$) magnetostatic (low k) excitations which reduces the effective threshold substantially.

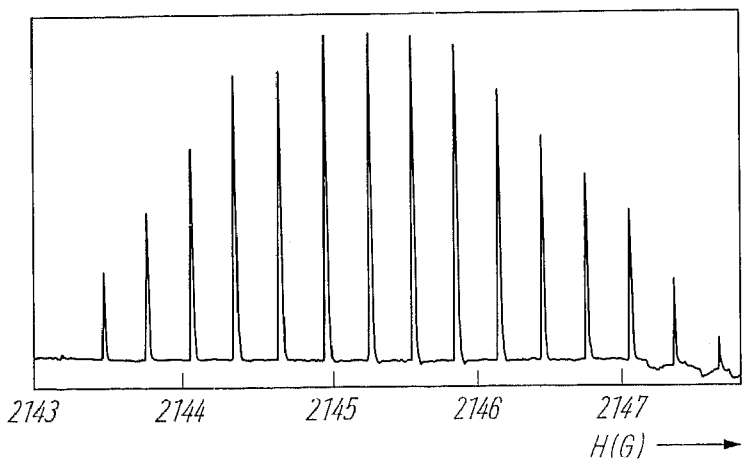

Fig. 3.19. Regular spacing and narrow spike widths for the subsidiary absorption fine structure in single crystal YIG (after Jantz and Schneider [144]).

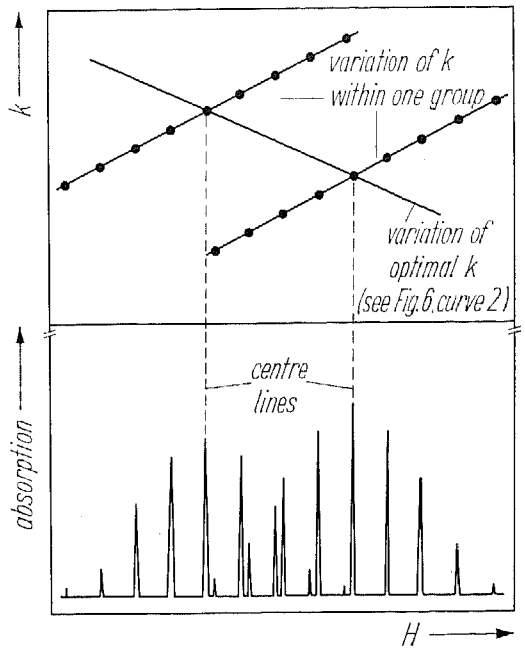

Fig. 3.20. Mode-peak correspondence for the fine structure spikes in the Jantz and Schneider experiments on subsidiary absorption (Jantz and Schneider [144]).

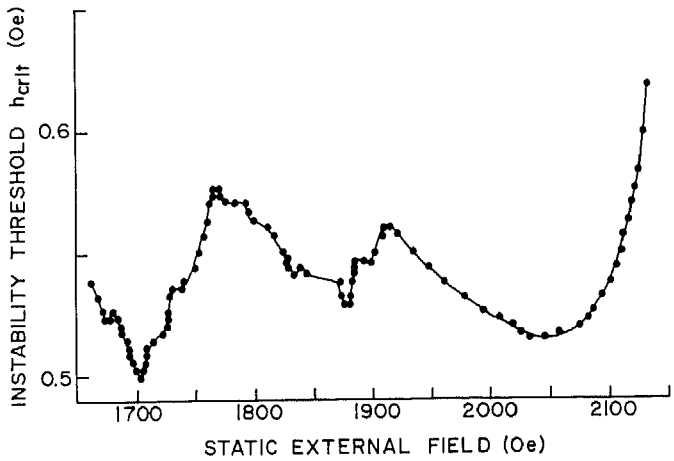

Fig. 3.21. Transverse pumping data for the "$k \simeq 0$" region of the butterfly curve in single crystal YIG (Patton and Jantz [147]).

There has also been work on the study of externally excited magnon by light scattering techniques. These were initially limited to Bragg scattering in the infrared on magnons derived by magneto-elastic conversion from transducer excited elastic waves. This work is reviewed by Hu and Morgenthaller [148]. Brillouin scattering has also been used to study parametric excitations in yttrium iron garnet by Venitskii et al. [149, 150, 151]. Their basic accomplishment was the direct observation of parallel pumped $k \simeq 0$ magnons by light scattering techniques. In order to detect the pumped magnons, very high power levels, larger than the critical power level for instability by a factor of 4–5, were needed. Wettling et al. [35]

and Wettling and Jantz [36] have used Brillouin scattering to study parametric excitations in $FeBO_3$. The initial intent was to use FMR to parametrically excite magnons and use the excitations to (among other things) study various aspects in fig. 3.9. Due to the large magneto-elastic coupling in $FeBO_3$, however, the parametric excitations have been identified as phonons. The coupling, in fact, is so strong that the scattered light is visible to the eye.

3.4. Relaxation

Relaxation processes for magnetic excitations have been of interest for over three decades, starting with the observation of FMR by Griffiths [152] and the theoretical explanation by Kittel [153] of the resonance condition. This subject is reviewed by Sparks [43] and Patton [141], with an emphasis on insulators, and by Bhagat [154] for metals. It is apparent from preceding sections that both light scattering and spin-wave instability experiments allow the examination of particular (ω_k, $\boldsymbol{k}$) magnons. Light scattering can probe thermal excitations, as considered in section 2. Instability experiments allow the somewhat indirect study of magnons excited well above thermal levels. This section considers aspects of magnon $\boldsymbol{k}$-dependent relaxation accessible by these two techniques, either alone or in combination.

For purposes of illustration, consider the case of three-magnon relaxation in YIG. In the limit of low k ($k \lesssim 10^6\,\mathrm{cm}^{-1}$), a spin-wave linewidth of the form

$$\Delta H_k = A + Bk \tag{3.18}$$

is often utilized. Detailed calculations indicate more complicated variations which involve both k and θ_k (see Sparks [43]). Experimental results on parallel pumping in single crystals (Sethares et al. [155]; Patton and Jantz [156]) indicate a possible ϕ_k dependence as well in some situations. The main point, for present purposes, is that relaxation can be (and often is) $\boldsymbol{k}$ dependent.

As mentioned in the previous section, spin-wave instability butterfly curves provide an indirect, albeit clear, indication of the $\boldsymbol{k}$-dependence of ΔH_k. Figure 3.15 underscores the role of the spin-wave linewidth rather nicely. The fact that the butterfly curve data tend to follow curve "B" rather than curve "A" (see fig. 3.16) is due to the increase in ΔH_k with wavenumber.

There are, however, several notable exceptions to the simple smooth behavior of curve "B" in fig. 3.16, which are now believed to indicate a more decisive role of $\boldsymbol{k}$-dependent relaxation in nonlinear phenomena. The earliest report of "anomalous" behavior was for parallel pumping in [110] magnetized YIG single crystals (Sethares et al. [155]). Their data are indicated by the solid points in fig. 3.22. These authors observed a peculiar double minimum structure. They noted (correctly) that the low field minimum (H_c') corresponded to the field at which the ($\phi_k = 0$, $\theta_k = 90°$) magnon at $\omega_k = \omega/2$ has zero k, while the high field minimum (H_c) corresponded to the same conditions for $\phi_k = 90°$. (The pertinent spin-wave dispersion is shown in fig. 3.5, as discussed earlier.) A full theoretical analysis of parallel pumping which includes anisotropy (Haubenreisser and Linzen [157]), however, shows that the coupling is strongest for $\phi_k = 90°$ magnons. In other words, the low field (H_c') dip in fig. 3.22 should not appear.

It has recently been pointed out (Patton and Jantz [156]; Patton [89]) that the above "anomaly" is a result of $\boldsymbol{k}$-dependent relaxation. This dependence leads to rather abrupt changes in $\boldsymbol{k}$ as one moves up in static field. The net effect is the double minimum butterfly curve of fig. 3.22.

The basic effect is easily explained by considering the various parameters which tend to minimize h_c (and hence correspond to the observed h_{crit}): (1) The coupling term, essentially as given in eq. (3.16) but

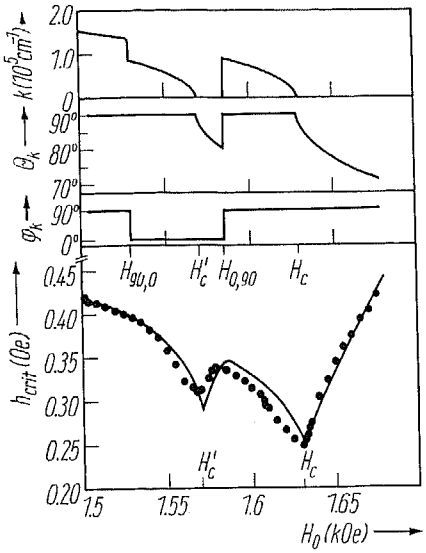

Fig. 3.22. Parallel pump butterfly curve data (after Sethares et al. [155]) and theory (after Patton [142]).

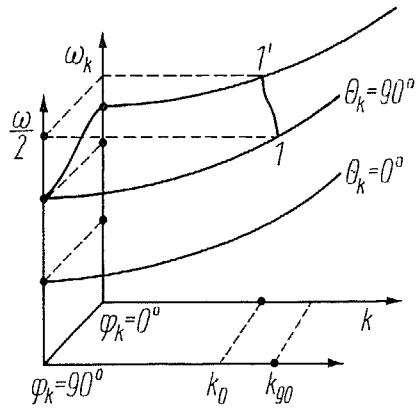

Fig. 3.23. Spin-wave manifold for [110] magnetized YIG.

with additional terms involving ϕ_k, "favor" modes with $\phi_k = 90°$. (2) The ΔH_k factor in eq. (3.16) given by eq. (3.18), "favors" modes with minimum $|k|$. These two tendencies are in competition, as can be seen from the dispersion picture in fig. 3.23. The $\omega_k = \omega/2$ cut in the favored branch surface at $\theta_k = 90°$ is indicated by the line from (1) to (1'). It is seen that (1) corresponds to $\phi_k = 90°$ while (1') corresponds to minimum $|k|$. Whichever point yields, by numerical calculation, the lowest h_c will correspond to the observed h_{crit}.

A quantitative calculation based on an educated guess for ΔH_k,

$$\Delta H_k = A + Bk + C\sin^2(2\theta_k) + E\sin^2(2\phi_k)\,, \tag{3.19}$$

yielded the theoretical results summarized in fig. 3.22. We see that, apart from a field interval, $H_{90,0} < H < H_{0,90}$, the $\phi_k = 90°$ preference "wins" and the expected butterfly is obtained. In this 50 Oe interval, however, the unstable spin wave actually flips from $\phi_k = 90°$ to $\phi_k = 0°$ due to the minimum $|k|$ preference. This leads directly to the low field dip and the double minimum structure for the [110] parallel pump butterfly curve. We have, in effect, a spin-wave switch at the two flip fields. Apart from the empirical ϕ_k term in eq. (3.19), the other dependencies are more or less in agreement with theoretical predictions.

The k-dependent relaxation in single crystal YIG also has an important influence on the transverse pumping (subsidiary absorption) butterfly curves. One such effect is the shoulder in fig. 3.17 at about 1700 Oe (H'_c). The essential results of a more extensive study of subsidiary absorption (Patton and Jantz [147]) are shown in fig. 3.24. Data, obtained by method II in section 3.3, a theoretical fit, and the (k, θ_k) variations obtained from the theory are given. Perhaps the most interesting (and previously unsuspected) result is the abrupt drop in k as H exceeds 1500 Oe. In the context of the spin-wave theory, "$k = 0$" simply means negligible Dk^2. For $k \sim 10^4\,\mathrm{cm}^{-1}$, as suggested by the Jantz fine structure data, Dk^2 is on the order of a few Oe or less. We see, then, that there is an appreciable field interval,

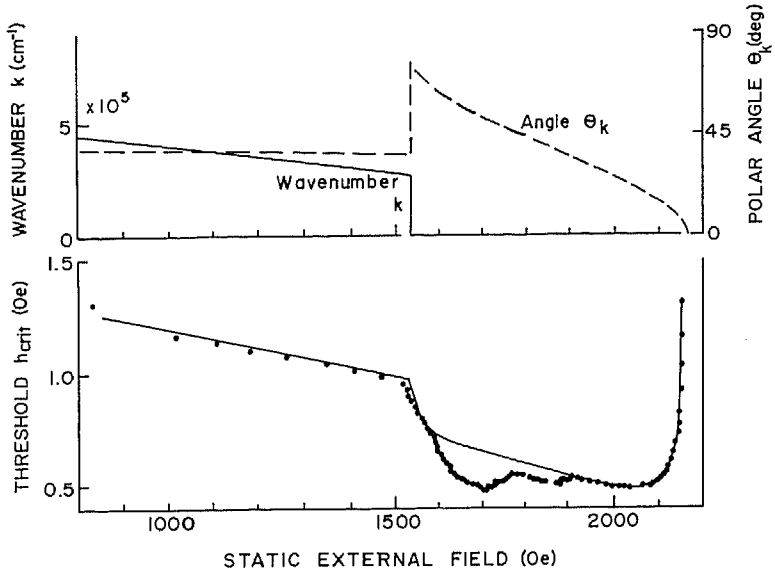

Fig. 3.24. Subsidiary absorption butterfly curve data, and theoretical fits for [111] magnetized YIG at x-band (after Patton and Jantz [147]).

extending well below the previously assigned "$k = 0$" transition at $H_{45} \sim 2000$ Oe, where the instability of low k ($\gtrsim 10^4\,\mathrm{cm}^{-1}$) mode dominates.

The structure between the "kink" field of 1500 Oe and 2000 Oe was shown in fig. 3.21 and shown to be connected with magnetostatic mode interactions. The actual instability onset curves near the kink field are also of considerable interest. A series of typical recorder traces of absorption vs. static field (increasing) are shown in fig. 3.25. As the power level is increased above -4.6 db (db down from maximum power), we see a small jump at static fields somewhat higher than that for initial instability. These jumps appear to be due to a second instability for modes at $k \sim (2\text{–}3) \times 10^5\,\mathrm{cm}^{-1}$ and $\theta_k \sim 45°$.

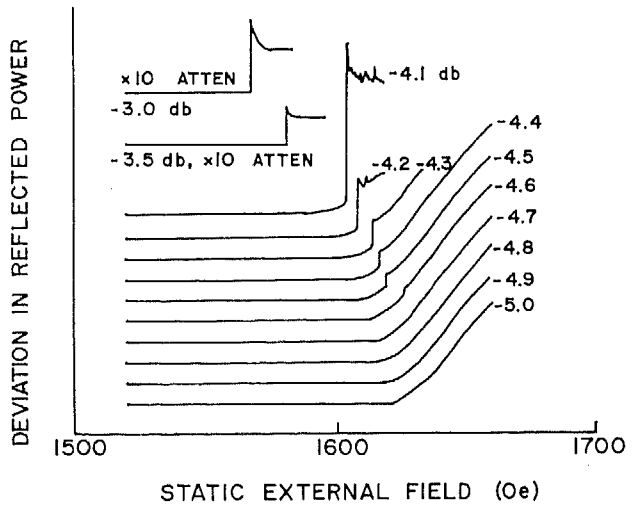

Fig. 3.25. Spin-wave instability onset character near the "kink" field (after Patton and Jantz [147]).

These same modes constitute the dominant instability below the kink field. We therefore have two groups of spin-wave modes simultaneously excited well above thermal levels, one at low k and $\theta_k \sim 70$–$80°$ and one at high k and $\theta_k \sim 45°$. The former instability is switched on abruptly at the kink field.

Experiments for various intermediate directions of the microwave field from parallel (as in fig. 3.22) to perpendicular (as in fig. 3.24) have been carried out by Liu and Patton [158]. These additional data, in combination with theory, provide several new facts concerning spin-wave instability and relaxation. First, the data indicate that the pumping due to the parallel and perpendicular components of the microwave field is not cooperative. The theory for intermediate angles, $0 < \Psi < 90°$, yields (Patton [89, 142])

$$1/h_{\text{crit}}^{\text{obl}} = \max(\cos\Psi/h_c^{\parallel} - \sin\Psi/h_c^{\perp}) . \tag{3.20}$$

The data indicate that the actual behavior follows

$$h_{\text{crit}}^{\text{obl}} = \min(h_{\text{crit}}^{\parallel}/\cos\Psi,\ h_{\text{crit}}^{\perp}/\sin\Psi) . \tag{3.21}$$

In the above, $h_{\text{crit}}^{\text{obl}}$ is the predicted microwave field amplitude for the onset of spin-wave instability, $h_c^{\parallel}$ and $h_c^{\perp}$ are the spin-wave angle dependent threshold expressions from the separate theories for parallel and transverse pumping, and $h_{\text{crit}}^{\parallel}$ and $h_{\text{crit}}^{\perp}$ are minimum values of $h_c^{\parallel}$ and $h_c^{\perp}$ with respect to θ_k and ϕ_k. All minimization and maximization are subject to the usual constraint $\omega_k = \omega/2$. The observation that the data follow eq. (3.21) indicates that the spin system selects either $h_{\text{crit}}^{\parallel}$ or $h_{\text{crit}}^{\perp}$, depending on which one is lower, *not* some value lower than either of them [eq. (3.20)].

The second result concerns the wavevector k-dependence of ΔH_k. To explain all of the oblique pump data, in addition to the use of eq. (3.21), it is necessary to invoke a $\Delta H_k(k)$ function somewhat more involved than shown in eq. (3.19). For all pump angles except 90°, a ΔH_k of

$$\Delta H_k = A_0 + A_1 \sin^2 2\theta_k + B_1 L(k/B_2) , \tag{3.22}$$

with

$$L(x) = \frac{1}{1.39x} \ln\left[1 + \frac{8x^2(1+2x^2)}{1+8x^2}\right] . \tag{3.23}$$

This functional form is loosely consistent with the three magnon relaxation calculation of Sparks [43], but must be regarded as phenomenological in the absence of any rigorous theory. To fit the data for the range of Ψ, however, it was necessary to let the B_1 coefficient vary with Ψ. For perpendicular pumping, the data could not be fitted very well by eq. (3.22). Instead, the following form was found to work best:

$$\Delta H_k = A_0 + A_1 \sin^2\theta_k , \qquad k = 0 , \tag{3.24}$$

$$\Delta H_k = A_2 + B_1 L(k/B_2) , \qquad k \neq 0 . \tag{3.25}$$

The reasons and theoretical justification for these complex variations in $\Delta H_k(k)$ with pump angle remain unresolved.

Apart from the spin-wave instability experiments discussed above, there has been very little experimental work to determine the k-dependence of the magnon relaxation or linewidth in magnetic systems. That which has been reported has generally been for standing spin-wave resonance excitations in thin films, discussed in sections 2.3 and 3.1.

Brillouin scattering would appear to be an ideal way to measure magnon linewidths. The published data on narrow linewidth material, namely YIG with $\Delta H_k \gtrsim 1$ Oe at room temperature, however, yields light scattering peaks which are a thousand times broader than intrinsic linewidths (see fig. 2.5). Under such circumstances, the measurement of intrinsic linewidth variations with k is not possible.

The situation is somewhat better in the case of metals, because of their larger intrinsic linewidths. As illustrated in fig. 2.10, the surface magnon peak broadens as the angle between k and field approaches the critical angle for surface mode propagation. This appears to be more a reflection of the virtual surface branch character of section 2.4 than any intrinsic k-dependent relaxation *per se*. Sandercock and Wettling [21] explain the broadening in terms of scattering to degenerate volume magnons (fig. 2.27). In general, the linewidths observed for metals are on the order of or somewhat larger than those expected from FMR. Broader lines are expected for the bulk magnons because of the skin depth and uncertainty principle limitations discussed in section 2.4.

The only specific data on linewidth and relaxation by Brillouin scattering (to the author's knowledge) are for $CrBr_3$ (Sandercock [15]). His data on intensity and linewidth vs. temperature for $\omega_k \sim 20$ GHz are shown in fig. 3.26. Linewidths in the ferromagnetic region are about 40–50 MHz, corresponding to 15–20 Oe. Interestingly, the data extend into the paramagnetic region above $T_c \sim 32$°K. A resolution of 10 MHz was achieved by scanning the output of a 5-pass Fabry–Perot with a confocal interferometer having a narrow spectral range of about 300 MHz. The confocal instrument was operated in tandem with the five pass interferometer, and the laser source was locked to an external reference cavity. We note that 10 MHz resolution corresponds to a linewidth of 3.5 Oe.

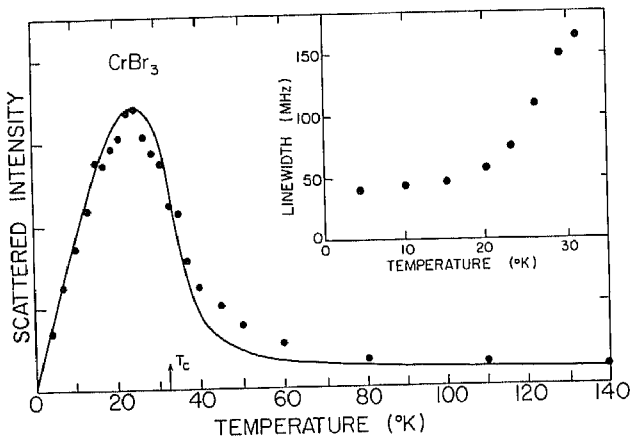

Fig. 3.26. Backscattering intensity and linewidth vs. temperature for $CrBr_3$, excitation at $\omega_k \sim 20$ GHz (after Sandercock [15]).

4. Magnon light scattering techniques

The previous two sections have provided a review of magnon excitations of moderate frequency (up to about 1000 GHz) in net-moment systems. This chapter considers the experimental light scattering techniques used to observe such excitations, with emphasis on Brillouin scattering. Conventional

Brillouin scattering has been used to study excitations in solids in the 1–30 GHz range. With recent innovations described below, the upper limit can likely be extended into the range usually accessed by Raman scattering, up to 1000 GHz or so in some situations. A general survey of experimental methods in light scattering spectroscopy is given by Cummins [159]. Recent advances in Brillouin scattering are surveyed by Sandercock [11, 12, 13].

Section 4.1 describes the basic experiment and the conventional plane-mirror Fabry–Perot interferometer used to analyze Brillouin scattering spectra in many cases. Section 4.2 describes recent advances which achieve high contrast and increased long-term stability, mainly due to John Sandercock [10, 11]. Section 4.3 presents a brief description of recent innovations (Sandercock [14]) which make single PZT (piezoelectric transducer) scanning and tandem operation possible, in addition to the previous improvements.

4.1. Fabry–Perot interferometry

The basic Brillouin light scattering experiment is straightforward. Incident light at frequency ω_{inc} from a single moded laser, with wavevector $\boldsymbol{k}_{inc}$, impinges on and penetrates the surface of a magnetic sample. Excitations within the material at some frequency ω_{ex} and wavevector $\boldsymbol{k}_{ex}$ interact with the light to produce a scattered wave at $\omega_{sc} = \omega_{inc} + \omega_{ex}$ and $\boldsymbol{k}_{sc} = \boldsymbol{k}_{inc} + \boldsymbol{k}_{ex}$. In most cases, the emission of an excitation is also possible and a down shifted photon ($\omega_{sc} = \omega_{inc} - \omega_{ex}$) is also possible. For excitations in the 1–100 GHz range discussed in previous chapters, the condition $\omega_{inc} \gg \omega_{ex}$ is generally well satisfied, so that $|k_{inc}|$ and $|k_{sc}|$ are nearly equal (for isotropic optical media). The key experimental challenge is to resolve the relatively small frequency shift of $\pm\omega_{ex}$ and use these shifts to study the properties of the excitations of interest, in this case magnons.

Such experiments are generally done with Fabry–Perot interferometers. A survey of various approaches is given by Cummins [159]. For the frequency ranges of importance for magnons (tens to hundreds of GHz), plane mirror Fabry–Perot systems are needed. A conventional mirror configuration with piezoelectric transducer (PZT) scanning is indicated in fig. 4.1. As a function of the mirror spacing L, a transmission peak for a given wavelength λ will occur for $n\lambda = 2L$. For a fixed separation and a given order n, the frequency shift from one peak in transmission to another is

$$\Delta\nu = c/2L\,, \tag{4.1}$$

where c is the speed of light. We may conveniently define this frequency shift as the free spectral range (FSR). For $L = 2$ mm, the FSR is about 75 GHz.

Several other instrument parameters are of importance: the finesse F, the peak transmission T, and the contrast C. The finesse is defined as the ratio of the peak separation (FSR) to the half-width $\delta\nu$ of an individual transmission peak for monochromatic light,

$$F = \Delta\nu/\delta\nu\,. \tag{4.2}$$

Finesse is determined by a number of factors which include mirror reflectivity, mirror flatness, aperture size, etc. The first two may be expressed quantitatively as a reflectivity finesse

$$F_R = \pi R/(1-R)\,, \tag{4.3}$$

related to the mirror reflectivity R, and a surface finesse,

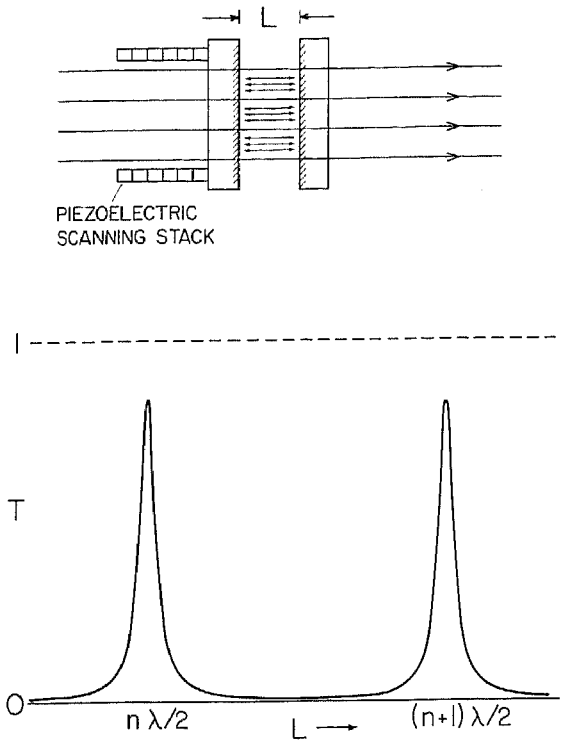

Fig. 4.1. Fabry–Perot mirror pair with PZT scanning; interferometer transmission function (after Sandercock [11]).

$$F_S = m/2\,, \tag{4.4}$$

for a mirror surface flat to λ/m. The total finesse, considering these two terms only, is given by a parallel impedance type equation,

$$\frac{1}{F} = \frac{1}{F_R} + \frac{1}{F_S}\,. \tag{4.5}$$

We see that the total system finesse will be somewhat smaller than the smallest individual contribution. If the reflectivity is high, the surface finesse is the limiting factor. For typical values of R (above 0.9) and m (100 or 200 for good mirrors), the overall system finesse is about 50–100 for a well designed system.

The peak transmission is determined by the mirror reflectivity and absorption. The absorption term is

$$T_A = \left(1 - \frac{A}{1-R}\right)^2, \tag{4.6}$$

where A is the mirror absorption factor. It is evident from eqs. (4.3) and (4.6) that one pays the price of reduced transmission to have a high reflectivity finesse.

The contrast C is the ratio of the maximum transmission at a peak to the minimum transmission

between peaks. For a reasonable finesse (ten or better), the contrast is

$$C \simeq 4F^2/\pi^2 . \tag{4.7}$$

For a system with the finesse limited by the mirror flatness, the system finesse can be no greater than a few hundred. Contrast limits are therefore about 10^4–10^5. The requirement $F_k > F_S$ puts the transmission at a fraction of one percent. We therefore see that the contrast of the simple plane-parallel Fabry–Perot is limited to moderate values (for our purposes) on the order of 10^5. Even these moderate values, however, require a rather low transmission.

4.2. Multipass and stabilization techniques

As evident from some of the light scattering data discussed in previous chapters, a contrast of 10^9 or greater is desirable for the observation of magnon excitations in many cases. Well resolved peaks, moreover, require extended data accumulation times. Both of these features have been realized in the design of a multipass Febry–Perot interferometer with electronic-feedback stabilization, with the pioneering work by Sandercock [10, 11].

Pertinent design considerations for a general multipass configuration have been described by Sandercock [11], and a representative 5-pass system is indicated in fig. 4.2. Consider the contrast enhancement for p passes over the one pass contrast C_1,

$$C = C_1^p . \tag{4.8}$$

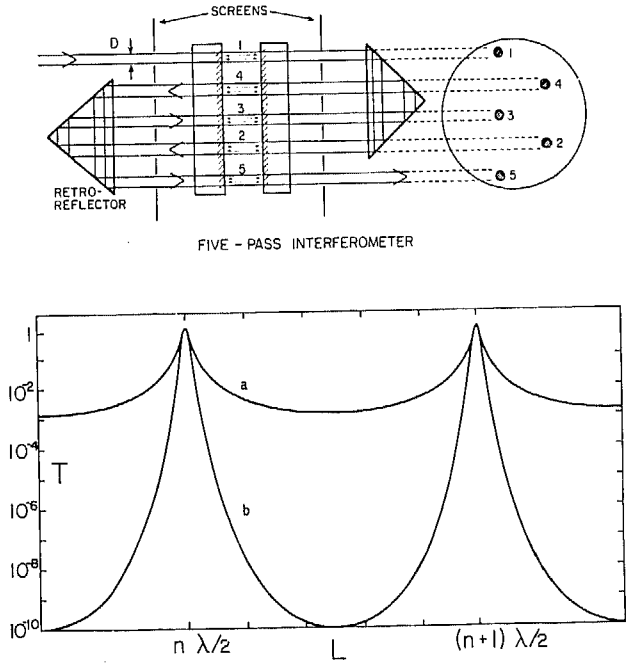

Fig. 4.2. Five-pass Fabry–Perot configuration and a theoretical transmission curve (after Sandercock [11]).

Denoting the single pass finesse in eq. (4.7) by F_1, we see that a rather large contrast is possible for a reasonably small F_1. For $p = 5$ and $C = 10^{10}$ (following Sandercock [11]), one obtains $F_1 = 15.7$. This is easily achieved by using mirrors of moderate quality, say $\lambda/100$ flatness, and a small reflectivity finesse. For $\lambda/100$ mirrors and $F_R \simeq 17.5$, we obtain the desired high contrast and a reasonable transmission as well. For a mirror absorption factor of 0.2%, the above parameters yield an estimated transmission of about 70% (Sandercock [11]).

The actual Sandercock system, used for a number of the experimental results discussed previously, utilized $\lambda/100$ mirrors coated for 86% reflectivity. In a five-pass configuration, the overall finesse of 40 yielded a contrast ratio in excess of 10^9 with a transmission of 50%. The contrast enhancement is indicated in fig. 4.2. A comparison of spectra obtained with a one-pass and a two-pass configuration is shown in fig. 4.3. The contrast enhancement, even with two passes, is significant.

In addition to optical design, a number of mechanical considerations are crucial to the realization of a useful interferometer. The first of these involves scanning. To obtain Brillouin spectra as shown in fig. 4.3 and earlier sections, it is necessary to simultaneously change the mirror spacing in a smooth and continuous manner, and at the same time retain a high degree of parallelism between the two mirrors. The standard approach used in a number of commercial instruments (Burleigh and Tropel, for example) is to align the mirrors and then do a slow scan by means of the PZT drive elements mounted on the circumference of the movable mirror. Drift in parallelism usually limits scan times to five minutes or less, with the same time limit for signal averaging.

A more sophisticated (and more complicated) approach, developed and successfully implemented by

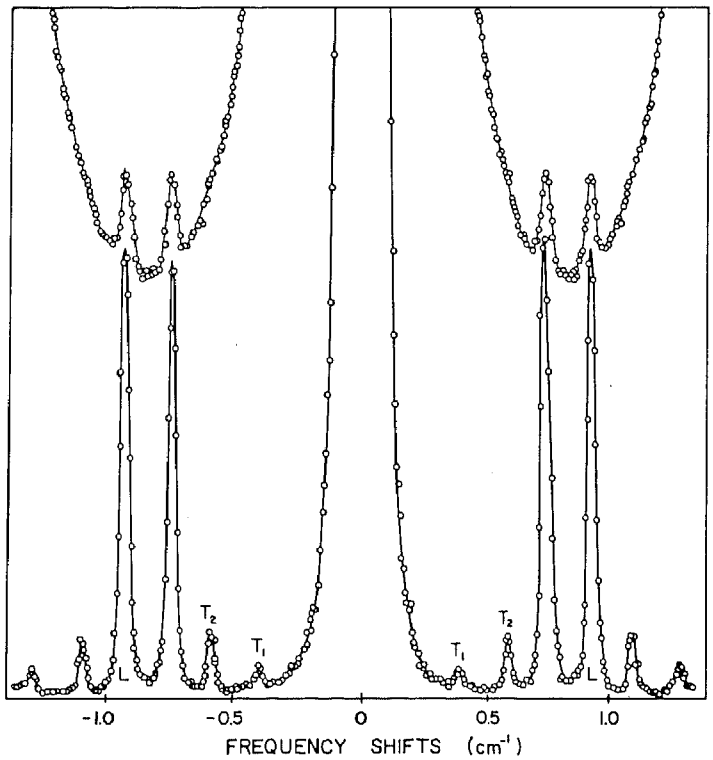

Fig. 4.3. Comparison of Brillouin scattering spectrum for a single pass and a double pass Fabry–Perot (after Sandercock [10]).

Sandercock, is to use a repetitive scan (at a few Hz), in combination with a feedback scheme to maintain parallelism. His approach is summarized in fig. 4.4. The PZT X- and Y-stacks serve dual functions. (1) They are used to provide the linear scan, driven by the sawtooth wave indicated by the upper "logic signal". (2) In addition, plus and minus error signals are applied to the X-stack during two successive cycles of the scan ramp, and then plus and minus error signals are applied to the Y-stack during the next two successive cycles of the scan ramp. The peak transmission at the laser frequency, indicated by the off-scale maximum at $0\,cm^{-1}$ in fig. 4.3, will be maximum when the mirrors are parallel. The change in peak transmission due to the error signal pulses can therefore be used in a feedback scheme to lock the mirrors into parallelism as the system is repetitively scanned over the Rayleigh peak. The schematic circuitry in fig. 4.4 uses these variations in peak transmission due to the X- and Y-stack modulations to electronically lock and system into parallelism.

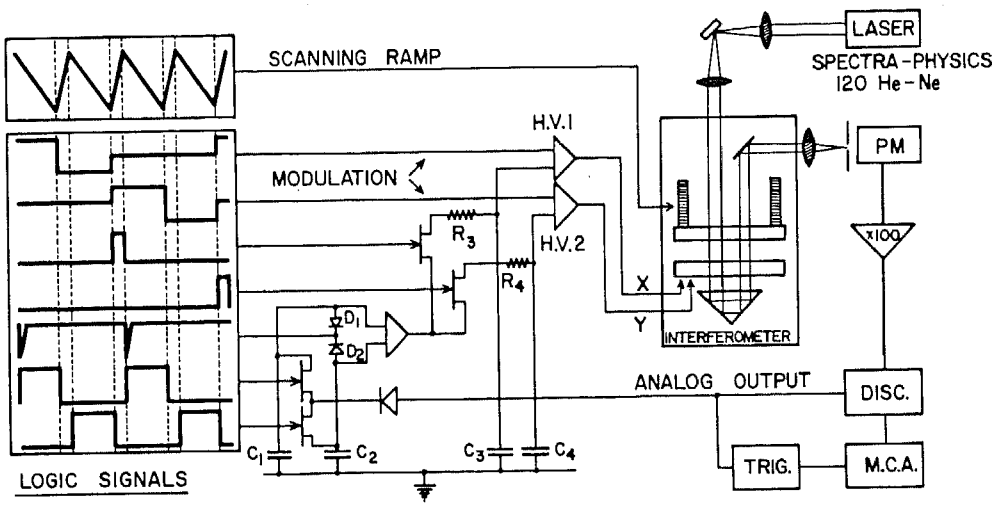

Fig. 4.4. Schematic lay-out of a rapid scanned, stabilized Fabry–Perot system (after Sandercock [10]).

With this system data accumulation periods can be extended from minutes to hours of drift free operation. Systems designed along the lines described above have been used in a number of the studies discussed in earlier chapters, notably, those on YIG (Sandercock and Wettling [16, 17]), $CrBr_3$ (Sandercock [15]), and $FeBO_3$ (Jantz et al. [26]; Jantz and Wettling [27, 28]). Commercial systems with feedback stabilization have recently become available from Burleigh Instruments, Inc., based on the above principle and specific circuits described by Bechtle [160, 161]. The latter paper describes a digital version of the stabilization electronics. Technical aspects of the feedback stabilization instrumentation and multipass techniques are also discussed in several technical memos by Burleigh Instruments, Inc. [162, 163]. A stabilization technique for interferometers used in a fixed frequency mode (unscanned) has been described by Vacher et al. [164]. In this scheme, an additional reference signal at the same position as the excitation of interest is used for stabilization. This intense line is shuttered off when the signal of interest is being sampled.

4.3. Mechanically scanned tandem operation

There are two basic limitations for plane-parallel Fabry–Perot interferometers, as far as magnon studies are concerned. The first is the practical limitation on the minimum mirror separation, and the

corresponding limit on the FSR. A typical large spacing of 2 mm yields an FSR of 75 GHz, as remarked previously. A very small spacing of 0.25 mm (which is probably as small as one would risk!) yields 600 GHz. The bandwidth and resolution in this later case would degrade to 10 GHz or more, with most typical magnon lines poorly resolved. The second limitation, also related to the FSR, is the bandwidth. Large FSR means a large bandwidth and poor resolution. To achieve a very high resolution, in the tens of MHz range for some magnon studies of interest, one must accept a rather small FSR of a few GHz at best (see eq. (4.2)).

Tandem systems, consisting of two Fabry–Perot interferometers in series which are synchronously scanned in some manner, provide an elegant solution to the problem of large FSR, narrow bandwidth Brillouin scattering spectroscopy. There have been two basic approaches. Cannel (as described by Cummins [159]) has utilized gas pressure variations to achieve synchronous scanning of the two interferometers. More recently, Sandercock [14] has devised a way to achieve tandem operation with mechanical scanning, along with feedback for mirror parallelism stabilization as discussed in the previous section. There are two important innovations involved in the design of a mechanically scanned tandem system. The first has to do with the linear scan technique and the second has to do with tandem operation. A schematic drawing to demonstrate the linear scan technique is shown in fig. 4.5. The essential ingredient is the "deformable parallelogram" composed of two parallel plates connected by two thin rectangular sheets of spring steel. If the parallelism of the seating grooves for the spring steel rectangles is kept within 10 μ, the constrained relative motion of the two plates will be parallel for displacements up to several hundred light wavelengths. Given this convenient state of affairs, a single PZT element can be used in conjunction with a capacitance motion detector to obtain a highly linear scan.

Care must be taken to utilize torsion free mountings for the transducer element, which is easily accomplished by the use of magnetic washer-ball bearing contacts. Mirror alignment and feedback to maintain parallelism is accomplished by mechanical and piezo-electric adjustments at the stationary, alignable mirror holder. Adjustment of the Fabry–Perot mirror separation is done by moving the lower plate back and forth on the races indicated in fig. 4.5. A recently available commercial translation stage

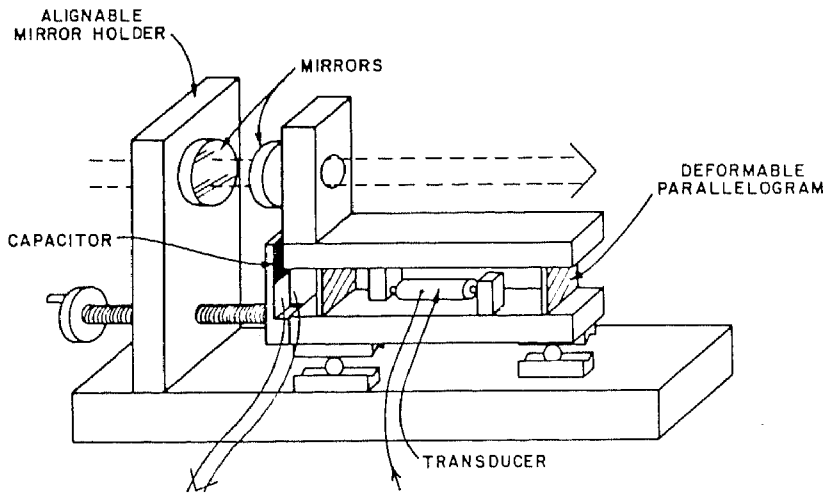

Fig. 4.5. Schematic drawing of Sandercock's single PZT drive scheme for a Fabry–Perot interferometer (Sandercock, private communication, 1978).

(Schneeberger, Bern) has been found to be capable of providing the near optical tracking required to maintain reasonable mirror parallelism during mirror separation adjustments.

The second feature of Sandercock's mechanical tandem design involves the use of the single PZT scanning to achieve tandem operation. The essential ingredients are indicated in fig. 4.6. In the tandem system, the moving mirror elements of two separate Fabry–Perot mirror pairs are mounted on the translation stage described above, with mirror axes at an angle θ as indicated. Since the spacing for an individual mirror pair determines the separation in frequency between Rayleigh peaks for that pair, the use of a tandem system with mirror pairs of different separations yield a greatly increased free spectral range. For the common PZT scan drive to yield tracking frequency shifts for the two Fabry–Perot interferometers, the spacings L_1 and L_2 must be related by

$$L_2 = L_1 \cos\theta . \tag{4.9}$$

Feedback stabilization for mirror parallelism of both mirror pairs is done as described in section 4.2, except that a total of eight scans, rather than four, are required for each sample sequence in the feedback loop.

A system incorporating the above features, with a spacing ratio of 15/16 ($\theta \sim 20°$), was used by Sandercock and Wettling [20, 21] to obtain the data on Fe and Ni discussed in section 2. The chief advantage of this particular system was in the achievement of a large effective FSR. For $\theta \sim 20°$, the individual mirror separations are still about the same so that the bandwidth is still roughly the same as for a single interferometer (assuming a similar finesse for both). For our 2 mm spacing of section 4.1 with $F \sim 50$, the bandwidth is on the order of a few GHz or so.

Dil et al. [165] have discussed techniques for synchronizing two separate Fabry–Perot interferometers for tandem operations by purely electronic means. Details on a mechanical tandem design following the Sandercock approach have recently been published by Lindsay et al. [166].

The simultaneous achievement of large FSR and narrow bandwidth is generally accomplished by operating a plane-parallel interferometer (large FSR) in series with a spherical Fabry–Perot (Cummins [159]; Sandercock [15]). Using a rather intricate technique Sandercock [15] was able to synchronize the two interferometers as well. Insofar as spherical interferometers are reasonably stable, feedback stabilization was needed only for the plane-parallel Fabry–Perot. We see from fig. 4.6 and eq. (4.9) that

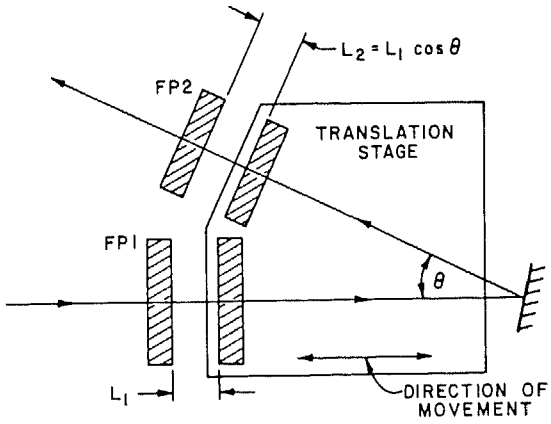

Fig. 4.6. Schematic illustration of the Sandercock drive system for a mechanically scanned tandem Fabry–Perot interferometer.

the combination of a large FSR (small L_2) and narrow bandwidth (large L_1) is possible only for rather large angles. Sandercock (private communication) has recently achieved synchronized, tandem operation for a spherical interferometer (in the place of the #1 mirror pair in fig. 4.6) and a plane-parallel Fabry–Perot. The practical limit on achievable bandwidth is on the order of 10 MHz.

Acknowledgements

The author is grateful to Dr. Sanford Kern and Dr. Wolfram Wettling for helpful comments on the manuscript, to Ms. Mary Spencer for her diligent attention and patience in typing the many versions, and to Mr. Todd Harvey and Mr. Glen Sunada for help in assembling references and figures for the final manuscript.

References

[1] C. Kittel, Phys. Rev. 110 (1958) 1295.
[2] M.H. Seavey and P.E. Tannenwald, Phys. Rev. Lett. 1 (1958) 168.
[3] H. Puszkarski, Acta Physica Polonica A38 (1970) 217.
[4] P.E. Wigen, T.S. Stakelon, H. Puszkarski, and P. Yen, AIP Conf. Proc. 29 (1976) 670.
[5] T. Wolfram and R.E. DeWames, Progr. Surface Sci. 2 (1972) 233.
[6] B.R. Tittmann and R.E. DeWames, Phys. Lett. 30A (1969) 499.
[7] R. Henry, S.D. Brown, P.E. Wigen, and P.J. Besser, Phys. Rev. Lett. 28 (1972) 1272.
[8] R.E. Camley and D.L. Mills, Phys. Rev. B18 (1978) 4821.
[9] M. Grimsditch, A. Malozemoff, and A. Brunsch, Phys. Rev. Lett. 43 (1979) 711.
[10] J.R. Sandercock, Optics Commun. 2 (1970) 73.
[11] J.R. Sandercock, Proc. 2nd. Conf. Light Scattering in Solids (Paris, Flamarion, 1971) p. 9.
[12] J.R. Sandercock, RCA Rev. 36 (1975) 89.
[13] J.R. Sandercock, Proc. 3rd Int. Conf. Light Scattering in Solids (New York, Wiley, 1976) p. 219.
[14] J.R. Sandercock, Topics in Applied Physics 51: Light Scattering in Solids III, eds. M. Cardona and G. Guntherodt (Berlin Heidelberg, Springer-Verlag, 1982).
[15] J.R. Sandercock, Solid State Commun. 15 (1974) 1715.
[16] J.R. Sandercock and W. Wettling, Solid State Commun. 13 (1973) 1729.
[17] J.R. Sandercock and W. Wettling, AIP Conf. Proc. 18 (1974) 935.
[18] W. Wettling, M.G. Cottam, and J.R. Sandercock, J. Phys. C: Solid St. 8 (1975) 211.
[19] P. Grünberg and F. Metawe, Phys. Rev. Lett. 39 (1977) 1561.
[20] J.R. Sandercock and W. Wettling, IEEE Trans. Magnetics 14 (1978) 442.
[21] J.R. Sandercock and W. Wettling, J. Appl. Phys. 50 (1979) 7784.
[22] F. Metawe and P. Grünberg, J. Magn. Magn. Mat. 9 (1978) 80.
[23] P.H. Chang, A.P. Malozemoff, M. Grimsditch, W. Senn, and G. Winterling, Solid State Commun. 27 (1978) 617.
[24] A.P. Malozemoff, M. Grimsditch, J. Aboaf, and A. Brunsch, J. Appl. Phys. 50 (1979) 5885.
[25] A.P. Malozemoff, P.H. Chang, and M. Grimsditch, J. Appl. Phys. 50 (1979) 5896.
[26] W. Jantz, J.R. Sandercock, and W. Wettling, J. Phys. C: Solid St. 9 (1976) 2229.
[27] W. Jantz and W. Wettling, Appl. Phys. 15 (1978) 399.
[28] W. Jantz and W. Wettling, IEEE Trans. Magnetics 14 (1978) 716.
[29] A.S. Borovik-Romanov, V.G. Zhotikov, N.M. Kreines, and A.A. Pankov, JETP Lett. 24 (1977) 207.
[30] A.S. Borovik-Romanov, V.G. Zhotikov, and N.M. Kreines, Sov. Phys. JETP 47 (1978) 1188.
[31] A.S. Borovik-Romanov, V.G. Zhotikov, N.M. Kreines, and A.A. Pankov, Physica 86–88B (1977) 1275.
[32] W. Wettling, W.D. Wilber, and C.E. Patton, J. Appl. Phys. 53 (1982) 8163.
[33] V.G. Zhotikov and N.M. Kreines, Sov. Phys. JETP Lett. 26 (1977) 360.
[34] V.C. Zhotikov and N.M. Kreines, JETP 50 (1979) 1202.
[35] W. Wettling, W. Jantz, and C.E. Patton, J. Appl. Phys. 50 (1979) 2030.
[36] W. Wettling and W. Jantz, Appl. Phys. 19 (1979) 175.

[37] P. Grünberg, M.G. Cottam, W. Vach, C. Mayr, and R.E. Camley, J. Appl. Phys. 53 (1982) 2078.
[38] W.D. Wilber, P. Kabos, and C.E. Patton, IEEE Trans. Magnetics 19 (1983) in press.
[39] A.S. Borovik-Romanov and N.M. Kreines, J. Magn. Magn. Mat. 15–18 (1980) 760.
[40] A.S. Borovik-Romanov and N.M. Kreines, Phys. Reports 81 (1982) 351.
[41] A.S. Borovik-Romanov and N.M. Kreines, J. Appl. Phys. 53 (1982) 8157.
[42] J.G. Dil, Rep. Prog. Phys. 45 (1982) 295.
[43] M. Sparks, Ferromagnetic Relaxation Theory (New York, McGraw-Hill, 1964).
[44] T. Holstein and H. Primakoff, Phys. Rev. 58 (1940) 1098.
[45] R.E. Camley, P. Grünberg, and C.M. Mayr, Phys. Rev. B26 (1982) 2609.
[46] P.A. Bates, M.G. Cottam, and S.R.P. Smith, J. Magn. Magn. Mat. 15–18 (1980) 771.
[47] L. Walker, Phys. Rev. 105 (1957) 390.
[48] L. Walker, J. Appl. Phys. 29 (1958) 318.
[49] R.W. Damon and J.R. Eshbach, J. Phys. Chem. Solids 19 (1961) 308.
[50] P. Roschmann and H. Dotsch, Phys. Stat. Sol. (b) 82 (1977) 11.
[51] A.I. Akhiezer, V.G. Bar'yakhar, and S.V. Peletminskii, Spin Waves (Amsterdam, North-Holland, 1969).
[52] V.G. Bar'yakhtar and M.I. Kaganov, in: Ferromagnetic Resonance, ed. S.V. Vonsovskii (Oxford, Pergamon, 1966) p. 231.
[53] R.E. DeWames and T. Wolfram, J. Appl. Phys. 41 (1970) 987.
[54] T. Wolfram and R.E. DeWames, Phys. Rev. B4 (1971) 3125.
[55] T. Wolfram and R.E. DeWames, Phys. Rev. Lett. 24 (1970) 1489.
[56] T. Wolfram and R.E. DeWames, Phys. Lett. 30A (1969) 2.
[57] T. Wolfram and R.E. DeWames, Phys. Rev. B1 (1970) 4358.
[58] T. Wolfram and R.E. DeWames, Solid State Commun. 8 (1970) 191.
[59] T. Wolfram and R.E. DeWames, Solid State Commun. 9 (1971) 171.
[60] R.E. DeWames and T. Wolfram, Appl. Phys. Lett. 15 (1969) 297.
[61] Z. Frait, Phys. Stat. Sol. 2 (1962) 1417.
[62] R. Weber, IEEE Trans. Magnetics 4 (1968) 28.
[63] H. Puszkarski, Acta Physica Polonica A38 (1970) 899.
[64] P. Grünberg, J. Magn. Magn. Mat. 15–18 (1980) 766.
[65] P. Grünberg, C.M. Mayr, W. Vach, and M. Grimsditch, J. Magn. Magn. Mat. 28 (1982) 319.
[66] W. Wettling, R.S. Smith, W. Jantz, and P.M. Ganser, J. Magn. Magn. Mat. 28 (1982) 299.
[67] R.E. Camley and M. Grimsditch, Phys. Rev. B22 (1980) 5420.
[68] M. Grimsditch, A. Malozemoff, A. Brunsch, and G. Suran, J. Magn. Magn. Mat. 15–18 (1980) 769.
[69] R.E. Camley, T.S. Rahman, and D.L. Mills, Phys. Rev. B23 (1981) 1226.
[70] T.S. Rahman, D.L. Mills, and R.E. Camley, J. Appl. Phys. 52 (1981) 2286.
[71] R.E. DeWames and T. Wolfram, Solid State Commun. 7 (1969) 1451.
[72] R.E. Camley and D.L. Mills, J. Appl. Phys. 50 (1979) 7779.
[73] G.T. Rado and J.R. Weertman, J. Phys. Chem. Solids 11 (1959) 315.
[74] H. Puszkarski, Phys. Stat. Sol. (b) 50 (1972) 87.
[75] H. Puszkarski, IEEE Trans. Magnetics 9 (1973) 22.
[76] J.T. Yu, R.A. Turk, and P.E. Wigen, Phys. Rev. B11 (1975) 420.
[77] S.D. Brown, R.D. Henry, P.E. Wigen, and P.J. Besser, Solid State Commun. 11 (1972) 1179.
[78] R.D. Henry, P.J. Besser, D.M. Heinz, and J.E. Mee, IEEE Trans. Magnetics 9 (1973) 535.
[79] T.S. Rahman and D.L. Mills, Phys. Rev. B20 (1979) 1173.
[80] E. Trulinger and D.L. Mills, Solid State Commun. 12 (1973) 819.
[81] C. Demangeat and D.L. Mills, Solid State Commun. 20 (1976) 535.
[82] C. Demangeat and D.L. Mills, Phys. Rev. B16 (1977) 2321.
[83] P.K. Schwob, M. Tachiki, and G.E. Everett, Phys. Rev. B10 (1974) 165.
[84] C.H. Bajorek and C.H. Wilts, IBM Research Report RC 4559, Aug. 10, 1979.
[85] C.H. Bajorek and C.H. Wilts, J. Appl. Phys. 46 (1975) 1376.
[86] R.A. Pollak and C.H. Bajorek, J. Appl. Phys. 46 (1975) 1382.
[87] W.H. Meiklejohn and C.P. Bean, Phys. Rev. 102 (1956) 1413.
[88] W.H. Meiklejohn and C.P. Bean, Phys. Rev. 105 (1957) 904.
[89] C.E. Patton, Phys. Stat. Sol. (b) 92 (1979) 211.
[90] J. Smit and H.P.J. Wijn, Ferrites (New York, John Wiley, 1959).
[91] W.H. Von Aulock, Handbook of Microwave Ferrite Materials (New York, Academic Press, 1965).
[92] E. Schlömann, R.I. Joseph, and I. Bady, J. Appl. Phys 34 (1963) 672.
[93] M. Mita and H. Schimizu, J. Phys. Soc. Japan 35 (1973) 414.
[94] M. Mita and H. Shimizu, AIP Conf. Proc. 24 (1975) 514.
[95] R.K. Wangsness, Phys. Rev. 91 (1953) 1085.

[96] R.K. Wangsness, Phys. Rev. 93 (1954) 68.
[97] R.K. Wangsness, Phys. Rev. 97 (1955) 831.
[98] R.K. Wangsness, Amer. J. Phys. 24 (1956) 60.
[99] J. Kaplan and C. Kittel, J. Chem. Phys. 21 (1953) 760.
[100] J.S. van Wieringen, Phys. Rev. 90 (1953) 487.
[101] T.R. McGuire, Phys. Rev. 97 (1955) 831.
[102] S. Geschwind and L.R. Walker, J. Appl. Phys. 30 (1959) 163S.
[103] R.C. LeCraw, J.P. Remeika, and H. Matthews, Phys. Lett. 12 (1964) 9.
[104] G.B. Wright, ed., Light Scattering Spectra of Solids (New York, Springer-Verlag, 1969) pp. 185–263.
[105] M. Balkanski, ed., Proc. 2nd Int. Conf. Light Scattering in Solids (Paris, Flamarion, 1971) pp. 133–179.
[106] M. Balkanski, R.C.C. Leite, and S.P.S. Porto, eds., Proc. 3rd Int. Conf. Light Scattering in Solids (New York, John Wiley, 1976).
[107] I.E. Dzialoshinski, Sov. Phys. JETP 6 (1958) 1120.
[108] T. Moriya, Phys. Rev. 120 (1960) 91.
[109] I. Bernal, C.W. Struck, and J.C. White, Acta Cryst. 16 (1963) 849.
[110] J.C. Joubert, T. Shirk, W.B. White, and R. Roy, Mat. Res. Bull. 3 (1968) 671.
[111] A.J. Kurtzig, R. Wolfe, R.C. LeCraw, and J.W. Nielsen, Appl. Phys. Lett. 14 (1969) 350.
[112] R.C. LeCraw, R. Wolfe, and J.W. Nielsen, Appl. Phys. Lett. 14 (1969) 352.
[113] R.C. LeCraw, H.J. Guggenheim, and J.W. Nielsen, Phys. Lett. 31A (1970) 179.
[114] R. Wolfe, A.J. Kurtzig, and R.C. LeCraw, J. Appl. Phys. 41 (1970) 1218.
[115] A.J. Kurtzig, J. Appl. Phys. 42 (1971) 3494.
[116] M.H. Seavey, Solid State Commun. 10 (1972) 219.
[117] J. Schober, IEEE Trans. Magnetics 12 (1976) 401.
[118] V.I. Ozhogin, Sov. Phys. JETP 21 (1966) 874.
[119] A.S. Borovik-Romanov, V.G. Zhotikov, N.M. Kreines, and A.A. Pankov, JETP Lett. 23 (1976) 649.
[120] R.L. White, J. Appl. Phys. 40 (1969) 1061.
[121] R.C. Sherwood, J.P. Remeika, and J.H. Williams, J. Appl. Phys. 30 (1959) 217.
[122] R.M. White, R.J. Nemanich, and C. Tsang, Bull. Amer. Phys. Soc. 24 (1979) 471.
[123] R.M. White, R.J. Nemanich, and C. Tsang, J. Magn. Magn. Mat. 15–18 (1980) 773.
[124] R.M. White, R.J. Nemanich, and C. Herring, Phys. Rev. B25 (1982) 1822.
[125] G.F. Hermann, J. Phys. Chem. Solids 24 (1963) 597.
[126] I.S. Jacobs, H.F. Burne, and L.M. Levinson, J. Appl. Phys. 42 (1971) 1631.
[127] G.O. White and C.E. Patton, IEEE Trans. Magnetics 16 (1980) 684.
[128] G.F. Hermann, Phys. Rev. 133 (1964) A1334.
[129] F.B. Hagedorn and E.M. Gyorgy, Phys. Rev. 174 (1968) 540.
[130] J.R. Shane, Phys. Rev. Lett. 20 (1968) 728.
[131] F.B. Hagedorn, E.M. Gyorgy, R.C. LeCraw, J.C. Hensel, and J.P. Remeika, Phys. Rev. Lett. 21 (1968) 364.
[132] R.C. LeCraw, R. Wolfe, E.M. Gyorgy, F.B. Hagedorn, J.C. Hensel, and J.P. Remeika, J. Appl. Phys. 39 (1968) 1019.
[133] G. Cinader, Phys. Rev. 155 (1967) 453.
[134] V.I. Ozhogin, V.G. Shapiro, K.G. Gurtovoi, E.A. Galstyan, and A.Y. Chervonenkis, Sov. Phys. JETP 35 (1972) 1162.
[135] N. Koshizuka, K. Hayashi, and T. Tsushima, Ferrities, Proc. of the ICF3 (Japan, Center for Academic Publications, 1981) pp. 760–776.
[136] R.W. Damon, Rev. Mod. Phys. 25 (1953) 239.
[137] N. Bloembergen and S. Wang, Phys. Rev. 93 (1954) 72.
[138] H.J. Suhl, J. Phys. Chem. Solids 1 (1957) 209.
[139] F.R. Morgenthaler, J. Appl. Phys. 31 (1960) 95S.
[140] E. Schlömann, J.J. Green, and U. Milano, J. Appl. Phys. 31 (1960) 386S.
[141] C.E. Patton, Magnetic Oxides Part 2, ed. D.J. Craik (London, John Wiley, 1975) p. 875.
[142] C.E. Patton, Phys. Stat. Sol. (b) 93 (1979) 63.
[143] W. Jantz and J. Schneider, Solid State Commun. 9 (1971) 69.
[144] W. Jantz and J. Schneider, Phys. Stat. Sol. (a) 31 (1975) 595.
[145] Y.M. Yakovlev, Y.N. Burdin, Y.R. Shilnikov, and T.N. Bushveva, Sov. Phys. Solid State 12 (1971) 2475.
[146] W. Jantz, J. Schneider, and B. Andlauer, Solid State Commun. 10 (1972) 937.
[147] C.E. Patton and W. Jantz, J. Appl. Phys. 50 (1979) 7082.
[148] H.L. Hu and F.R. Morgenthaler, Appl. Phys. Lett. 18 (1971) 307.
[149] V.N. Venitskii, V.V. Eremenko, and E.V. Matyushkin, Sov. Phys. JETP 45 (1977) 796.
[150] V.N. Venitskii, V.V. Eremenko, and E.V. Matyushkin, JETP Lett. 27 (1978) 222.
[151] V.N. Venitskii, V.V. Eremenko, and E.V. Matyushkin, Sov. Phys. JETP 50 (1979) 5, 934.
[152] J.H.E. Griffiths, Nature 158 (1946) 670.
[153] C. Kittel, Phys. Rev. 73 (1948) 155.
[154] S.M. Bhagat, in: Techniques of Metals Research, Vol. 6, Measurements of Physical Properties, Part 2, Magnetic Properties and Mössbauer Effect, ed. E. Passaglia (Sussex, Wiley Interscience, 1973).

[155] J.C. Sethares, M.H. Seavey, T.G. Purnhage, and M.R. Stiglitz, J. Appl. Phys. 35 (1964) 898.
[156] C.E. Patton and W. Jantz, IEEE Trans. Magnetics 14 (1978) 698.
[157] W. Haubenreisser and D. Linzen, Phys. Stat. Sol. 2 (1962) 734.
[158] Y.H. Liu and C.E. Patton, J. Appl. Phys. 53 (1982) 5116.
[159] H.Z. Cummins, Proc. 2nd Int. Conf. Light Scattering in Solids (Paris, Flamarion, 1971).
[160] D. Bechtle, Rev. Sci. Instrum. 47 (1976) 493.
[161] D. Bechtle, Rev. Sci. Instrum. 47 (1976) 1377.
[162] Burleigh Instruments, Inc., Technical Memo for Fabry–Perot Interferometry No. FP-140-475 (1976).
[163] Burleigh Instruments, Inc., Tech Memo/Manual for Das-1 Data Acquisition/Stabilization System, No. Das-184–11773 (1976).
[164] R. Vacher, H. Sussner, and M.V. Schickfus, Rev. Sci. Instrum. 51 (1980) 288.
[165] J.G. Dil, N.C.J.A. van Hijningen, F. van Dorst, and R.M. Aarts, Appl. Optics 20 (1981) 1374.
[166] S.M. Lindsay, M.W. Anderson, and J.R. Sandercock, Rev. Sci. Instrum. 52 (1981) 1478.